Performance Evaluation of Planar Solid Oxide Fuel Cell with Different Interconnector Configurations

Submitted in partial fulfillment of the requirements

For the award of the degree of

DOCTOR OF PHILOSOPHY

in

MECHANICAL ENGINEERING

by

Raj Kumar

(Roll No. 718025)

Under the supervision of

Dr. A. Veeresh Babu

(Professor, MED)

DEPARTMENT OF MECHANICAL ENGINEERING

NATIONAL INSTITUTE OF TECHNOLOGY WARANGAL

WARANGAL– 506 004, TELANGANA, INDIA.

FEBRUARY 2023

THESIS APPROVAL FOR Ph.D.

This thesis entitled **"Performance evaluation of planar solid oxide fuel cell with different interconnector configurations"** by **Mr. Raj Kumar** is approved for the degree of Doctor of Philosophy.

_____

_____

_____

Examiner

Dr. A. Veeresh Babu

Professor, Department of Mechanical Engineering, NIT Warangal

Supervisor

Prof. V. Suresh Babu

Head, Department of Mechanical Engineering, NIT Warangal

Chairman

NATIONAL INSTITUTE OF TECHNOLOGY

WARANGAL – 506 004, Telangana State, INDIA

CERTIFICATE

This is to certify that the thesis entitled **"Performance evaluation of planar solid oxide fuel cell with different interconnector configurations"** being submitted by **Mr. Raj Kumar** for the award of the degree of Doctor of Philosophy in Mechanical Engineering to the National Institute of Technology, Warangal, India is a record of the bonafide research work carried out by him under my supervision. The thesis has fulfilled the requirements according to the regulations of this Institute and in my opinion has reached the standards for submission. The results embodied in the thesis have not been submitted to any other University or Institute for the award of any degree.

Place: Warangal,

Date:

Dr. A. Veeresh Babu
Supervisor
Professor,
Department of Mechanical Engineering
National Institute of Technology, Warangal.

NATIONAL INSTITUTE OF TECHNOLOGY

WARANGAL – 506 004, Telangana State, INDIA

DECLARATION

This is to certify that the work presented in the thesis entitled **"Performance evaluation of planar solid oxide fuel cell with different interconnector configurations"** is a bonafide work done by me under the supervision of **Dr. A. Veeresh Babu**, Professor, Department of Mechanical Engineering and was not submitted elsewhere for award of any degree.

I declare that this written submission represents my ideas in my own words and where others ideas or words have not been included I have adequately cited and referenced the sources. I also declare that I have adhered to all principles of academic honesty and integrity and have not misrepresented or fabricated or falsified any idea/data/fact/source in my submission. I understand that any violation of the above will be a cause for disciplinary action by the Institute and can also evoke a penal response from the sources which have thus not been appropriately cited or from whom proper permission has not been taken when needed.

Place: Warangal **Raj Kumar**

Date: **Roll no. 718025**

ACKNOWLEDGEMENT

I would like to express my sincere gratitude and profound indebtedness to my supervisor **Dr. A. Veeresh Babu,** Professor, Mechanical Engineering Department, NITW because he cultivated a research attitude in my mind for applying learning approach in my research as well as in the individual life. His important thoughts have given me an immense support to complete my research work. His positive and daring attitude in different aspects trained me to handle the situations with enthusiasm. His suggestions helped a lot to make myself stronger in all differing circumstances. His brilliant support made me to sustain and develop knowledge and be close to my home life. I owe a lot to him for making me a part of the continuity of the profession.

I extend my sincere gratitude to university authorities, **Prof. N.V. Ramana Rao,** Director, National Institute of Technology, Warangal and other top officials who gave me an opportunity to carry out research work and for providing the necessary facilities and encouragement throughout my work.

I sincerely thank **Prof. V. Suresh Babu,** Head, Mechanical Engineering Department, National Institute of Technology, Warangal for his continuous support towards carrying out research work.

I wish to express my sincere and wholehearted thanks and gratitude to my doctoral scrutiny committee (DSC) members **Dr. K. Madhu Murthy,** Professor, Department of Mechanical Engineering, **Dr. V. Rajesh Khana Raju,** Professor, Department of Mechanical Engineering, **Dr. Shirish H. Sonawane,** Professor, Chemical Engineering Department, National Institute of Technology, Warangal for their kind help, continuous monitoring, encouragement and valuable suggestions for successful completion of research work.

I express my heartfelt thanks and gratitude to my fellow research scholars **Amarnath G.B, Bhukya Balaji** ,**Ajmera Suresh**, **Abhishek Kumar,** M.Tech Scholars **– V. Mahesh , A. Akshay** and all the Mechanical engineering faculty members who has directly or indirectly helped me through their thought provoking ideas, concepts and for their valuable support in the beautiful journey of my Ph.D.

I am also thankful to all the supporting and technical staff of the Department of Mechanical Engineering who has helped me during my work. A special mention to **Mr. M. V. Vijay Kumar,** office staff for his constant help and encouragement.

Last but not the least, a special debt of deep gratitude to my parents, wife and my daughter, who are undoubtedly the happiest to see me complete this endeavor. To them, I owe all my accomplishments.

Finally, I would like to acknowledge the help given by all the persons who have directly or indirectly supported the work.

Raj Kumar

Abstract

A Solid Oxide Fuel Cell (SOFC) is an intricate system involving an amalgam of several electrochemical reactions with thermal-fluid-electrical interactions. To enhance the performance of the fuel cell, the interconnector configuration has to be designed judiciously. In this article, a trapezoidal interconnector design for anode and cathode flow channels after a thorough simulation carried out with all the multi-physics involved using ANSYS fluent is proposed. The proposed trapezoidal interconnector design performance is compared against the conventional rectangular interconnector configuration. From the results, it is observed that the trapezoidal interconnector design provides an increase of 18.2% power density compared to the conventional rectangular interconnector configuration when the cell is operated at 1123K operating temperature. The proposed design offers the advantage of operating the cell at a lower operating temperature of 1073K with an increment of 10.68% power density compared to the 1123K operating temperature in a conventional rectangular interconnector configuration. In addition, the influence of rib width on the anode side fuel transport is also evaluated by designing a SOFC with a rectangular parallel anode interconnector and a trapezoidal channel cathode interconnector. It is concluded that the rib width of the anode side has a moderate effect on fuel transport in anode-supported SOFCs.

Additionally in this article, a novel rhombohedral interconnector with a staggered position is also proposed by considering the influence of flow field variations on heat and mass transfer. The rhombohedral staggered interconnectors help to alter the fluid flow patterns in the flow channels, leading to an improvement in heat and mass transport behavior. It also assists to control the pressure distribution in the flow channels and improves the performance of anode-supported SOFCs. First, a comparison between existing experimental research and a traditional rectangular interconnector model is carried out to validate the physics of the SOFC functioning. Then the performance of a staggered-position rhombohedral interconnector is evaluated to that of a typical rectangular interconnector. To further understand the impact of flow rate on cell performance, parametric research with varied mass flow rates is conducted. The findings indicate that when compared to a conventional rectangular interconnector, the rhombohedral staggered interconnector design enhances the power density by 33.9 %. With an increase in mass flow rate beyond a specified stoichiometric range, the performance decreases indicating an excessive

supply of reactants. Using the proposed staggered rhombohedral interconnector configuration, the SOFC can be designed to operate optimally.

Keywords: ANSYS, Flow channels, Interconnector, Rib width, SOFC, CFD, Flow-field, Fuel cell, Interconnector, Simulation.

TABLE OF CONTENTS

LIST OF FIGURES

LIST OF TABLES

NOMENCLATURE

D_{ij}	Effective (ordinary) diffusivity (m^2/ s)
D_{ij}^{eff}	Average effective diffusivity (m^2/ s)
E	Specific total energy (J / kg)
F	Faraday's constant (C / mol)
I	Current density (A / m^2)
I_o	Exchange current density (A / m^2)
J_i	Diffusive flux (kg/m^2s)
k	Thermal conductivity (W / mK)
P	Pressure (Pa)
R	Gas constant (8.3145 J /mol K)
T	Temperature (K)
$\vec{v}$	Velocity vector (m /s)
X	Mole fraction
Y	Mass fraction

Greek Symbols

α	Charge transfer coefficient
ε	Porosity
η	Potential loss (V)
μ	Dynamic viscosity (kg. s /m)
ρ	Density (kg/ m^3)
σ	Ion/electron conductivity (Ω^{-1} m^{-1})
ϕ	Electric potential (V)
$\vec{\tau}$	Viscous stress tensor
ξ	Stoichiometric ratio

Chemical notations

Ni	Nickel
NiO	Nickel oxide
YSZ	Yttria-stabilized zirconia
LSM	Lanthanum strontium manganite

Abbreviations

2D	Two Dimensional
3D	Three Dimensional
BCGSTAB	Biconjugate gradient stabilized algorithm
CAD	Computer aided design
CRI	Conventional rectangular interconnector

RATC	Rectangular parallel Anode interconnector and Trapezoidal Cathode interconnector
SOFC	Solid oxide fuel cell
SRhI	Staggered Rhombohedral Interconnector
TI	Trapezoidal interconnector
TPB	Triple Phase Boundary

CHAPTER 1

Introduction

1.1 Background

The sustainable development of any nation is greatly reliant on energy. The term sustainable development has numerous definitions, but the most popular one states that it is "the development that meets the requirements of the present without compromising the ability of future generations to meet their own needs"[1]. The population and economic growth have a direct impact on global energy usage. According to the most recent predictions, from 2020 to 2050, the total global energy consumption is expected to grow at an average annual rate of 1.3% as depicted in Figure 1. Over the next 28 years, the global energy consumption will rise from 601.5 quadrillion Btu to 886.3 quadrillion Btu[2].

Fossil fuels such as coal, natural gas, and oil have been burnt in conventional power production systems based on the "heat engine" principle for few decades [3]–[7]. Continuous attempts have been made to increase energy conversion efficiency while lowering emissions of pollutants such SO_x, NO_x, and CO_2 that have a negative impact on the environment[8]–[10]. Gas turbine power plants' thermal efficiency ranges from 30 to 35% whereas gas-powered engines' ranges from 30 to 44% , turbo-charged diesel engines' ranges from 45 to 54%, and combined cycle power plants' ranges from 60 to 60% [11].

A greenhouse gas called CO_2 is the primary cause of climate change and other related environmental problems. According to predictions, the earth's surface temperature has risen by around 0.6 ^oC in the last century. According to estimates, the earth's surface temperature might rise by 2 to 6 ^oC in the following century if fossil fuel usage continues to rise as it has been.

More reliable, efficient, and clean energy sources are desperately required to fulfill the rising energy demands, diminishing global fossil fuel supplies, and requirements to reduce air pollution. Fuel cells are extensively considered as the next generation power sources for both stationary and mobile usages as they can generate heat as well as power, have a high efficiency of converting fuel to electricity, and have minimal environmental effects.

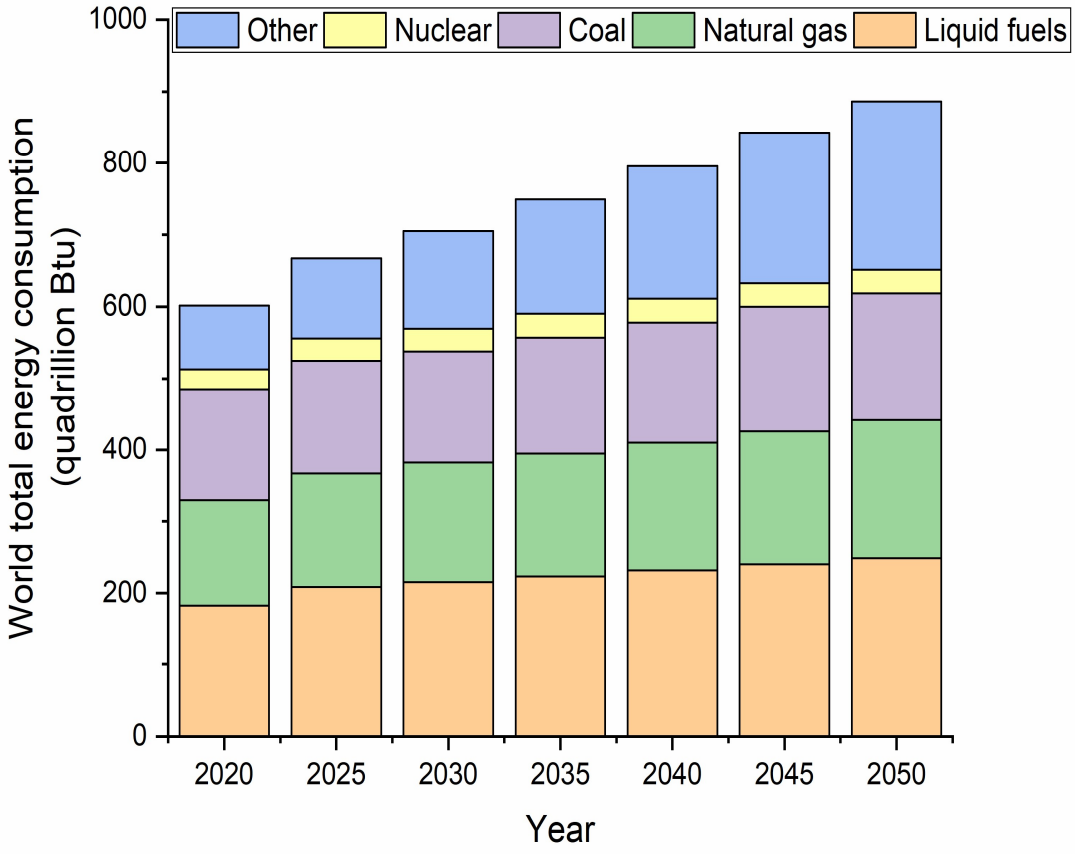

FIGURE 1. 1: World total energy consumption [2]

1.2 Introduction to Fuel Cell

It is a well-known fact that non-renewable energy sources are limited and get depleted over their usage. So, for continuous power generation, an alternative energy source that is renewable needs to be explored. A fuel cell is an ideal alternative energy source that can meet the exponentially rising energy demand and could help to reduce global warming by improving the efficiency of electrical power generation. Fuel cells are galvanic cells that directly transform the chemical energy of the fuel into electrical energy through an electrochemical process in which fuel is oxidized at the anode. Fuel cell technology is advancing in comparison to combustion engines, because of its great efficiency and its capacity to deal with natural resource depletion to a greater extent[12], [13]. Low to zero emissions, the use of a range of fuels, low maintenance

requirements, quiet operation, high levels of reliability, and long system lifespan are the key characteristics of fuel cells[14], [15].

1.3 History of Fuel Cell

William Robert Grove created the first fuel cell in 1839 [16]. During an experiment, the fuel cell's operating principle was unintentionally found. Groove joined the two electrodes and noticed that the current was flowing against the direction it should have been, consuming the hydrogen and oxygen. Nitric acid was used to submerge a platinum electrode and zinc sulphate to submerge a zinc electrode. He coined the system as "gas battery." In 1842, Groove created a gas chain by connecting 4 gas batteries in series; at 1.8 V, 12 A of current was produced. Grove's fuel cell could not be used in practice due to electrode corrosion and material instability[17]–[23].

Friedrich Wilhelm Ostwald, who is credited with developing the field of chemistry-physics, conducted an experimental study of the link between the various fuel cell components in 1893. These included electrodes, electrolyte, oxidising and reducing agents, anions, and cations. His discovery served as the foundation for further advancement in the field of fuel cell chemistry. Walther Nernst was the first to use zirconium as a solid electrolyte in 1900, while William W. Jacques created the first fuel cell with practical uses (Direct Carbon Fuel Cell) in 1896 [24].

Chemical engineer Francis Bacon at Cambridge University in England began studying the fuel cell in 1930. The first alkaline fuel cell was created by Bacon in 1958 [19], [25]. The National Aeronautics and Space Administration (NASA) of the United States employed fuel cells to supply electrical energy during prolonged space missions in the 1950s and 1960s. The alkaline NASA fuel cell uses oxygen as the oxidant and hydrogen as the fuel. The fuel cell performs three essential tasks during space travel: (i) electricity to operate the spaceship, (ii) water to cool the equipment and for drinking, and (iii) heat to prevent the astronauts from freezing [24], [26].

NASA and the University of Southern California collaborated to develop a direct methanol fuel cell in 1990. In some applications, direct methanol fuel cells take the place of conventional batteries. Because they have a longer lifespan than lithium ion batteries and can be recharged by just switching out the fuel cartridge, they are anticipated to grow in popularity. Sanyo (Japan),

Toshiba, Hitachi, NEC, and Samsung (Korea) are among the companies developing these fuel cells [27]–[29].

There are numerous enterprises producing fuel cells now for various uses. In buses, vehicles, trucks, motorbikes, ships, aeroplanes, forklifts, and trains, fuel cells are most frequently used [30]–[35]. Mobile phones, laptops, and other portable electronic equipment are also powered by fuel cells. In large-scale applications including shopping centers, warehouses, hospitals, schools, and banks, fuel cell electricity is used [36]–[38]. Fuel cell technology is also used to power vacuum cleaners, vending machines, and traffic signals. Methane gas produced during waste disposal and water treatment is used in fuel cells to generate power [39]. As we can see, fuel cells have a wide range of applications in various fields.

1.4 Working principle of Fuel Cell

A fuel cell is made up of three basic parts: an electrolyte that separates the two electrodes known as the anode and cathode as shown in Figure 2. Electrodes have strong electronic conductivity and are porous. The electrochemical reaction involves an electrolyte, which only permits ions to flow through. An electrolyte, in other words, has strong ionic conductivity[40].

The oxidation half reaction and the reduction half reaction are the two subsets of the electrochemical process in a hydrogen-based fuel cell. For instance, when a fuel cell with a proton conducting electrolyte is utilized, the reaction at the anode is half an oxidation reaction where hydrogen breaks down into positively charged protons and negatively charged electrons. While the electrons go through an external circuit to produce energy, the protons pass through the electrolyte membrane. The electrons migrate toward the cathode after completing the circuit[41], [42]. The anodic reaction is as follows:

$$H_2 \rightarrow 2H^+ + 2e^- \qquad (1.1)$$

At the cathode, oxygen enters and interacts with positively charged protons and electrons that have passed through electrolytes. Depending on the fuel cell's design, oxygen may occasionally take up electrons and travel through the electrolyte to the anode, where it interacts with protons.

Water is produced as a result of the oxygen reaction, which is a reduction half reaction[43], [44].

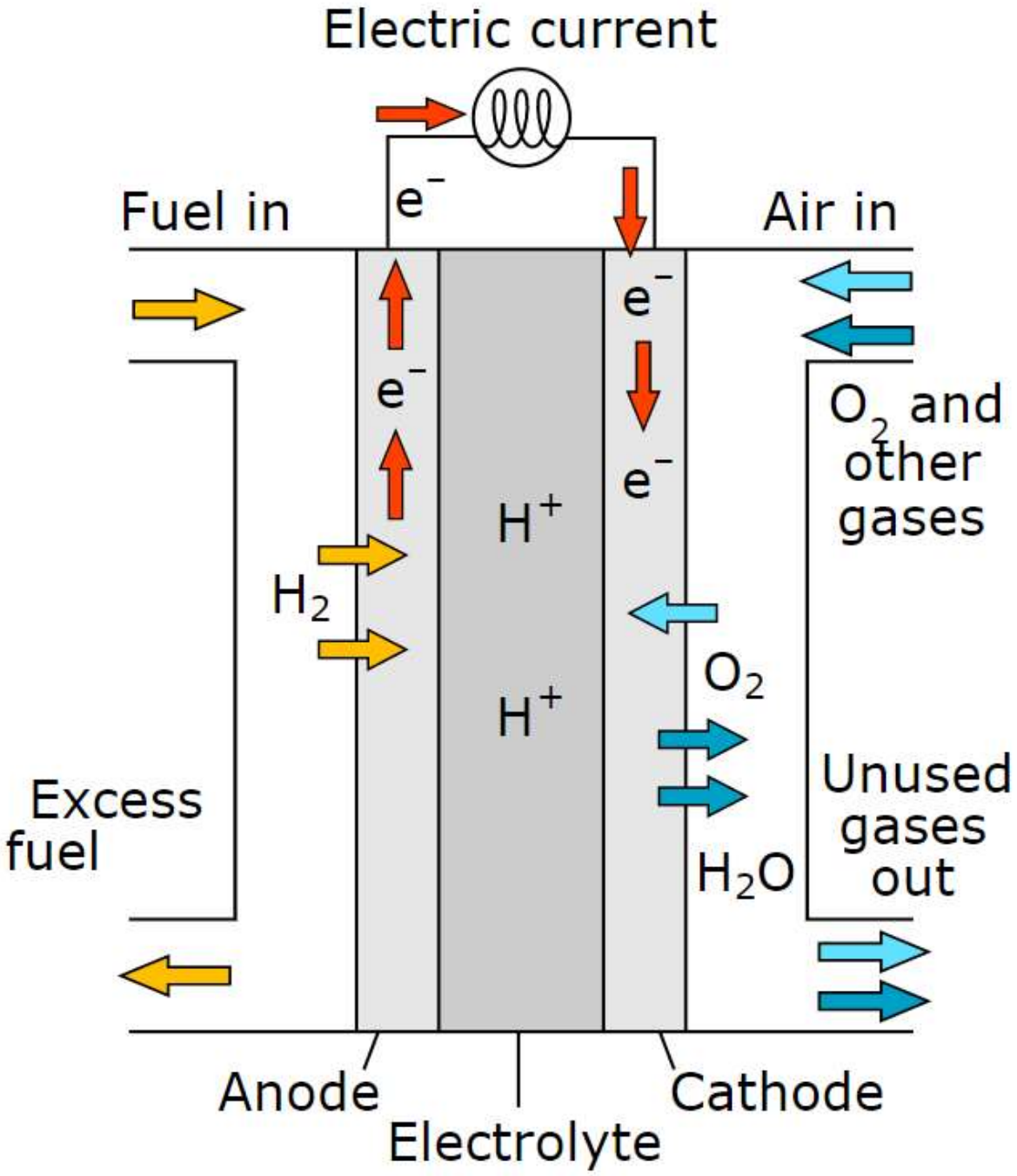

FIGURE 1. 2: Fuel cell working principle [45]

The cathodic reaction is as follows

$$\frac{1}{2}O_2 + 2H^+ 2e^- \rightarrow H_2O \qquad (1.2)$$

The full cell overall reaction is as follows:

$$H_2 + \frac{1}{2}O_2 \rightarrow H_2O \qquad (1.3)$$

A single fuel cell produces a low voltage of just about 0.7 volts. The fuel cells are connected in series to provide the necessary voltage output. Fuel cell stack refers to this arrangement of fuel cells [46]–[50].

1.5 Types of Fuel Cells

All fuel cell models operate on the same principles. They differ from one another in terms of reactant type, operating temperature, and electrolyte membrane composition. The following are the six main types of fuel cells[51]–[59]. The Attributes of different types of fuel cells are tabulated in table 1.

1. Alkaline Fuel Cell (AFC)

2. Polymer Electrolyte Membrane Fuel Cell (PEMFC)

3. Phosphoric Acid Fuel Cell (PAFC)

4. Direct Methanol Fuel Cell (DMFC)

5. Molten Carbonate Fuel Cell (MCFC)

6. Solid Oxide Fuel Cell (SOFC

TABLE 1. 1: Attributes of different types of fuel cells [37], [38][55], [60]–[65].

FUEL CELL TYPE	COMMON ELECTROLYTE	OPERATING TEMPERATE	TYPICAL STACK SIZE	ELECTRICAL EFFICIENCY (LHV)	APPLICATIONS	ADVANTAGES	CHALLENGES
AFC	Aqueous potassium hydroxide soaked in a porous matrix, or alkaline polymer membrane	<100°C	1–100 kW	60%	Military Space Backup power Transportation	Wider range of stable materials allows lower cost components Low temperature Quick start-up	Sensitive to CO_2 in fuel and air Electrolyte management (aqueous) Electrolyte conductivity (polymer)
PEMFC	Perfluorosulfonic acid	<120°C	<1 kW–100 kW	60% direct H2; 40% reformed fuel	Backup power Portable power Distributed generation	Solid electrolyte reduces corrosion and electrolyte management	Expensive catalysts Sensitive to fuel impurities

					Transportation Specialty vehicle	problems Low temperature Quick start-up	
PAFC	Phosphoric acid soaked in a porous matrix or imbibed in a polymer membrane	150°–200°C	5–400 kW, 100 kW module (liquid PAFC) <10 kW (polymer membrane)	40%	Distributed generation	Suitable for Combined Heat and Power(CHP) Increased tolerance to fuel impurities	Expensive catalysts Long start-up time Sulfur sensitivity
DMFC	Solid Polymer membrane	50°–200°C	Upto 1.5 kW	40%	Replace batteries in mobile phones, laptops and other portable applications	Reduced cost due to absence of fuel reformer	Low efficiency and power density, methanol cross-over and poisonous by-product

MCFC	Molten lithium, sodium, and/or potassium carbonates, soaked in a porous matrix	600°–700°C	300 kW–3 MW, 300 kW module	50%	Electric utility Distributed generation	High efficiency Fuel flexibility Suitable for CHP Hybrid/gas turbine cycle	High temperature corrosion and breakdown of cell components Long start-up time Low power density
SOFC	Yttria stabilized zirconia	500°–1,000°C	1 kW–2 MW	60%	Auxiliary power Electric utility Distributed generation	High efficiency Fuel flexibility Solid electrolyte Suitable for CHP Hybrid/gas turbine cycle	High temperature corrosion and breakdown of cell components Long start-up time Limited number of shutdown

1.6 Solid Oxide Fuel Cell (SOFC)

Fuel cells are generally named after the fuel/electrolyte used. The fuel cell which uses solid composite or ceramic as electrolyte for oxidation is called a solid-oxide fuel cell (SOFC). As the operating temperature of SOFC is about 1000^{o}C, it is categorized as a high operating temperature fuel cell. This feature of SOFC offers the advantage of reduced ionic and electronic resistances in the electrolyte and electrode respectively, eliminating the requirement of precious-metal catalysts as used in other fuel cells[2–5]. In addition, the byproduct of SOFC contains an enormous amount of heat energy which can be re-circulated and when some hydrocarbons are utilized as fuel, it is used for internal reforming[70].

1.6.1 SOFC Development Background

Since 1899, Walther Nernest has been working on the SOFC project. 85% ZrO2 and 15% Y2O3 make up the solid Nernst mass, which was created by Nernst. A first SOFC prototype was created in 1937 by Emil Baur and H. Preis, and it was used at 1000 °C [71]–[73]. It was discovered that the most efficient electrolyte could be created with 60% Nernst mass, 10% clay, and 30% lithium zirconate. However, the price of the necessary materials proved prohibitive[74]–[76]. Following the work of Carl Wagner, who linked the electrical conductivity in mixed oxides like dopes ZrO2 to the presence of oxygen vacancies, more in-depth investigations on SOFC started in 1943. In the late 1950s, development on SOFC innovation began to accelerate[77]–[81].

A fuel cell device was created in 1962 by Westinghouse researchers Weissbart and Ruka utilising porous platinum as the electrode material and an electrolyte composed of 85% ZrO2 and 15% CaO, a variation on the Nernst mass material. In 1998, Westinghouse and Siemens merged to form Siemens-Westinghouse, which went on to play a vital role in the development of the Tubular SOFC technology[76], [78]. Since the middle of the 1990s, a wide variety of SOFC materials and designs have been developed. Due to performance and cost considerations, anode-supported planar SOFCs gained popularity among diverse designs. The demand for distributed generation SOFC surged about 2000, but the technology was not yet ready for the market. Since 2000, SOFC has kept up its research and development activities in the academic and industrial

communities. While industrial developers mostly concentrate on producing prototypes, academic researchers primarily concentrate on the underlying theory, such as modelling, simulation, and analysis of catalysis and electrolyte property[79]–[81].

1.6.2 SOFC Working Principle

A solid electrolyte placed between two porous electrodes known as the anode and cathode makes up a solid oxide fuel cell. The SOFC operates at high temperatures, between 500°C and 1000 °C, and it is at these temperatures that oxygen ions or protons conduct ionically. The SOFC electrolyte material should be extremely chemically and mechanically stable, have good ionic conductivity, and be sufficiently dense to prevent gas mixing. The SOFC working principle is depicted in Figure 3.

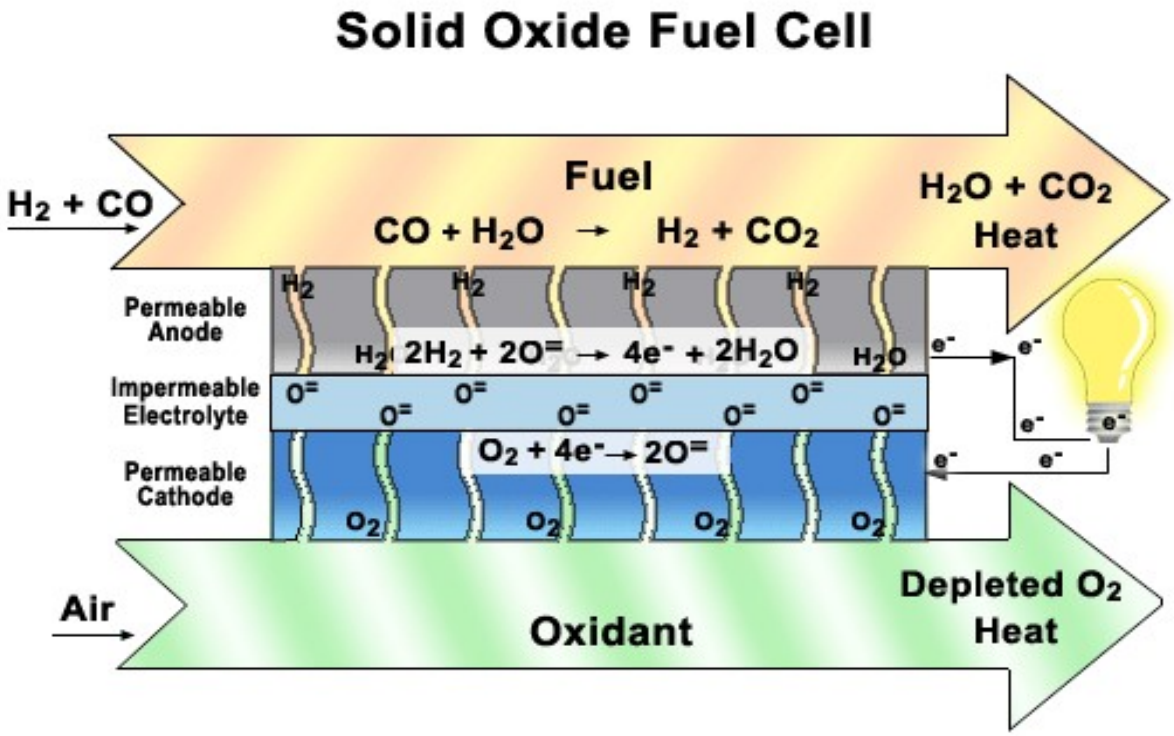

FIGURE 1. 3: SOFC Working Principle [82]

The fuel is electrochemically oxidised at the anode, while the fuel is electrochemically reduced at the cathode. Due to its high electrochemical activity, hydrogen is typically employed as a fuel, although carbon monoxide can also be used in conjunction with hydrogen. The internal

reformation of the fuel is possible due to the high operating temperature, and hydrocarbons like methane can also be used as fuel. An oxidant corresponds to air or oxygen. An SOFC generates water at the anode by using oxygen ions as a charge carrier. The chemical potential gradient of ions across the electrolyte acts as the driving force between the fuel and oxidant[83]–[88].

1.6.3 Materials for SOFC Components

1.6.3.1 Electrolyte material

Yttria-Stabilized Zirconia (YSZ) is the most widely utilised electrolyte material for SOFC systems. According to the ionic conductivity restrictions for YSZ, which apply to operating temperatures below 750 °C it is not appropriate for electrolyte-supported SOFCs[89]–[91]. Scandia stabilised zirconia Sc2O3-ZrO2 (SSZ), Gd or Sm-doped CeO2 (CGO or SDC), and Sr and Mg-substituted LaGaO3 are some of the additional materials frequently used as electrolytes (LSGM). The lowest working temperature of these systems is influenced by the ionic conductivity as well as a reasonable estimation of the thinnest film thickness that may be manufactured[92]–[96]. In comparison to YSZ, SSZ exhibits better stability in oxidising and reducing environments and a higher conductivity. Price, availability, and degradation are issues with SSZ deployment. In addition to having a higher conductivity than YSZ, LSGM is also appropriate for usage at temperatures between 600 and 700 °C[97], [98]. The power density of YSZ-based SOFCs is insufficient at these temperatures. The LSGM has a stability issue, necessitating more study of this material[99], [100].

1.6.3.2 Anode Material

Nickel/YSZ cermet is the most popular material used for anodes (ceramic metal composite). This blend of YSZ serves as an element for ion conduction, while Ni metal, which has strong electronic conductivity and catalytic activity, serves as the anode. The main problem with Ni is that it reacts with oxygen to generate NiO. (Nickel Oxide). More space is occupied by NiO than by Ni, creating stresses in the electrode that might cause it to shatter, changing its structure as well as that of the entire cell. Problems at the anode arise when hydrocarbons are utilised as fuel because of their sulphur content and carbon production. The choice of materials is constrained by

additional factors, such as thermal expansion coefficients, in addition to electrochemical characteristics. By creating novel materials like Ni-Al2O3 and Ni-TiO2, efforts have been made to solve the problem of thermal expansion mismatching between YSZ electrolyte and Ni/YSZ anode[101]–[103]. Lowering the operating temperature is one strategy for limiting the generation of carbon. Ni/YSZ anodes can have a Yttria-doped ceria (YDC) layer added to improve cell performance and resistance to carbon deposition. Cu/YSZ is one of the potential materials for anodes since it does not catalyse the creation of carbon and is more tolerant of sulphur concentrations than Ni/YSZ[104], [105]. Due to their stability in reducing environments, chromites and titanates are the perovskites that have received the most attention.

1.6.3.3 Cathode Material

Strontium-doped perovskite-based lanthanum manganite (La0.84Sr0.16) MnO3, or LSM, is the most often used and researched cathode material. Although LSM's ionic conductivity is rather low, it is an excellent catalyst for the dissociation of oxygen molecules at higher temperatures and its thermal expansion coefficient corresponds well with YSZ electrolyte[106]–[108]. Low ionic conductivity is the cause of the activation losses on the cathode side. Any substance that can effectively catalyse the creation of oxygen ions can help to reduce these losses. For instance, a composite cathode, LSM/YSZ, boosts overall catalytic activity even at lower temperatures by providing improved oxygen ion conductivity and a larger active surface[109]. The chemical compatibility of LSM with YSZ electrolyte is another issue. Depending on the quantity of strontium, it combines with YSZ electrolyte to produce La2Zr2O7 and SrZrO3, respectively. Insulating and highly resistant materials La2Zr2O7 and SrZrO3 refer to interface delamination and performance degradation in cells[110]. Alternative cathode materials have been employed to address this issue and it was reported that the addition of iron to the cobalt site results in the formation of (La1-xSrx)(Co1-yFeyO3) (LSCF), which enhances the fuel cell performance[111]–[113].

1.6.4 SOFC Configurations

Based on the geometrical construction, SOFCs are classified as planar and tubular. Figure 1.4 depicts a general perspective of the tubular SOFC. A tubular arrangement consists of two tubes: an alumina-made inner tube known as the air injection and guidance tube and an exterior tube known as the cell tube (Al2O3). Anode and cathode surfaces make up the cell tube's outer and inner surfaces, respectively, and solid electrolyte is located in the space between them. Preheated air enters the cell tube through the injection tube, travels across the space between the injection and cell tubes, and then flows over the cathode surface. The cell tube has a closed end on one side. Along the outside of the cell tube and in a direction parallel to the air flow, the fuel gas passes over the anode surface. The cathode and electrolyte are traversed by oxygen ions, which then interact with the fuel to produce current [96]. Due to the closed end of each cell support tube, this sort of cell does not require a gas tight barrier between cells [114]. However, because of longer current routes and significant voids within the stack structure, the tubular solution has drawbacks such as high production costs, low power density, and increased ohmic losses[74][115].

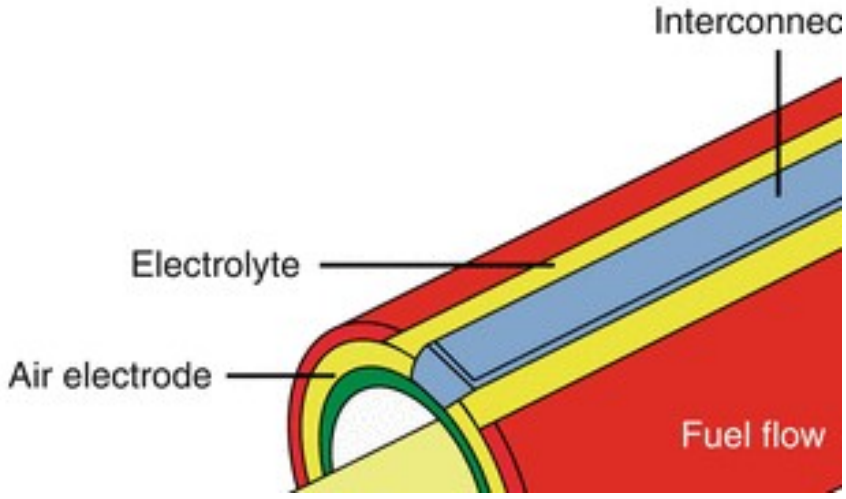

FIGURE 1. 4: Tubular SOFC [59]

In comparison to tubular SOFC, the planar cell has gained major attention as it offers trouble-free production[116]. In addition, when employed in combined heat and power (CHP) applications, planar SOFCs which operate at high temperatures (700^{o}C-900^{o}C) achieve about

90% overall efficiency[117]. The planar SOFC facilitates the usage of thin electrolytes thereby offering lower internal resistance and providing scope for the cell to operate at fairly high current densities (up to 1,000mA cm−2)[118]. A positive-electrolyte-negative electrode (PEN), which connects the top and bottom of the cell stack, as well as air and fuel channels, make up the planar structure, as shown in Figure 1.5. Between the anode and the separator plate, the fuel gas channel is situated, while on the opposite side, between the cathode and separator plate the air channel is located[59]. Compared to tubular SOFC, planar SOFC is more affordable, has simpler fabrication methods, a higher power density, and reduced ohmic losses. The planar SOFCs offer three variants, co-flow, counter flow, and cross flow, depending on the flow direction of the oxidant and fuel inside the cell. Planar SOFC has some disadvantages, including the requirement of high-temperature gas sealing between the cell components and brittleness under tension and thermal stresses at the interfaces between multiple cells that might result in mechanical degradation[119], [120].

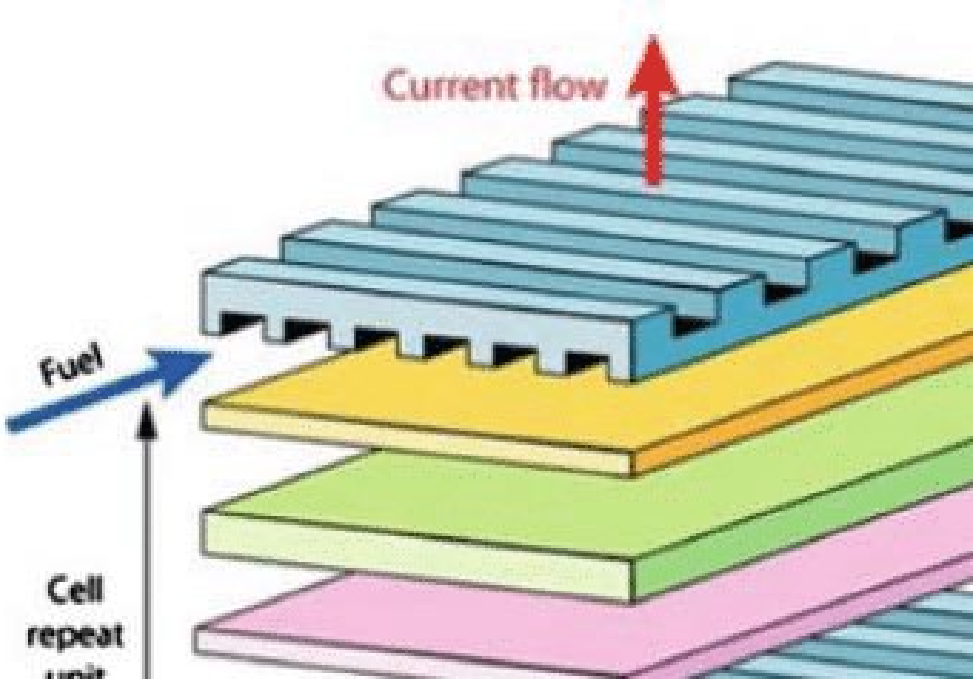

FIGURE 1. 5: Planar SOFC[59]

Based on the component of the cell which is providing mechanical strength and support, the planar SOFC is classified as electrolyte supported cell, anode supported cell and cathode

supported cell. In Figure 1.6, the configurations are shown[121]. Cells with a dense electrolyte membrane and thin anode and cathode electrodes are known as electrolyte-supported cells. Because of the dense electrolyte, ohmic losses increase, reducing power density. As a result, to attain equivalent performance, this cell type requires a greater working temperature. In anode-supported SOFC, the thick anode is topped with a thin electrolyte. The ohmic losses and operating temperature of anode-supported SOFCs are lower than those of electrolyte-supported SOFCs because the anode's electrical conductivity is high and thin electrolyte is used. Due to mass transport limitations, a thicker anode causes concentration losses to increase. Cathode-supported SOFCs can function at lower temperatures than anode-supported SOFCs because of the thin electrolyte that is utilized. Higher concentration polarization losses can be expected as a result of a thicker cathode that may restrict the delivery of reactants to the reaction sites. Ohmic losses created in cathode-supported structures are larger than those produced in anode-supported structures because the cathode has a lower electrical conductivity than the anode[122][123].

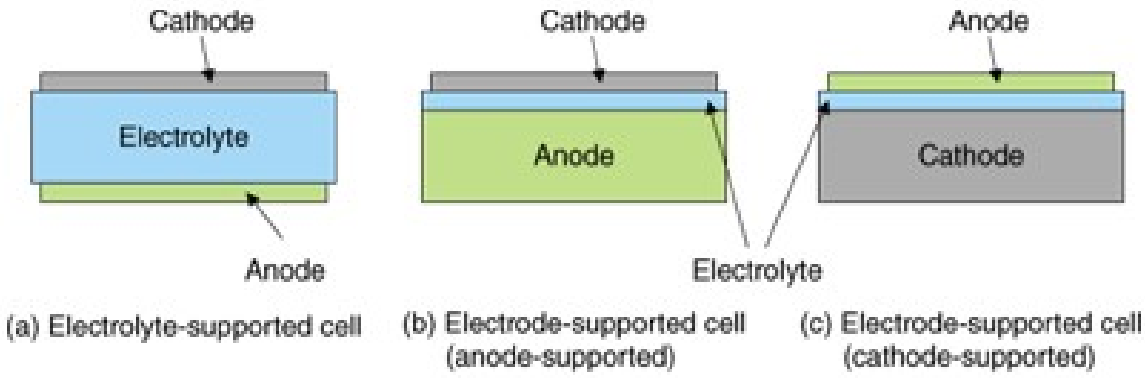

FIGURE 1. 6: SOFC classification based on component providing mechanical strength and support [121]

1.6.5 Fuel for SOFC

Fuel adaptability, which allows a wide variety of fuels to be used in SOFCs, is one of its main advantages. Unlike low temperature fuel cells, where CO can be poisonous, SOFCs can use CO as a fuel without it being harmful to the system. Among the other fuels that could be used are hydrogen, methane, long-chain hydrocarbons, ethanol, methanol, biogas, ammonia, hydrogen sulphide, etc[119], [120], [124]–[127].

The electrochemical reactions that occur when hydrogen is used as a fuel in SOFC are as follows:

At anode:

$$H_2 + O^{2-} \rightarrow H_2O + 2e^- \qquad (1.4)$$

At cathode:

$$\frac{1}{2}O_2 + 2e^- \rightarrow O^{2-} \qquad (1.5)$$

The overall cell reaction is:

$$H_2 + \frac{1}{2}O_2 \rightarrow H_2O \qquad (1.6)$$

Methane is regarded as one of the most suitable fuels for SOFCs since it is easily accessible, plentiful, affordable, and has a delivery system that is already in place. Methane steam reforming process is used in SOFCs rather than the direct electrochemical oxidation of hydrocarbons like methane because of the potential for carbon production. Even when methane is directly electrochemically oxidised, less carbon is broken down than with higher hydrocarbon fuels. Hydrogen and carbon monoxide are produced when methane and steam interact. Methane steam reforming is the term for the reaction. The water gas shift reaction (WGS) is the name given to the process when carbon monoxide further combines with steam to form hydrogen[128]–[130].

The Solid Oxide Fuel Cell (SOFC) is emerging as a promising option as global research and development efforts concentrate on the need for low-emission, long-lasting, and affordable substitutes for conventional sources of energy. The SOFCs have received a lot of attention in recent years because of their high conversion efficiency, which can exceed 50%. In addition, SOFC has many advantages over other fuel cell technologies, including high power density, internal hydrocarbon reforming, and fuel adaptability.

Since the flow-field geometry greatly influences the transport of the reactant gases as well as the transfers of heat and momentum, the SOFC performance might vary dramatically depending on the interconnector design. The interconnector's configuration has a significant impact on a stack's performance and lifespan, according to recent experimental and numerical studies. However,

research on the impact of flow field design on SOFC performance is limited. Therefore, to bridge this gap and understand the physics of the interconnector design impact on the cell performance, a complete optimal 3D investigation is conducted on different novel interconnector configurations.

1.7 Summary

This chapter covered the description of the fuel cell, its operating system, and how different fuel cell types perform. An emphasis was placed on the SOFC's development history, component materials, configurations, and use of various fuels. The most often utilised materials are YSZ electrolyte, YSZ/Ni anode, and LSM cathode. The planar SOFC has a higher power density, is easy to construct, and can be easily shaped into a variety of configurations. The hydrogen is utilised as fuel. In SOFCs, steam reforming of hydrocarbon fuels like methane is possible because to the high working temperate. The motivation for the present study is explained in a lucid way.

CHAPTER 2

Literature Review

The issues associated with SOFC performance are the main emphasis of the current chapter, which provides an overview of the state of the art in SOFC model development. The chapter is divided into two main sections: part 2.1, which deals with experimental work, and section 2.2, which deals with numerical analyses.

2.1 Experimental Work

The factors affecting SOFC performance are intricate, and it takes time and money to run experiments to study them. To better understand and improve the precision of CFD models, some information and important factors, such as the electrochemical performance of the cell, should be obtained experimentally and utilized to compare the simulation results. The experimental tests that were carried out to determine the electrochemical and thermal performance of SOFCs are reviewed in the sections that follow. This study excludes the experimental effort done to develop and examine the impact of new materials on SOFC performance.

2.1.1 Electrochemical Performance

The studies were carried out to find out how operation temperature affected the electrochemical performance of the cell[131]–[134]. As illustrated in Figure 2.1, it was discovered that at high operating temperatures, current density and power generation are higher. The effect of temperature and pressure on the performance of the cell was researched by Seidler et al.[135]. Their findings showed that temperature has a greater impact on the performance of the cell than pressure; nevertheless, at high pressure, an increase in temperature is more advantageous, as shown in Figure 2.2.

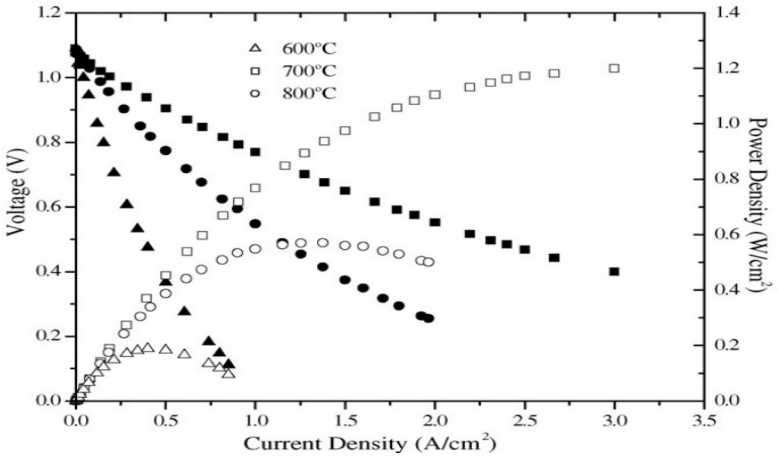

FIGURE 2. 1: Polarization curve depicting the effect of different operating temperature[135]

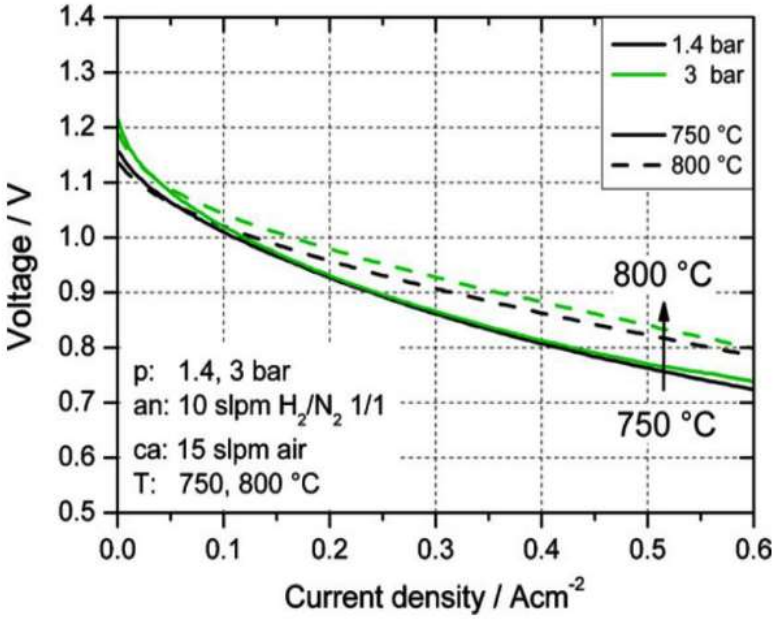

FIGURE 2.2: Polarization curve depicting the effect of different operating pressures and temperature[135]

Jung et al. [136] and Luo et al. [137] conducted analyses of the impact of contact resistance on cell performance. The electron flow is hampered by a rise in resistance, which lowers the cell's current density. It was hypothesized that by using the proper compressive load, contact resistance may be decreased.

The effect of diffusion losses is more pronounced at lower hydrogen concentrations/higher current densities, according to Bedogni et al. [138]. Investigations into the effects of various fuel compositions and mass flow rates revealed that the operating conditions have an impact on the performance of fuel cells. Microtubular (MT) SOFCs were the subject of experimental and numerical research by Lawlor et al. [139] that took into account the effects of co-flow, counter flow, and cross flow configurations. The findings demonstrated that the flow regime had no discernible influence on the electrical performance and temperature distribution for any of the three designs. Further research is required since it was unclear why the temperature was consistently greater just above the core of the MT-SOFC.

2.1.2 Thermal Performance

By using the X-ray diffraction method, Yakabe et al. [140] and Fischer et al.[141] calculated the residual stresses in the electrolyte of anode supported SOFCs. According to Yano et al.[142] observations, the exothermic process taking place in the anode can cause the temperature of solid electrolyte in a single chamber SOFC to reach as high as 850 °C. The exothermic reaction that takes place at the anode/electrolyte interface is what causes the cell temperature to be higher than the furnace temperature, as shown by Y.Leo et al.[143]. The relationship between fuel cell and furnace temperatures is shown in Figure 2.3.

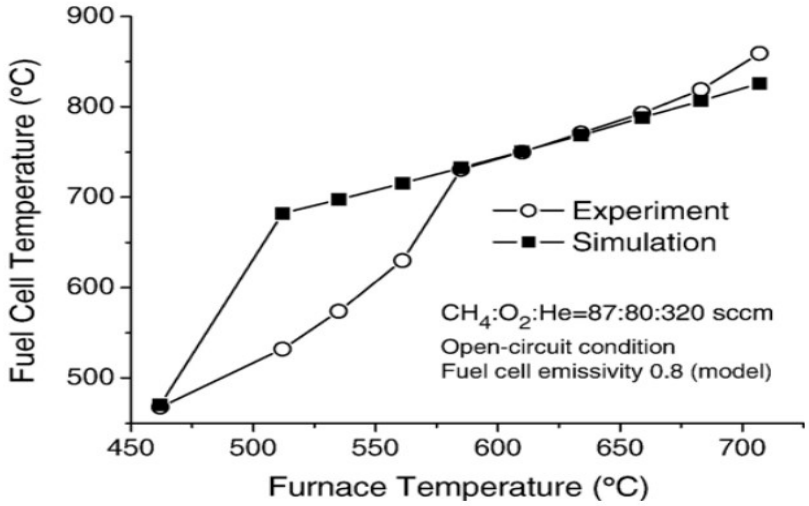

FIGURE 2. 3: Fuel cell temperature Vs Furnace temperature[143]

The impact of current density on temperature distribution and cell performance was investigated by Razbani et al.[144]. The top right corner of the cell was where the highest temperature was found (air inlet and fuel outlet corner). Due to more polarisation at higher current densities, temperature gradient increased as current density increased. The results showed that the fuel cell operates more effectively at higher oven temperatures, citing a more even dispersion of heat and reduced polarisation. According to Morel et al.[145] prediction, the partial and total oxidation of methane at the anode is what causes the temperature rise at the anode's input, which causes the temperature gradient in SOFC. Fracture analysis was carried out on an electrolyte-supported SOFC in the context of an actual operational system by Y. Kim, et al. [146]. Due to the significant mismatch between the thermal expansion coefficient of the electrolyte and the anode, cracks are more prone to develop. For stacks that have been in operation for more than 4,000 hours, it has been noted that leakage around some cracks might lead to structural changes in the anode, which may start the fuel burning locally. Burning fuel raises temperature, increases water and oxygen concentrations, and can oxidise nickel.

2.2 Numerical Studies

The SOFC is a complex system involving an amalgam of several electrochemical reactions with thermal-fluid-electrical interactions. This complex nature of the equations results in non-linearity, which hinders understanding the principles and the governing equations directly with experimentation[147]. Theoretical models such as simulation modeling will be a fetching tool to understand the electrochemical behaviour and design efficient SOFCs[148]. Therefore the present section uses a simulation environment to investigate the power density distribution, temperature distribution, and fuel/oxidizer concentration for a trapezoidal interconnector design by simultaneous consideration of detailed mass and heat transfers, fluid movement, and electrochemical reactions. The performance of SOFC is dictated by material conductivity[149][150], catalyst reaction rates[151]–[153], fuel composition[154], [155], and interconnector configuration[156], [157]. The interconnector plays a significant role in improving the cell performance as it connects the cells in a stack in series and collects the current produced by the cells. Additionally, it serves as a gas channel for transporting oxidants and fuels,

which can have a considerable impact on cell performance and stack stability as the flow-field geometry appreciably affects the heat and momentum transfer of reactant gases[158].

2.2.1 Numerical models on geometrical configuration

In the past, several numerical simulation studies using ANSYS, COMSOL, and in-house computational codes were designed and employed to forecast the effects of a variety of geometrical configurations and performance constraints of SOFCs[147], [159]–[164]. Few of the simulation studies are presented here.

The importance of rib width on fuel cell efficiency is demonstrated by a 2D mathematical model developed by W. Kong et al. [165]. It was reported that the rib width for anode and cathode should be wisely selected to trade-off between the ohmic resistance loss and species diffusion beneath the ribs.

M. Andersson et al. [166] conducted a 3D finite element method study for optimization of design parameters. It was observed that for compact cell design, the cathode side interconnector has to be designed judiciously as it impacts the current density significantly.

Q. Chen et al. [167] investigated the impact of a unique bi-layer interconnector on SOFC performance using a two-dimensional model. It was observed that this design results in a reduction of concentration potential compared to a conventional parallel single-channel interconnector. The limitation of this design is associated increase in the pressure drop.

T. M. M. Heenan et al. [168] analyzed the reason for the malfunction of a SOFC stack during startup. It was accessed from the failure investigation that the design of the interconnector has a major role in the reduction of NiO to Ni. As a result, researchers must devise a novel Bi-polar plate/interconnector design to mitigate the complexity of the oxide gradient at the land–channel interaction region.

A. N. Celik [169] used COMSOL multi-physics to create a 3D model of a planar SOFC with conventional parallel rectangular flow channels to have a better understanding of the cell's temperature and flow distribution. It was discovered that as the inflow molar concentration of hydrogen increases, the temperature rises but the average velocity of fuel and oxidizer falls. The same trend was also observed for the increase in the inlet molar concentration of oxygen.

The effect of various flow channel geometries on SOFC performance has been investigated by many researchers. To mention a few, the work carried out by Khazaee and Rava [170] is highlighted, where the flow channel configuration has been found to have a considerable impact on the accurate distribution of reactants in the reaction site. (i.e. TPB region). Their research revealed that rectangular geometries are more efficient than those with triangle or trapezoidal geometries. Furthermore, the data revealed that the trapezoidal channel has a greater molar fraction of hydrogen compared to rectangular and triangular flow channels. Similarly, Manglik and Magar[171] presented computational simulations of heat and mass transport on an anode-supported SOFC module with rectangular, triangular, and trapezoidal interconnectors. It was reported that rectangular interconnectors are better for thermal management, whereas trapezoidal or triangular interconnectors are better for higher fuel consumption and structural support in a SOFC stack.

Lin et al.[172] used a computational model to investigate the impact of rib width on planar SOFC concentration polarization. It was reported that when the rib width is large, ohmic polarization reduced, while concentration polarization increased.

In another similar study, Lin et al.[173] predominantly concentrated on the design of interconnector ribs. Based on their findings, they reported that for a particular area-specific contact resistance, the optimal width of the rib is linear to the pitch width, and with narrow rib widths a homogeneous gas concentration can be achieved. Rectangular channel configuration is the conventional design adopted by many researchers in experimental studies due to the ease in machinability of channels.

S.Zeng et al. [174] presented an optimized rectangular channel for gas transport and flow collection with an emphasis on the cathode support layer porosity impact on cell performance. The findings illustrated that broader and thinner gas channels reduce the cell current density slightly, but dramatically increase the volumetric current in the cell.

D. Bhattacharya et al.[175] examined the performance characteristics of the conventional straight rectangular channel and rectangular serpentine channel geometries for a 3D anode supported planar SOFC. It was observed that flow channels with serpentine configurations were found to outperform rectangular channels in terms of power output and fuel consumption, but they did increase the average temperature of the cells and created an extremely high pressure drop. A similar study on SOFC performance with helical, single-entry serpentine parallel, modified

parallel, 2-pass serpentine, and 3-pass serpentine flow channels was numerically evaluated by Saied et al.[164]. According to their research findings, for a three-pass serpentine configuration, fuel and oxygen were distributed over the active surface area uniformly, resulting in a high current of about 23.3 A, which is 5.18 % greater than other designs investigated. A constraining feature of this design is that the variations in the pressure drop and the peak temperature the cell experiences as a result of this design arrangement are not explored.

In the literature, various innovative configurations of the interconnector, apart from the conventional rectangular design of SOFC have also been studied. For example, Kong et al.[176] developed a new interconnector design based on staggered X-type patterns. The results demonstrated that independent of the porous anode and porous cathode porosity, the X-type configuration enhances performance due to a shorter current collection route. Similarly, Gao et al.[177] designed interconnectors with distributed cylindrical patterns. Based on their research findings, they concluded that an optimum rib size exists for fixed contact resistances and pitch widths.

As an alternative, Fu et al. [178] proposed grooved and rib-finned interconnect for SOFCs. As a result of the novel interconnectors, cell performance was improved due to a decrease in activation overpotential and concentration overpotential.

2.2.2 Numerical models on flow direction

In addition to the type of flow channel, the flow configuration plays a crucial role in flow uniformity. In this context, few studies were reported on the consequence of flow direction on cell performance. Y. J. Kim and M. C. Lee [179] investigated the influence of parallel, counter, and perpendicular flow directions on cell performance, and it was discovered that parallel flow arrangement produces the best cell performance. This is due to the reduction in overpotential compared to other flow directions. Whereas on the other hand K. P. Recknagle et al. [180] suggested that though the parallel flow direction provides the uniform temperature distribution, the highest power density is produced by counter flow design. Moreover, a counter-flow configuration has been reported to provide stable and enduring operation for SOFCs by Schluckner et al.[181].

A similar study was also reported by Zhang et al.[182] in which the performance of planar SOFC with 3 distinct flow designs (parallel flow, counter-flow, and cross-flow) was assessed. The results of the study have concluded that counter-flow configurations perform better than parallel flow and cross-flow configurations. To take the advantage of counter flow design one has to focus on the reduction of non-uniform temperature distribution encountered in this design. For this reason, in the present study, we have considered the counter flow configuration and tried to address the non-uniform temperature distribution by varying the channel geometrical configuration.

2.3 Summary

The following conclusions are drawn from a survey of the literature on experimental and numerical investigations on SOFC development. The mechanisms underlying the SOFC's electrochemical performance were the main subject of experimental study. However, because of the technical challenges, experimental measurements of species concentrations and temperature distributions are rare and there are no relevant data to use as a reference.

Investigating the mechanics of reacting flows, such as the transit of mass, heat, and momentum as well as chemical reactions that affect cell performance, is best done using computational models. By contrasting the simulation findings (which simulated the electrochemical mechanisms) with experimental data, the cell performances of numerical models were examined. The models were created to examine how the cell performance was impacted by the geometrical factors and flow configurations. The performance of the cell is influenced by its geometrical and material characteristics, hence optimized design parameters should be used. The operating temperature has a significant impact on the operation of the cell, according to simulations of the modeling process. The SOFCs are high temperature fuel cells (600–1000 °C), and because of the temperature difference between the cell and the surrounding environment, the cell experiences thermal stresses. To find the high stress locations that can lead to cell collapse, thermal stress generation is necessary.

The literature analysis showed that the current models take into account the thermal characteristics of the materials and fluids as the constants implied by the operating temperature. However, with SOFCs, exothermic electrochemical reactions cause the reacting fluxes in the cell

to form a temperature distribution, which makes the local temperature different from the operational temperature, which is held constant once cell operation conditions are known. When calculating the thermal properties of the fluids and materials for modeling cell performance, particularly the thermal impacts, it is evident that this discrepancy must be carefully taken into account. Also from the extensive literature survey, it is observed that the various methods adopted by researchers for performance enhancement of fuel cells are: (i) Optimization of flow channel/ interconnector configuration [183], [184], (ii) Insertion of obstacles of different shapes in the flow path[185], [186], (iii) Alternation of operating parameters[187].

The knowledge gaps discovered through literature reviews are as follows.

1) The current collector which not only collects electric current but also offers passages for reactants needs to be explored explicitly in SOFCs.

2) At the component level, a channel network with a wider or deeper channels towards the stack inlet can be studied as it may allow for greater partial pressure control and uniformity throughout the stack.

3) The contact resistance which is an important factor limiting the SOFC performance needs to be explored.

4) The channel inlet designs and flow arrangements for planar SOFC stacks still need further investigations to achieve an effective temperature gradient reduction.

To bridge the above gaps, the following objectives were designed with an emphasis to improve the SOFC performance.

1) To simulate and compare the performance of novel Trapezoidal interconnector (TI) with a wider channel width and narrow rib width against the Conventional rectangular interconnector (CRI) SOFC by considering all the multi physics involved in a typical SOFC.

2) To thoroughly understand the effect of different operating temperatures on the electrochemical reactions and cell performance for a TI design.

3) To study the effect of the rhombohedral interconnector placed in a staggered orientation called as Staggered Rhombohedral Interconnector (SRhI) on the mass transfer, ohmic losses and cell performance.

4) Carry out a parametric study on SRhI configuration by varying the inlet mass flow rates.

The following chapters provide information about the studies in detail.

CHAPTER 3

Mathematical Modeling

This chapter presents the partial differential equations required in modeling the physics of a fuel cell. To account for the arrangement of the counter-flow, from one side of the channel, hydrogen enters the anode part, while air enters the cathode part from the other end. The hydrogen and air then diffuse along the porous anode and the porous cathode in accordance with the species conservation equations and reaches the electrolyte where the potential of the cell is determined using formulae in Section Cell potential.

3.1 Cell Potential

The electrochemical reactions taking place at the triple phase boundary (TPB) of anode and cathode layers are:

$$H_2 + O^{2-} \leftrightarrow H_2O + 2e^- \quad \text{(anode TPB)} \tag{3.1}$$

$$\frac{1}{2}O_2 + 2e^- \leftrightarrow O^{2-} \quad \text{(cathode TPB)} \tag{3.2}$$

The electric field potential is calculated based on the conservation of charges using the Laplace equation as follows:

$$\vec{\nabla} \cdot (\sigma \nabla \phi) = 0 \tag{3.3}$$

where ϕ indicates the electrical potential and σdenotes the electric conductivity.

The ideal voltage, also known as reversible cell voltage, is calculated in the absence of an electric load using the Nernst equation as:

$$\phi_{\text{ideal}} = \phi^0 + \frac{RT}{2F} \ln\left(\frac{p_{H_2} p_{O_2}^{0.5}}{p_{H_2O}}\right) \tag{3.4}$$

where ϕ^0 denotes the open-circuit voltage.

In the present study, the concept of voltage "jump" is used to model the electrochemistry aspect of the cell. To associate the potential field with the electrochemical behaviour, all electrochemical effects are incorporated in the jump condition. The following is how this interface condition is defined [188]:

$$\phi_{cell} = \phi_{jump} - \eta_s \tag{3.5}$$

Where η_s correspond to conducting section ohmic losses and

$$\phi_{jump} = \phi_{ideal} - \eta_{act,a} - \eta_{act,c} - \eta_{ele} \tag{3.6}$$

Where η_{ele} denotes the electrolyte ohmic potential loss, $\eta_{act,a}$ and $\eta_{act,c}$ denotes the anode and cathode activation overpotential, respectively.

The following Butler-Volmer formulae are used to calculate the rates of anodic and cathodic reactions [188]:

$$I_{an} = I_{o,ref}^{an} \left(\frac{X_{H_2}}{X_{H_{2,ref}}}\right)^{\gamma_{H_2}} \left(\frac{X_{H_2O}}{X_{H_2O,ref}}\right)^{\gamma_{H_2O}} \left(e^{\frac{\alpha_{an} F \eta_{an}}{RT}} - e^{\frac{-\alpha_{cat} F \eta_{cat}}{RT}}\right) \tag{3.7}$$

$$I_{cat} = I_{o,ref}^{cat} \left(\frac{X_{O_2}}{X_{O_{2,ref}}}\right)^{\gamma_{O_2}} \left(-e^{\frac{\alpha_{an} F \eta_{an}}{RT}} + e^{\frac{-\alpha_{cat} F \eta_{cat}}{RT}}\right) \tag{3.8}$$

where $I_{o,ref}^{an}$ and $I_{o,ref}^{cat}$ are the reference current densities for anode and cathode, The X represents each species mole fractions, while γ represents each species concentration exponents. Equations (3)-(8) are used to calculate the activation overpotential on the cathode and anode sides.

3.2 Equations of Mass Conservation:

The equation for mass conservation in a steady state is as follows:

$$\vec{\nabla} \cdot \left(\rho \vec{v}\right) = S_m \tag{3.9}$$

where S_m represents mass source term and except for the reaction sites, it is zero across the domain.

The mass source term includes the species interactions which are calculated using Faraday's second law of electrolysis as follows:

$$S_m = \frac{aI}{nF} \tag{3.10}$$

where 'a' represents each species stoichiometric coefficient, 'I' denotes current density, 'n' indicates the number of electrons per mole of fuel, and 'F' represents the Faraday's constant.

To the cells near the electrolyte contact, the following species fluxes are applied:

$$S_{O_2} = -\frac{I}{4F} \tag{3.11}$$

$$S_{H_2} = -\frac{I}{2F} \tag{3.12}$$

$$S_{H_2O} = \frac{I}{2F} \tag{3.13}$$

3.3 Equations of Momentum Conservation

The steady-state momentum conservation equation is as follows for low Reynolds numbers and small gravitational forces:

$$\vec{\nabla} . \left(\rho \vec{v} \vec{v}\right) = -\nabla P + \vec{\nabla} \cdot \vec{\tau} + \vec{S} \tag{3.14}$$

where $\vec{\tau}$ represents viscous stress tensor and

$$\vec{\nabla} \cdot \vec{\tau} = \mu \nabla^2 \vec{v} \tag{3.15}$$

where μdenotes the dynamic viscosity of the fluid. The source term, $\vec{S}$ in Eq. (14) is zero in all the flow channels. It is, nevertheless, used to keep track of increased pressure drop in porous media when calculating flow. Two separate mechanisms, viscous and inertial resistance, contribute to pressure drop within porous media. For a homogeneous porous media, assuming that inertial losses are trivial compared to viscous losses, the source term is calculated as:

$$\vec{S} = -\frac{\mu}{\alpha} \vec{v} \tag{3.16}$$

3.4 Equations of Energy Conservation

The equation for energy conservation in a steady-state condition is as follows:

$$\vec{\nabla} . \left(\vec{v} \left(\rho E + P \right) \right) = \vec{\nabla} . \left(k_{eff} \nabla \mathrm{T} \quad - \sum_{\mathrm{i}} \mathrm{h_i} \vec{J_i} \right) + S_h \tag{3.17}$$

where E denotes specific total energy. If the change in specific kinetic energy is negligible, E equals the internal energy, and then the energy equation is expressed in its simplest form as:

$$\vec{\nabla} . \left(\vec{v} \left(\rho h \right) \right) = \vec{\nabla} . \left(k_{eff} \nabla \mathrm{T} - \sum_{\mathrm{i}} \mathrm{h_i} \vec{J_i} \right) + S_h \tag{3.18}$$

where h denoted specific enthalpy and $k_{eff}$is the effective thermal conductivity in the porous zone, which is calculated using the following equation:

$$k_{eff} = \varepsilon k_f + (1 - \varepsilon) k_s \tag{3.19}$$

where ε is the porosity of the porous media. Furthermore, the subscripts *s* and *f* signify solid and fluid states, respectively. The species flux, J_i , will be described in the next section.

In the electrically conducting domains, the source term is calculated as follows:

$$S_h = R_{ohmic} i^2 \tag{3.20}$$

3.5 Species Conservation Equations

In the computational domain, there are four distinct species: H_2, O_2, H_2O, and N_2. As a result, three transport equations must be solved. The diffusion equation in its convective form can be used to compute the mass concentration of each species:

$$\vec{\nabla} . \left(\rho Y_i \vec{v}\right) = -\vec{\nabla} \cdot \vec{J_i} + S_i \quad (3.21)$$

The convective terms are represented on the left-hand side of the equation, with Y_i denoting each species mass concentration. $S_i$denotes the source term due to chemical reactions, while J_i represents diffusive flux.

The flux of species i in a mixture with N component can be attributed to the concentration and temperature gradient using Fick's equation of diffusion as follows:

$$\vec{J_i} = -\rho D_{i,m} \nabla \mathrm{Y_i} - \mathrm{D_{i,T}} \frac{\nabla \mathrm{T}}{\mathrm{T}} \quad (3.22)$$

The multi-component diffusion approach based on the Stefan-Maxwell equations is employed in the current investigation to get more precise results.

$$\vec{J_i} = -\sum_{\mathrm{j=1}}^{\mathrm{N-1}} \rho\, D_{ij} \nabla \mathrm{Y_j} - \mathrm{D_{i,T}} \frac{\nabla \mathrm{T}}{\mathrm{T}} \quad (3.23)$$

where $\mathrm{D_{i,T}}$ denotes each species thermal diffusion coefficient and D_{ij} denotes generalized Fick's law diffusion coefficients matrix which is calculated as follows:

$$D_{ij} = [A^{-1}][B] \quad (3.24)$$

The diffusion coefficients discovered by Fick's law can not be used to simulate diffusion in porous media directly. Taking into account the porous consequences, the following correction approach is used:

$$D_{ij}^{eff} = \frac{\varepsilon}{\tau} D_{ij} \quad (3.25)$$

where the terms τ and ε denote tortuosity and porosity respectively.

Finally, in Eq. (21) the source terms are determined as below:

$$S_{O_2} = -\frac{I M_{w,O_2}}{4F} \quad (3.26)$$

$$S_{H_2} = -\frac{IM_{w,H_2}}{2F} \quad (3.27)$$

$$S_{H_2O} = \frac{IM_{w,H_2O}}{2F} \quad (3.28)$$

3.6. Methodology

The geometrical design was created using Solidworks 2010, a 3D CAD design software and then the numerical study was performed using commercial ANSYS FLUENT. To model the fluid-thermo-electric properties in conjunction with the electro-chemical reactions ANSYS FLUENT with an add-on-module named **SOFC with an unresolved electrolyte model** is employed. To simplify the complex electro-chemical equations of SOFC, the following assumptions were made:

- The porous anode and porous cathode were assumed to be homogeneous and isotropic.
- The fluid flow was considered laminar and incompressible because of moderate pressure differential, flow channel, and low flow velocities.
- It is assumed that the gas sealing is perfect.
- The gaseous fluids in the SOFC were considered to be ideal gases, and their heat capacities are only a function of temperature.
- Without taking into account the inlet and outlet port design, the flow field at the interconnector inlet is assumed uniform in this model.

3.7 Boundary Conditions and Input Parameters

The input material parameters and operating conditions for the proposed models are shown in Table 3.1 and Table 3.2 respectively. The electrical potential at the anode tap is set to zero, while the electrical potential at the cathode tap is set to an equal value to the cell operating current.

TABLE 3.1 Material attributes for validation study (Sembler and Kumar [189]) and Present study:

Porous anode (NiO + YSZ)	Density	6500 kg/m^3

	Specific heat	450 J/kgK
	Thermal conductivity	10 W/mK
	Viscous resistance	$1e^{+13} m^{-2}$
	Electron conductivity	333 330 $\Omega^{-1}. m^{-1}$
	Porosity	0.24
	Tortuosity	3
	Anode transfer coefficient	0.7
	Cathode transfer coefficient	0.7
	Exchange current density	200 000 A/m^2
Porous cathode (LSM)	Density	5620 kg/m^3
	Specific heat	450 J /kgK
	Thermal conductivity	11 W/mK
	Viscous resistance	$1e^{+13} m^{-2}$
	Electron conductivity	7937 W/mK
	Porosity	0.375
	Tortuosity	3
	Anode transfer coefficient	0.7
	Cathode transfer coefficient	0.7
	Exchange current density	800 A/m^2
Electrolyte (YSZ)	Density	5480 kg/m^3
	Specific heat	450 J /kgK
	Thermal conductivity	2 W/mK
	Resistivity	0.1 Ω.m
Interconnector (metal)	Density	8900 kg/m^3
	Specific heat	450 J /kgK
	Thermal conductivity	72 W/mK
	Electron conductivity	$1.5e^{+07} \Omega^{-1}. m^{-1}$
	Anode contact resistance	$1e^{-07} \Omega . m^2$
	Cathode contact resistance	$1e^{-07} \Omega .m^2$

TABLE 3.2 Flow channel boundary conditions for validation study (S.S Wei et al., [190]; Sembler and Kumar [189]) and Present study:

Anode mass flow rate	4.48 e^{-07} kg/s
Cathode mass flow rate	2.17 e^{-05} kg/s
Anode inlet temperature	1123 K
Cathode inlet temperature	1123 K
Anode flow composition	97% H_2, 3% H_2O (% mole)
Cathode flow composition	Dry air
Cell operating pressure	1 atm
External boundaries	Adiabatic
Electric potential at anode tap	$\phi = 0$
Electric potential at cathode tap	$i = I_{cell}$

3.8 Summary

The coupling mechanism and geometries of the planar anode-supported SOFC were described in detail in this chapter. It specifies the assumptions used to model the cell. It explains the governing equations. The electrochemical and chemical processes' underlying mechanisms are listed. The relationships used in the mechanical and thermal stresses' calculation are described. The boundary constraints are highlighted at the conclusion.

CHAPTER 4

Performance Evaluation of a Trapezoidal Interconnector Configuration of Solid Oxide Fuel Cell

The models discussed in Chapter 4 is used in simulations of a planar SOFC operating on hydrogen and the effects of temperature on the operation of the cell. Comparing the numerical results to the available experimental studies allows for their validation. It is analyzed and described how various parameters affect the electrochemical and thermal performance of the cell.

4.1 Introduction

In the present study, a full-scale 50 mm x 50 mm active area trapezoidal channel interconnector for anode and cathode is simulated with all the multi-physics involved considering the flow of fuel and air to be counter flow direction. The trapezoidal channel interconnector performance is compared to the conventional parallel rectangular interconnector configuration. Along with changing the angle, in this article, the dimensions of channels and rib were also varied which are also the important factors that are impacting the anode-supported SOFC performance. As anode supported fuel cell is more sensitive to oxygen diffusion under the rib area, a study is also undertaken to access the influence of rib width on the anode side fuel transport by designing a SOFC with a **rectangular parallel anode interconnector** and a **trapezoidal cathode interconnector**. In the literature, different shapes of flow channels like rectangular, triangular, and trapezoidal were studied[161], [170]. But the effects of the parametric study in relation to non-uniform channel width and rib width, pressure drop, and reactants velocity changes on SOFC performance were not focused. In the present study, a trapezoidal interconnector with wider channel width and a narrow rib is chosen for simulation because it has the following advantages: (a) As the trapezoidal interconnector offers wider channel width it may aid in uniform distribution and higher reactant gas penetration. (b) A narrow rib offers minimum

contact area, so it may provide an easy path for the reactants to permeate in the region located near the rib leading to minimizing concentration polarization losses. (c) The slant portion of the trapezoidal channel might aid in velocity control by forming small eddies. (d) A trapezoidal interconnector designed with the chosen dimensions of channel width and rib width may address the problem of non-uniform temperature distribution encountered in the counter-flow direction as reported in the literature[180].

The specific objectives of the present study are: (a) To understand the effect of the Trapezoidal channel with varied channel and rib width (i.e. wider channel and narrow rib width) on cell performance in an anode-supported SOFC. (b) Determine the impact of rib area on anode and cathode reactants transportation. (c) To reduce the operating temperature of SOFC by changing the interconnector configuration from CRI to TI with reduced rib width such that better heat management is attained in the cell.

4.2 Numerical implementation

4.2.1 Geometry

The model consists of an anode, electrolyte, cathode, and interconnector. To validate the Trapezoidal Interconnector (TI) concept shown in Figure 4.1, we first modeled a rectangle parallel interconnector, often known as the Conventional Rectangular Interconnector (CRI), depicted in Figure 4.2, with the same dimensions as the references.[189], [190] Since the channel configuration was proposed to change from rectangular to trapezoidal, the dimensions of the active electrolyte surface area were fixed as those of the reference studies (i.e. 50x50 mm^2) for **comparison** while maintaining the hydraulic diameter for the trapezoidal channel to be the same as that of the rectangular channel. The only attribute changed is the channel configuration. Instead of a straight parallel channel, a taper of 75^o is given to the vertical edge of the channels making it a trapezoidal channel with a wider channel width of 1.5mm and narrow rib width of 0.5mm.[184] The taper angle of 75^o is chosen from the work reported by R. M. Manglik and Y. N. Magar[171], where triangular channel, a trapezoidal channel with internal inclination angles(Θ) of 60^o and 75^o, and rectangular channel were studied and it was reported that: (a) As Θ increases, the heat transfer or Nusselt characteristics increases from $\Theta = 45^o$ to 90^o with a

significant change observed when Θ changes from 60 ^{o} to 75 ^{o} for a trapezoidal channel. (b) The ratio Nu/fRe which was used as a measure of the relative surface-area compactness or increased convective heat transfer surface-area density showed a drastic increase for Θ = 60 ^{o} to 75 ^{o} after which the change is almost linear with an increase in Θ up to 90 ^{o}. Thus to take the advantage of increased heat transfer, increased convective heat transfer surface-area density and to maintain the hydraulic diameter of the trapezoidal channel as that of a rectangular channel, the 75^{o} is chosen as the taper angle for the present trapezoidal interconnector. The dimensions of the cell is shown in table 4.1.

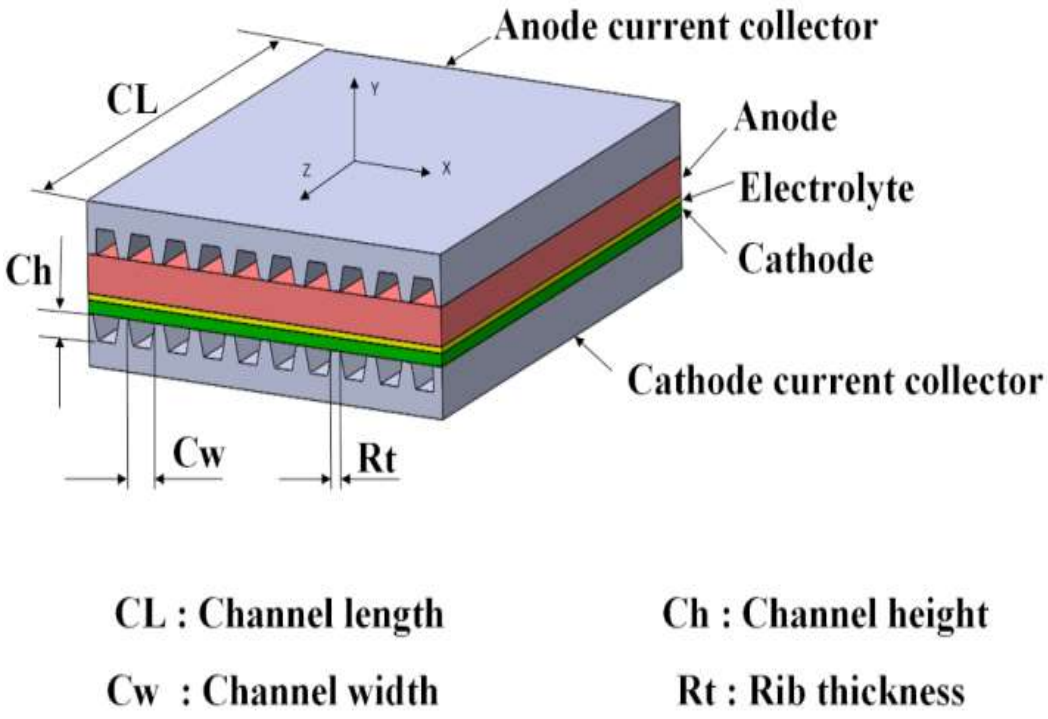

FIGURE 4. 1: SOFC with trapezoidal interconnector configuration (Present study).

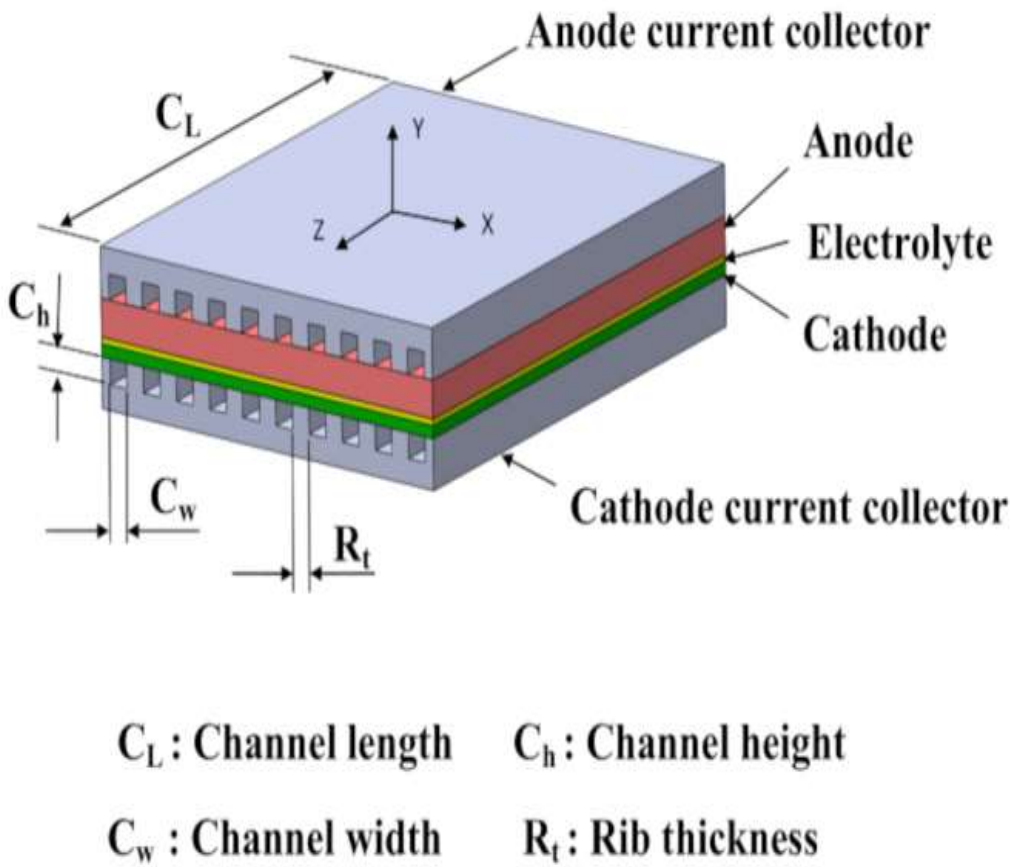

FIGURE 4. 2: SOFC with conventional rectangular interconnector (CRI) configuration (Validation study).

4.2.2 Meshing

The meshing of the computational domain was done in ANSYS software using hexahedral elements. Based on Sembler and Kumar [189] grid independence analysis, the entire domain was divided into discrete elements. The global mesh size of 0.5mm is used for the entire domain discretization, followed by edge sizing along the thickness direction of the cell to ensure that even the thinnest component has a good number of elements and no important information is lost. The mesh for the computational domain is shown in Figure 4.3, with the meshes for the anode and cathode domains clearly noticeable in the magnified version.

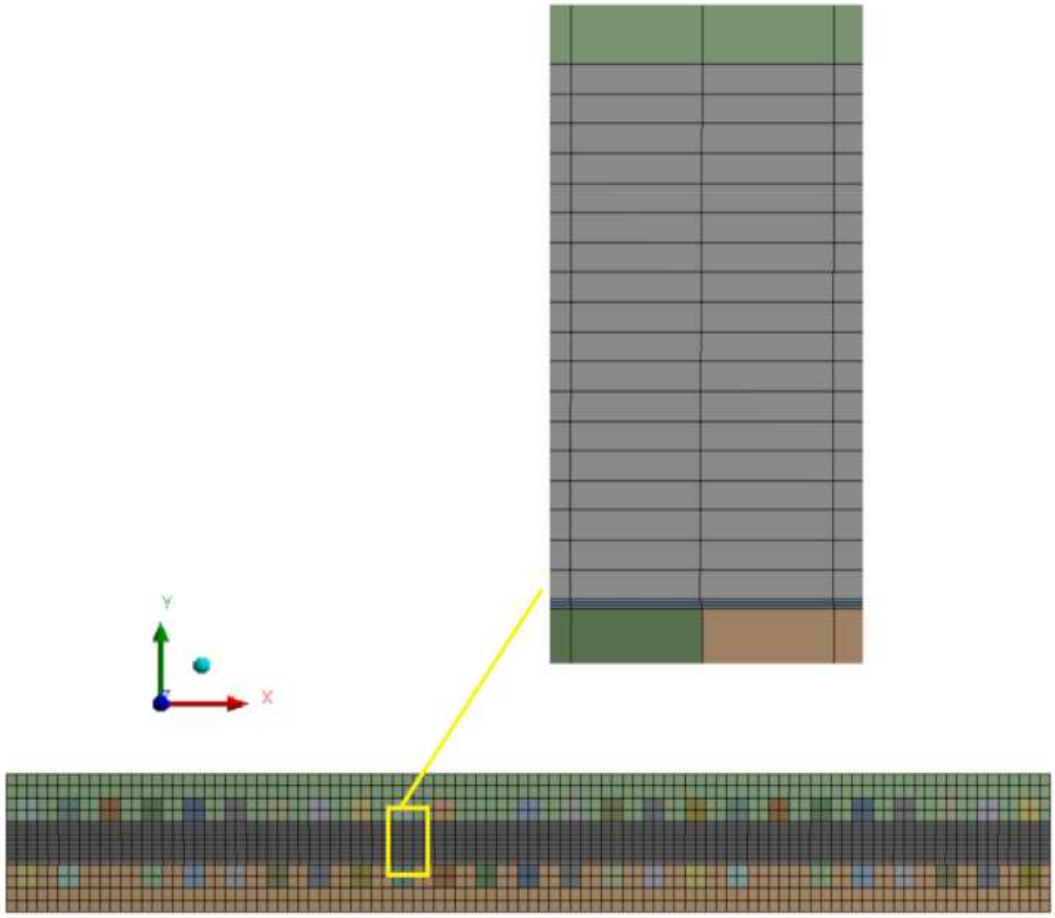

FIGURE 4. 3: Computational Mesh Domain

TABLE 4. 1 Dimensions of SOFC used for validation study (S.S Wei et al., [190]; Sembler and Kumar [189]) and Present Study:

Factors	**Validation study Magnitude**	**Present Study Magnitude**	**Units**
Channel height (C_h)	1	1	mm
Channel width (C_w)	1	1.5	mm
Channel length (C_L)	50	50	mm
Current collector height above the channels	1	1	mm
Rib thickness (R_t)	1	0.5	mm

Thickness of anode	1.8	1.8	mm
Thickness of cathode	30	30	μm
Thickness of electrolyte (virtual)	20	20	μm

4.2.3 Numerical solution procedure

The continuity, momentum, energy, and species equations in ANSYS FLUENT are solved using the Finite Volume Method (FVM). So, a 3D double precision with steady and pressure-based velocity formulation, coupled algorithm for pressure-velocity coupling is selected to solve the partial differential equations. For spatial discretization of momentum, energy, species, and electric potential second-order UPWIND scheme is selected. As it is a multi-physics problem, the convergence criteria of residuals for all the equations are set to $1e^{-08}$.

4.3 Results and Discussion

To evaluate the proposed trapezoidal interconnector performance, a unit cell was separated into anode, cathode, and flow channel components to simplify the SOFC simulation model. The anode, cathode, and electrolyte used in this work are nickel cermet (NiO +YSZ), LSM, and YSZ respectively.

4.3.1 Grid independence study

For the grid independence study, the initial mesh density for Conventional Rectangular Interconnector was selected following the Sembler and Kumar[189]. The final orthogonal quality of the selected mesh for CRI and TI are 0.98 and 0.91 respectively, which ensures that cell quality is adequate for the further simulation study. For the Trapezoidal Interconnector, a complete grid convergence test was performed using different elements: 139380, 226644, and 438256. The Performance curve obtained with 438256 elements was nearly identical to those of 226644 elements as shown in Figure 4.4. Therefore, for further simulations to reduce the computational time without compromising the accuracy of the result, 226644 elements were employed.

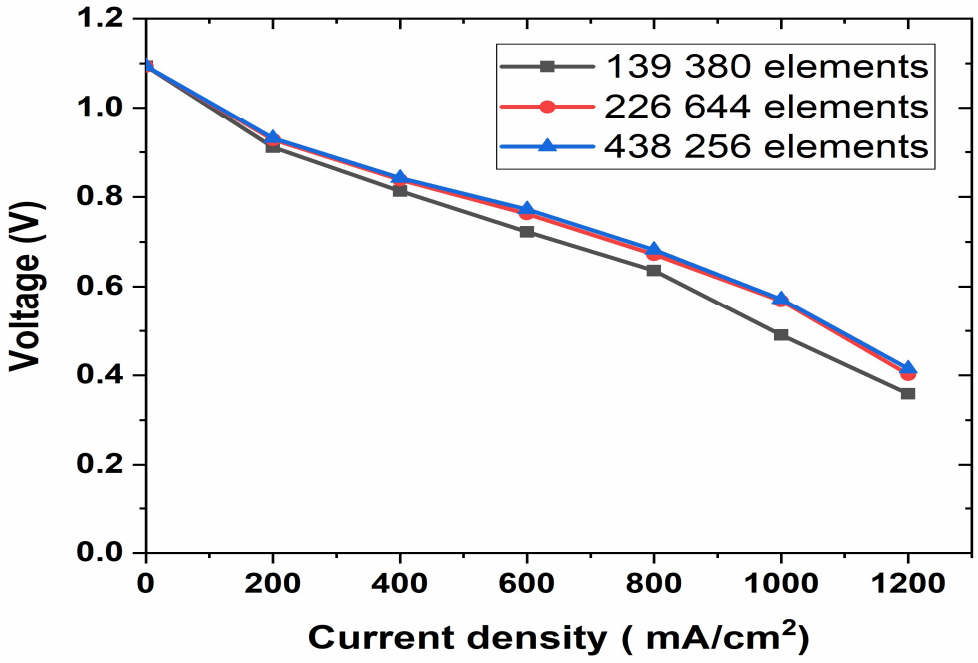

FIGURE 4. 4: Grid Independence study for the trapezoidal interconnector

To confirm the validity of the SOFC model developed in this study, the simulation work in this study is compared to numerical work published by S.S Wei et al.,[190] and experimental work carried out by Sembler and Kumar[189] using the same modeling environment. The simulated I-V and I-P plots are in great agreement at lower current density and higher operating voltages with experimental and numerical studies as shown in Figure 4.5. But at higher current densities and lower operating voltage, a small deviation is observed. A maximum deviation of 9.43% with the experimental study is estimated at 1200 mA/cm^2 current density, whereas the present study results greatly match with the numerical work even at higher current density and lower voltage reported in the literature[190]. The discrepancy observed at higher current density can be accredited to the value of electrolyte resistance assumed in the numerical study. Electrolyte resistance, is in fact, a temperature-dependent property[191]. The temperature rises concurrently with current density, resulting in greater electrolyte resistance and ohmic losses in the experiment[170]. The deviation reported in the present study at higher current densities is consistent with simulation results reported in the literature[192],[193]. Furthermore, the findings

of this investigation, particularly in the lower current density zone, were more congruent with experimental data than the numerical data offered in the literature. As a result, the present numerical model is more reliable in forecasting the performance of the fuel cell.

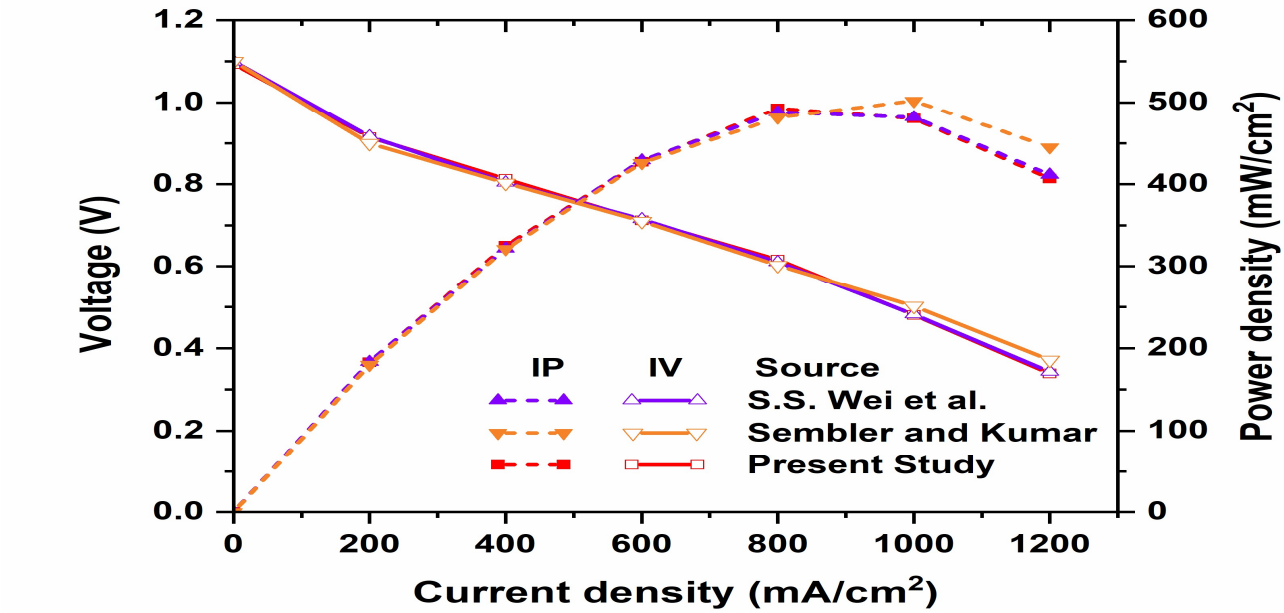

FIGURE 4. 5: Comparison of I-V and I-P curves for validation of the present study versus experimental study by Sembler and Kumar and numerical study by S.S Wei et al. in the literature.

4.3.2 Performance analysis and comparison of SOFCs with TI design against CRI design

The present study aims to illustrate the performance enhancement achieved by adopting the Trapezoidal interconnector (TI). Figure 4.6 shows that the Trapezoidal interconnector has a power density of 567.8 mW/cm^2 at a peak current density of 1000 mA/cm^2 compared to 480.4 mW/cm^{2}for the conventional rectangular interconnector (CRI) design. Thus an increase of 18.2% is obtained with a change in flow channel (interconnector) configuration from rectangular to trapezoidal. Therefore, the trapezoidal interconnector has an advantage over the rectangular interconnector. The reasons for the difference between the Trapezoidal interconnector and conventional rectangular interconnector designs will be examined in the following section.

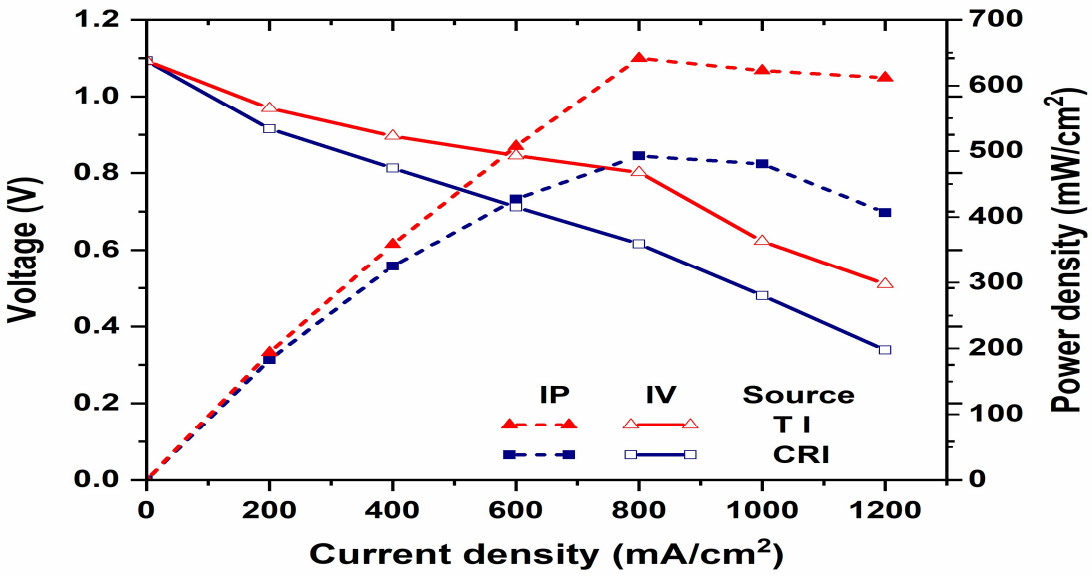

FIGURE 4. 6: Comparison of I-V curve and I-P curve for the Conventional rectangular interconnector and Trapezoidal interconnector design.

4.3.2.1 Oxygen mole fraction distribution

It is reported in the literature that the oxygen concentration under the rib area is very crucial for the anode-supported SOFC[194]–[196]. The trapezoidal interconnector with a wider channel width and narrow rib provides an easy pathway for the oxygen to diffuse in the regions near the rib resulting in enhancement of mass transfer. Figure 4.7 depicts the distribution of the mole fraction of oxygen at the cathode side of the fuel cell at 1000 mA/cm^2. At peak power density, the decrement of mole fraction of oxygen from 0.21 at the entry to 0.12 at the exit along the channel for TI compared to 0.14 for CRI demonstrates better transport of oxygen. This increment in oxygen transport can be attributed to better diffusion achieved by improved consumption of oxygen owing to a decrease in average velocity from 3.643 m/s in CRI to 2.79 m/s in TI at 1000 mA/cm^2 current density[197]. The better oxygen transport obtained in TI can also be justified by the area covered under the rib. The area under the rib for the conventional rectangular channel is 500mm^2 whereas for the Trapezoidal channel the area under the rib is 250mm^2. Based on the effective area exposed for flow transfer, TI is 12.5% more efficient than CRI. To maintain the hydraulic diameter for the trapezoidal channel to be the same as that of the rectangular channel, the mass flow area of the trapezoidal channel increases. From the continuity equation, for a fixed

mass flow rate as the area is increased, the **inlet velocity** will be reduced. As the inlet velocity reduces compared to the inlet velocity attained in the rectangular channel, the fuel consumption increases[161], indicating more diffusion through the porous anode in TI compared to CRI and thereby improving the species transport as well as reaction rates as shown in Figure 4.8.

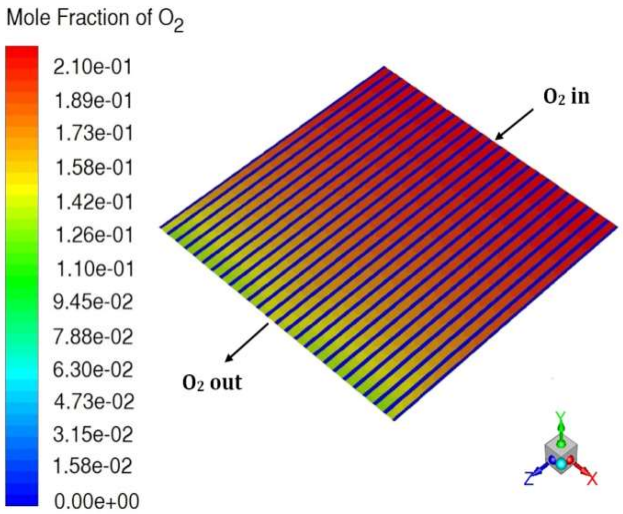

FIGURE 4. 7: Oxygen mole fraction distribution along the cell length at peak current density.

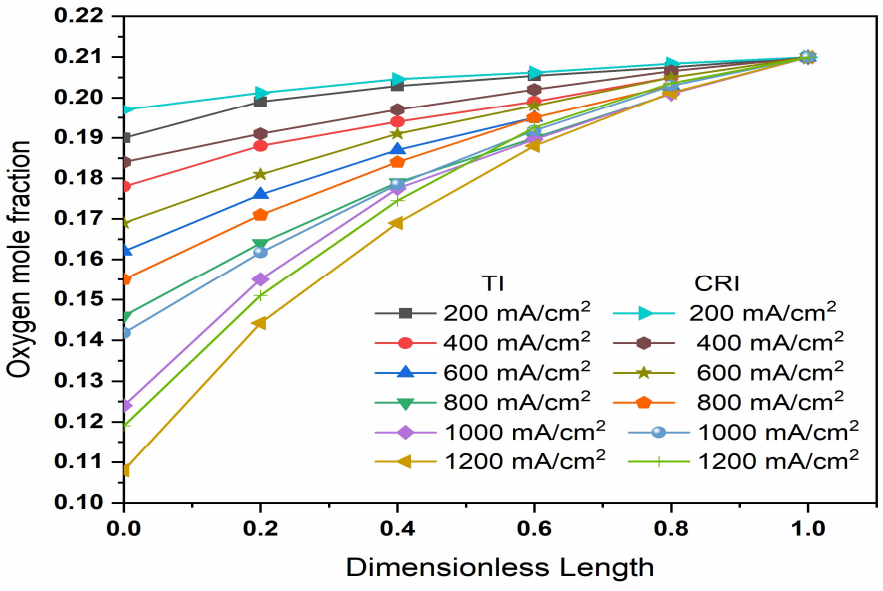

FIGURE 4. 8: Comparison of oxygen mole fraction consumption for TI and CRI design.

4.3.2.2 Hydrogen mole fraction distribution

Figure 4.9 shows the distribution of the mole fraction of hydrogen at the anode side of the fuel cell at 1000 mA/cm^2. The decrement of mole fraction of hydrogen at peak power density from 0.97 at the entry to 0.24 at the exit for TI compared to 0.253 for CRI along the channel demonstrates marginally improved utilization of fuel and species reaction rate compared to CRI. This increment in fuel utilization and species reaction rate can be attributed to improved diffusion achieved by more fuel consumption owing to the decrease in average velocity from 0.932 m/s in CRI to 0.718 m/s in TI at 1000 mA/cm^2 current density. For the CRI design, the rib width is 1mm, whereas for the TI design the rib width is 0.5mm. The increase in cell performance achieved in TI can be credited to the reduction in the current collector path, thereby a decrease in ohmic polarization due to the decrease in rib width. The electrical resistance includes both the ohmic resistance of the rib material and the contact resistance between the ribs and the electrodes. According to the law of resistance, when the width of the rib is decreased for a fixed cell width, the resistances in the rib and the active reaction area will increase. Simultaneously, the concentration overpotential underneath the rib and the contact resistance will decrease. Typically, the contact resistance is much higher than the ohmic resistance of the rib material[173]. So, as rib width is reduced, contact resistance reduces, resulting in a shorter current transmission length[198], [199]. As a result, ohmic polarization is reduced.

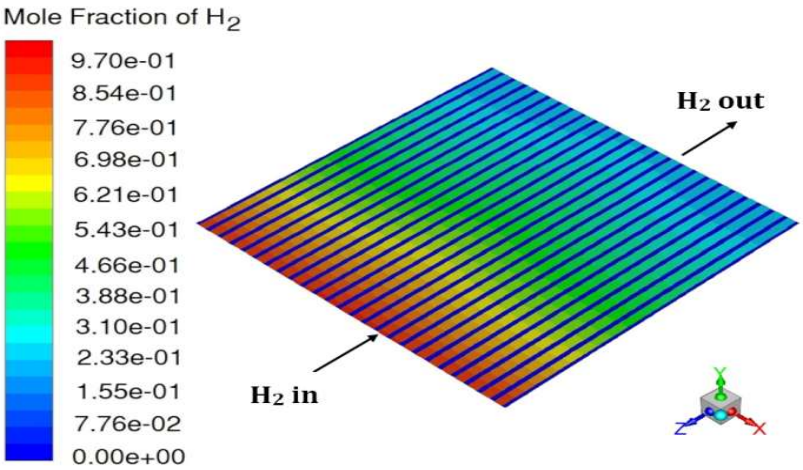

FIGURE 4. 9: Hydrogen mole fraction distribution along the cell length at peak current density.

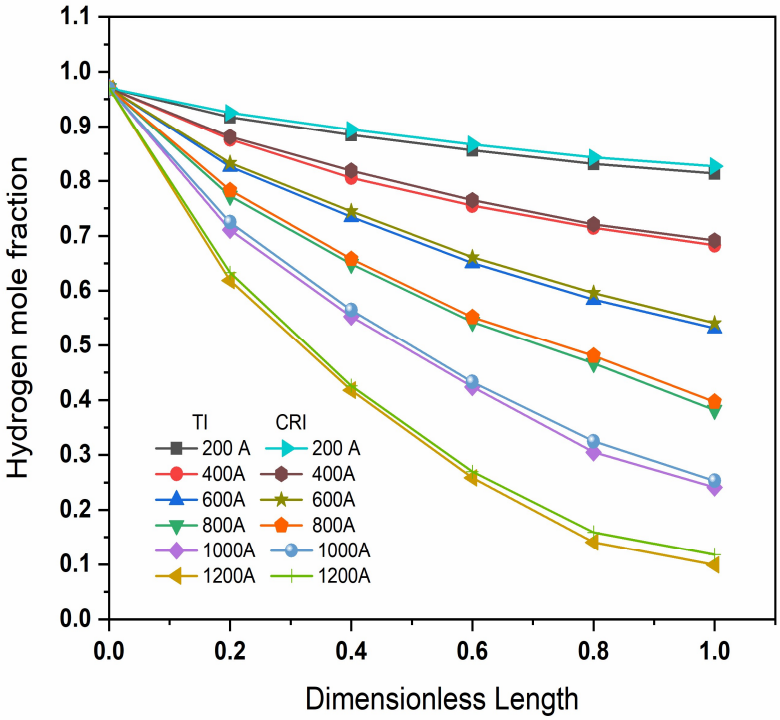

FIGURE 4. 10: Comparison of hydrogen mole fraction consumption for TI and CRI design

From the comparison plots of oxygen mole fraction and hydrogen mole fraction along the non-dimensional channel length for TI and CRI design shown in Figure 4.8 and Figure 4.10 respectively, it is noticed that the oxygen consumption improved significantly compared to hydrogen consumption with TI configuration. Moreover, for the CRI design, it is observed that the cathode electrode has very low oxygen content, especially beneath the ribs and even at the cathode inlet. This shows that the decreased cell function is mostly due to the decreased oxygen transfer caused by increased rib width in CRI design. However, by reducing the rib width, a significantly greater performance is obtained as a result of the reduced ohmic polarization and improved reactant distribution.

4.3.2.3 Pressure distribution

For the two interconnector configurations, Figure 4.11 depicts the distribution of fuel pressure at the anode side of the electrolyte and air pressure at the cathode side of the electrolyte. The pressure drop in the anodic and cathodic flow channels with fixed mass flow rates of fuel and air, respectively, increased with an increase in current density. This was owing to greater operating temperatures and the resultant increased expansion of the fuel/air during operation at higher current densities, resulting in higher fluid velocities and increased friction losses inside the flow channels[70]. The trapezoidal interconnector has a lower fuel and air pressure drop than the conventional rectangular interconnector, as evident from Figure 4.11. This is due to the ease in gas transport achieved by the trapezoidal interconnector design. From the output power viewpoint, at 1000 mA/cm^2 the trapezoidal interconnector produces 2185 mW more power than the conventional rectangular interconnector.

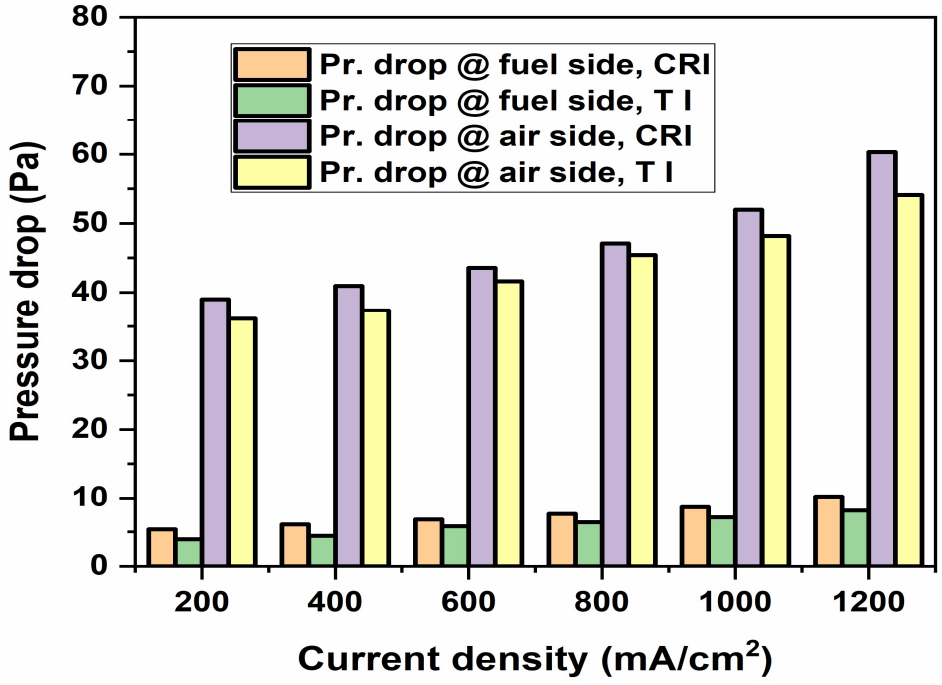

FIGURE 4. 11: Pressure drop at anode and cathode for the conventional rectangular interconnector and trapezoidal interconnector design.

4.3.2.4 Temperature distribution

The temperature distribution at the cathode/electrolyte interface is shown in Figure 4.12. As can be seen, the temperature rises progressively from the entrance to the flow direction. The reason for this trend is that electrochemical reactions generate a significant quantity of heat, as well as ohmic and activation polarization[169]. With increasing current density, the difference in average cell temperature at the cathode/electrolyte interface between TI and CRI increases. This means that the trapezoidal channel design manages heat better than the conventional rectangular interconnector.

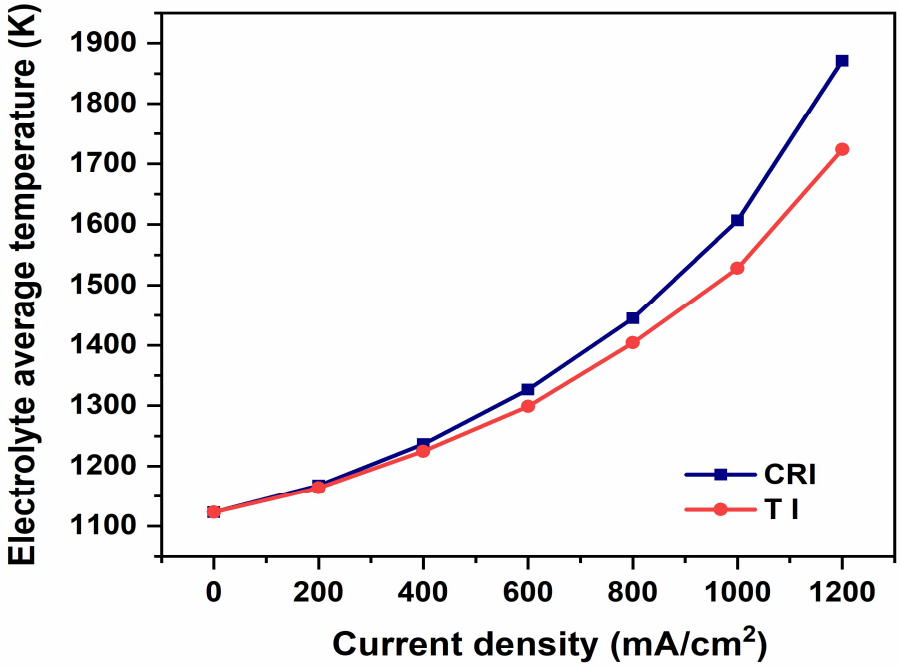

FIGURE 4. 12: Comparison of electrolyte average temperature distribution for the conventional rectangular interconnector and trapezoidal interconnector design.

One of the most critical aspects influencing electrochemical reactions and transport phenomena inside a cell is temperature distribution. To thoroughly understand the effect of different operating temperatures on the electrochemical reactions and cell performance for a trapezoidal interconnector design, a simulation with different operating temperatures of 973K, 1023K, 1073 K, and 1123K was conducted. As expected it is noticed that with an increase in operating

temperature the cell performance increased due to a higher reaction rate favourable at higher temperatures as depicted in Figure 4.12. From the performance plot depicted in Figure 4.13, it is observed that with an increase in operating temperature, the electrolyte average temperature also increased for increasing current density, resulting in changes in operating temperature and voltage, and therefore changing efficiencies[200]. Table 4.4 shows the peak power density obtained for different operating temperatures and their corresponding electrolyte average temperatures. The deviations calculated for the peak power density and their corresponding electrolyte average temperatures suggest that if the performance aspect can be compromised moderately then it is beneficial to operate the cell at 1073K where the electrolyte average temperatures can be cut down by 4.31% compared to operating at 1123K. Operating the cell at 1073K in TI design still offers improvement in performance by a margin of 10.68% compared to the CRI design.

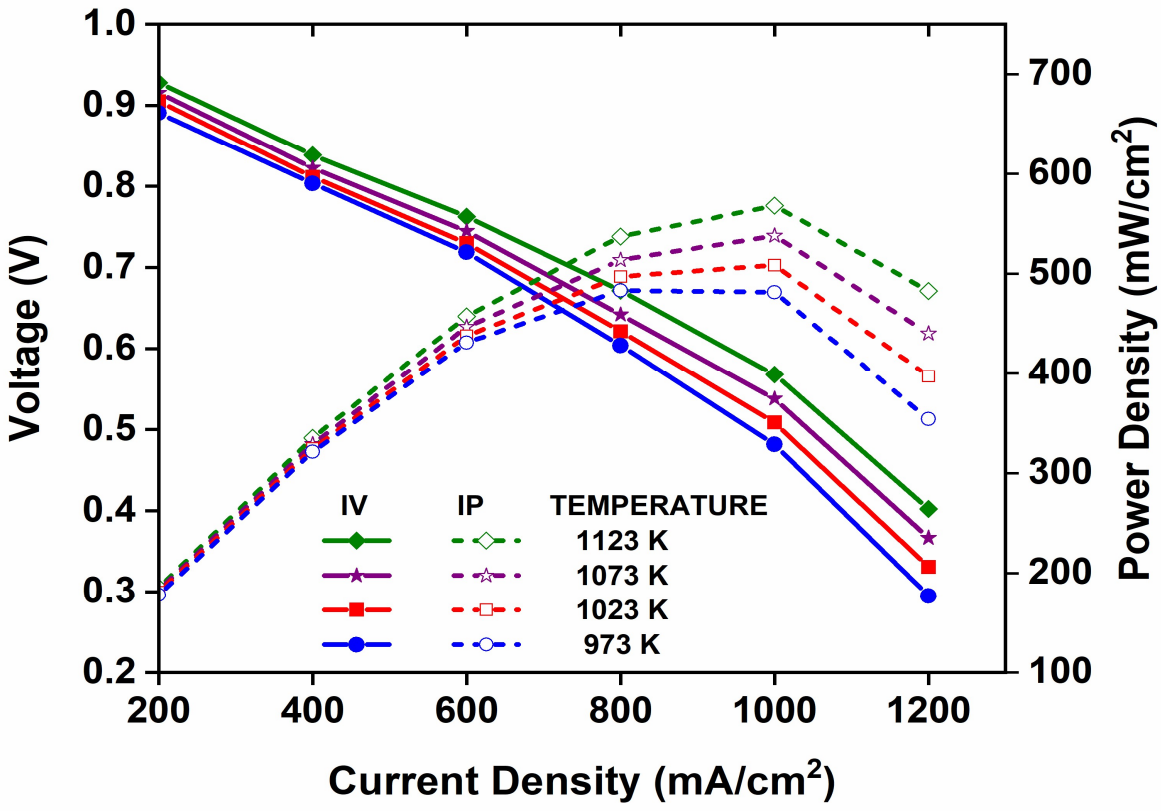

FIGURE 4. 13: I-V and I-P plots for the trapezoidal interconnector simulated at different operating temperatures.

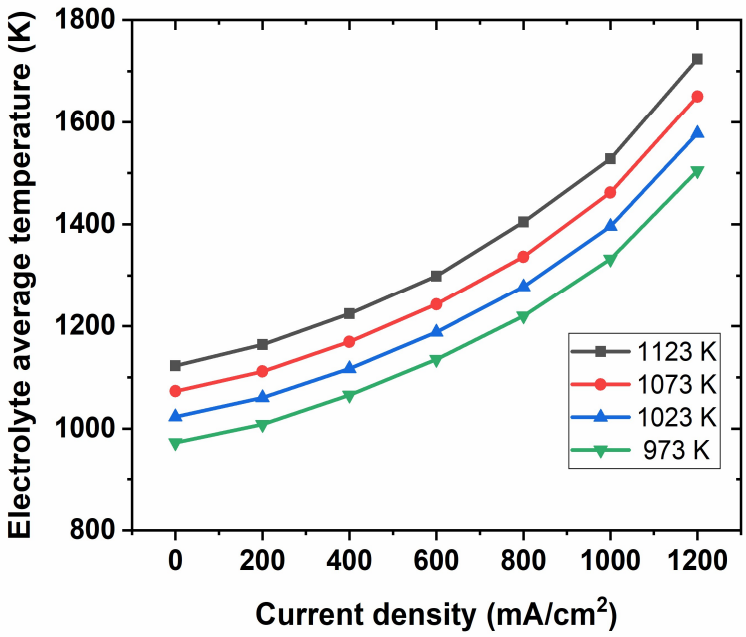

FIGURE 4. 14: Electrolyte average temperature for the trapezoidal interconnector simulated at different operating temperatures.

TABLE 4.2: For different operating temperatures, deviations in peak power density and their corresponding electrolyte average temperature

Operating temperature (K)	Peak power density obtained (mW/cm^2)	Electrolyte average temperature at Peak power density (K)	Deviation in Peak power density (%)	Deviation in Electrolyte Average temperature at Peak power density (%)
1123 (reference)	567.8	1527.97	0	0
1073	537.8	1462.07	5.27	4.31
1023	508.6	1396.08	10.42	8.58
973	481.6	1331.84	15.18	12.8

4.3.3 Performance analysis and comparison of SOFC with TI design against new RATC design

The rib width of the anode side has no substantial effect on fuel transport in an anode-supported SOFC, according to the literature[195]. To justify and understand the influence of rib width on the anode side fuel transport, a SOFC with a Rectangular parallel Anode interconnector and a Trapezoidal Cathode interconnector (RATC) was developed as shown in Figure 4.15. From the performance plot shown in Figure 4.16, it is evident that the cell performance of the new design (RATC) shows marginal variation with the trapezoidal channel interconnector cell. At 1000 mA/cm^2 the decrement of cell power density is estimated to be 2.06%. Therefore it can be established that the influence of rib width has a moderate impact on the anode side fuel transport.

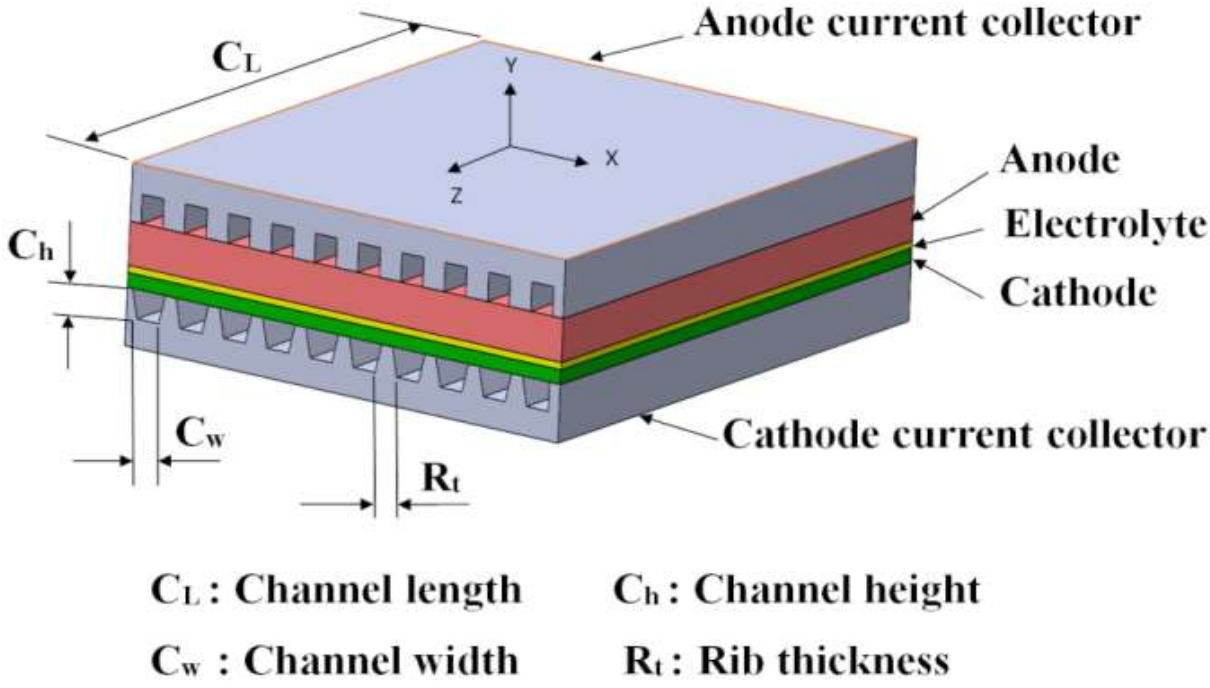

FIGURE 4. 15: SOFC with rectangular parallel anode interconnector and a trapezoidal channel cathode interconnector (RATC).

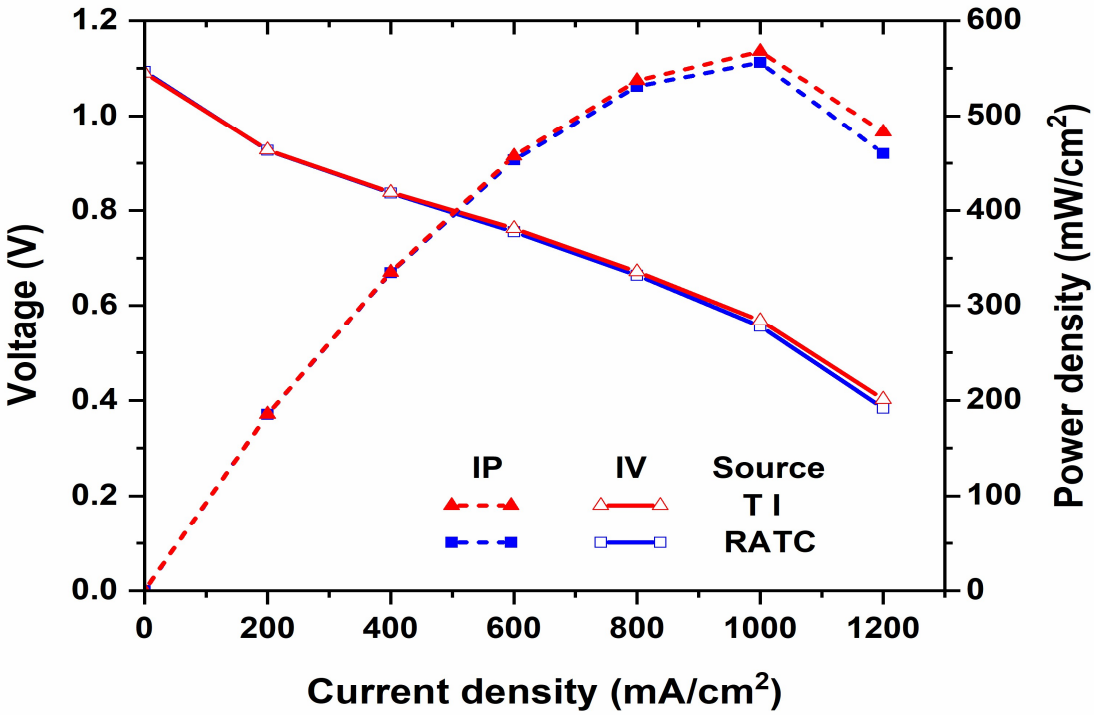

FIGURE 4. 16: Comparison of I-V curve and I-P curve for the Trapezoidal interconnector design against a new design (RATC).

Although machining an interconnector of this scale seems difficult, flow channels can be formed on sheet metals using a variety of processes, including hydroforming, which has been shown to increase the formability of sheet materials when compared to traditional forming methods. Hydroforming also enables the fabrication of intricate concave structures that would be difficult or even impossible to produce using traditional machining methods. Furthermore, this technology is currently being used to manufacture fuel cell interconnectors[201]–[204].

4.4 Summary

In the present study, a SOFC with a trapezoidal interconnector configuration is proposed. The performance analysis of trapezoidal interconnector configuration is compared against the conventional rectangular interconnector considering all the multi-physics involved. A study was

also conducted to determine the impact of rib area on anode fuel transportation. The highlights of the present study are summarized as follows:

1. The present study on anode-supported SOFC indicates that the trapezoidal interconnector design is beneficial for fuel and, in particular, air transportation.
2. The trapezoidal interconnector design improves cell performance. When the cell is operated at 1123K, an increment of 18.2% power density was observed compared to SOFC with a conventional rectangular interconnector configuration.
3. The trapezoidal interconnector offers the advantage of operating the cell at a lower operating temperature of 1073K with an increment of 10.68% power density compared to the 1123K operating temperature in a conventional rectangular interconnector configuration.
4. Considering the large anode conductivity, the area under the rib on the anode side shows moderate changes whether we employ a trapezoidal interconnector or RATC configuration. But from the interchangeability of components and fabrication viewpoint, the trapezoidal interconnector design for both anode and cathode interconnectors is preferable.

CHAPTER 5

Numerical investigation of a novel rhombohedral interconnector configuration for planar solid oxide fuel cells

The numerical outcomes of a planar anode-supported rhombohedral SOFC placed in a staggered pattern are reported in this chapter. At various cell locations, the temperature and species distributions are anticipated. In-depth research is done on the mechanics of heat production and consumption in electrochemical and chemical reactions.

5.1 Introduction

The planar type anode-supported SOFC is chosen for the present study as it is the most widely used because of its compactness and higher volume power density From the extensive literature survey, it is observed that the various methods adopted by researchers for performance enhancement of fuel cells are: (i) Optimization of flow channel/ interconnector configuration, (ii) Insertion of obstacles of different shapes in the flow path (iii) Alternation of operating parameters. In the present study, a planar type anode supported SOFC with counter flow direction is considered with an aim to design an interconnector that incorporates the feature of baffles in the flow path without designing a separate entity for obstacle creation. Therefore, an interconnector with a hollow rhombohedral channel is designed and it is placed in a staggered position. The reason for making the hollow rhombohedral channel is to prevent the dead zone formation at the back of channels in the flow direction, which is seen in the case of X-type patterns and results in a higher pressure drop.

The current study's specific objective is to evaluate the advantages of the rhombohedral interconnector for the SOFC stacks in terms of channel geometries. The rhombohedral interconnector is placed in a staggered position so that the staggered orientation itself acts as an obstacle, altering the heat and mass transport behaviors and providing a consistent distribution of

reactants at the active surface area of the cell. Besides considering the effects of novel channel geometries, this research also explores the effects of operating parameters, such as stoichiometric and rich stoichiometric fuel and oxidant mass flow rates, on the cell performance.

5.2 Numerical simulation execution

5.2.1 Model Geometry

A 3D planar type anode supported SOFC model consisting of a Conventional Rectangular Interconnector (CRI) with an active area of 50x50 mm^2 was validated in our previous study[205]. In the present study of Staggered Rhombohedral Interconnector (SRhI) as the boundary conditions are periodic, the simulation model is simplified such that in the transverse direction to the gas flow channel, three-unit structures of the staggered interconnector accounting for an active area of 18 x50 mm^2 were employed as shown in Figure 5.1. To validate the SRhI concept with a reduced active area, first a rectangle parallel interconnector is modeled with the same dimensions as that of the references[189],[190] which are tabulated in Table 5.1, but with a reduced active area of 18x50 mm^2 as shown in Figure 5.2. Since it was proposed to switch the interconnector arrangement from CRI to SRhI, the active electrolyte surface area was fixed at 18x50 mm^2 for comparison while retaining the flow volume for SRhI at the same rate as that of CRI. The counterflow direction for fuel and air is selected for the validation study as well as in the present study considering the advantage of counterflow over the co-flow[180].

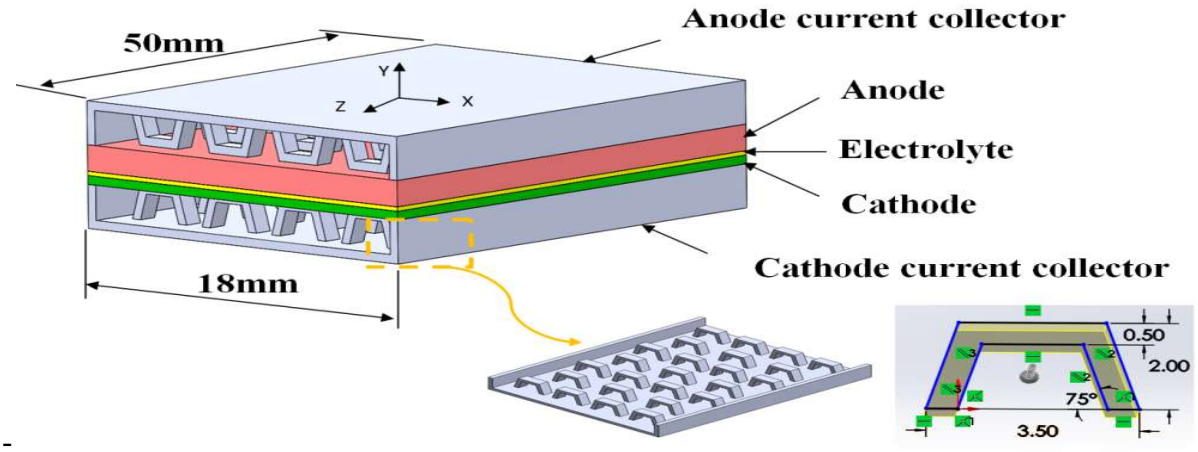

FIGURE 5. 1: SOFC model with staggered rhombohedral interconnector

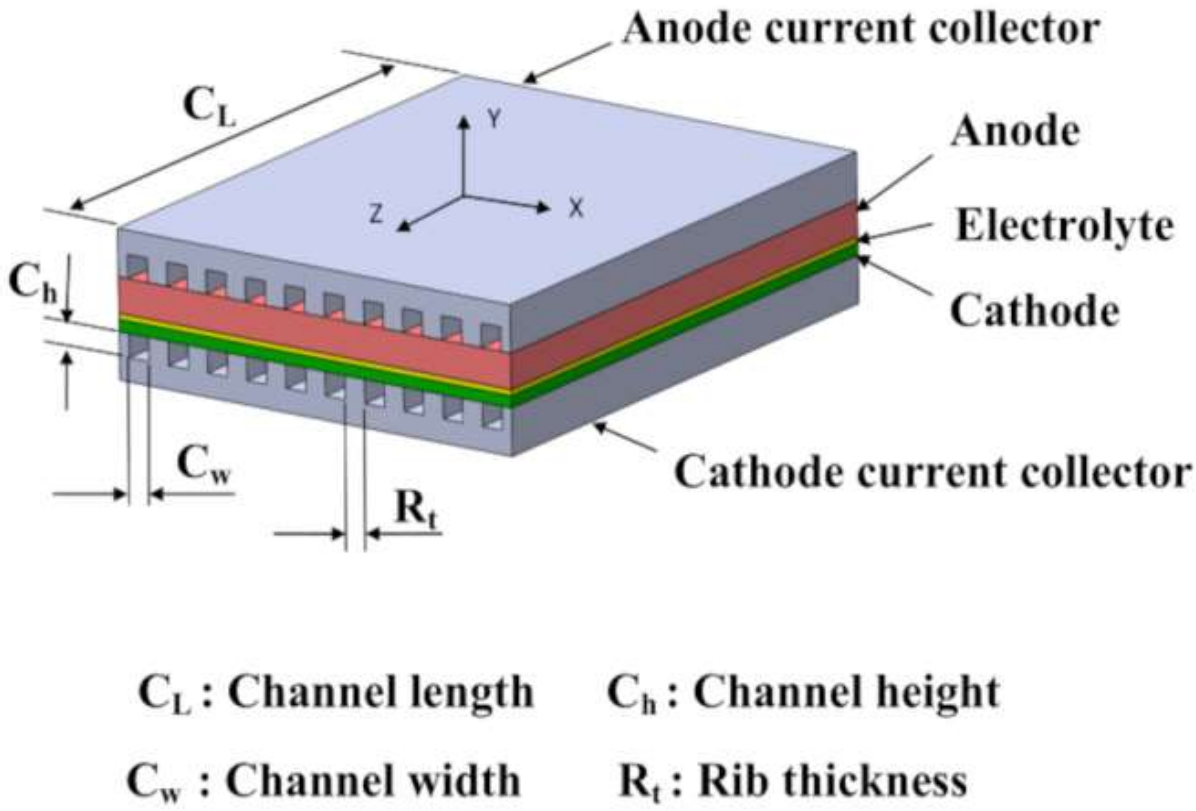

FIGURE 5. 2: SOFC model with conventional rectangular interconnector

TABLE 5.1: Dimensions of SOFC cell for validation study (S.S Wei et al.[190] ; Sembler and Kumar[189]):

Factors	**Magnitude**	**Units**
Height of channel (C_h)	1	mm
Width of channel (C_w)	1	mm
Length of channel (C_L)	50	mm
Interconnector Total height	2	mm
Thickness of each Rib (R_t)	1	mm
Thickness of anode	1.8	mm
Thickness of cathode	30	µm
Thickness of electrolyte (virtual)	20	µm

5.2.2 Numerical solution methodology

ANSYS FLUENT solves the continuity, momentum, energy, and species equations using the Finite Volume Method (FVM) and provides data of flow properties. The SOFC model then uses the local current data, applies species fluxes to the electrode interfaces, and applies the jump condition at the anode and cathode interface to calculate the electric field potential. The electric field potential consists of ohmic losses due to conducting materials, contact resistance, and the distribution of current density in the entire domain. The following solver settings were adopted to solve the governing equations:

- In the fluent launcher, double precision with a steady state, pressure-based and absolute velocity formulations are chosen.
- To solve the partial differential equations, a coupled scheme for pressure-velocity coupling is chosen.
- It was decided to use the second-order UPWIND technique for the spatial discretization of governing parameters.
- Due to the fact that it involves multi-physics, the residuals' convergence requirement for each parameter is set at 1e-08.
- For the solution to converge, it is critical to set up proper solution control parameters. The solver is quite sensitive to species equations, thus using the software's default parameters isn't enough. As a result, for each variable, appropriate under-relaxation factors should be determined.

Furthermore, adjusting multi-grid settings is strongly advised. To create a stable solution, “BCGSTAB” should be utilized as the stabilization approach if the solution exhibits fluctuating behavior.

5.3. Results and Discussion

To make the SOFC simulation environment easier to use, a unit cell was divided into anode, anode-interconnector, cathode and cathode-interconnector to assess the performance of the novel staggered rhombohedral interconnector. This work uses nickel cermet (Ni + YSZ) as the anode,

strontium doped with lanthanum manganite (LSM) as the cathode, and yttria-stabilized zirconia (YSZ) as the electrolyte.

5.3.1 Meshing and Grid independence study

ANSYS software is used to mesh the CRI computational domain. Based on the grid independence analysis performed by Sembler and Kumar[70], the whole computational domain was split into discrete components. For the computational domain discretization, a global mesh of 0.5 mm size is utilized, followed by local edge scaling along the cell's thickness direction. A thorough grid convergence test for the staggered rhombohedral interconnector was carried out utilizing the following elements: 429766, 590584, and 720164. Figure 5.3 shows that the polarization curve achieved with 590584 elements was almost equal to that obtained with 720164 elements. Therefore, 590584 elements were used in subsequent simulations.

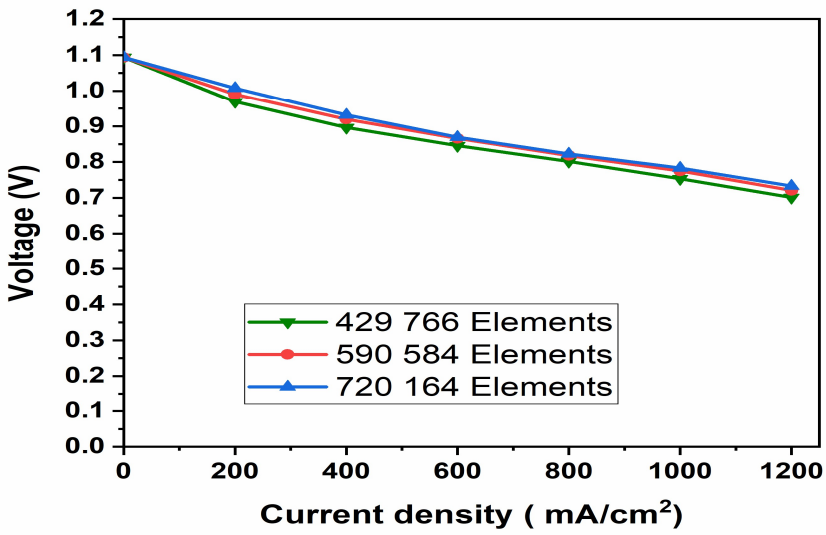

FIGURE 5. 3: Grid Independence study

5.3.2 Performance evaluation of SOFCs with SRhI design against CRI Design

The ploarization curves for SRhI and CRI configurations are shown in Figure 5.4. To compare the performance of the CRI design against the SRhI design whose active area is 18 X 50 mm^2, the CRI model used for validation was rebuilt with an active area of 18 X 50 mm^2 and the mass flow rate is calculated for the reduced active area maintaining the same stoichiometric ratios of

1.2 for fuel and 1.7 for air as that of references to thoroughly understand the impact of fluid flow and the electro-chemical behavior of both interconnector designs.

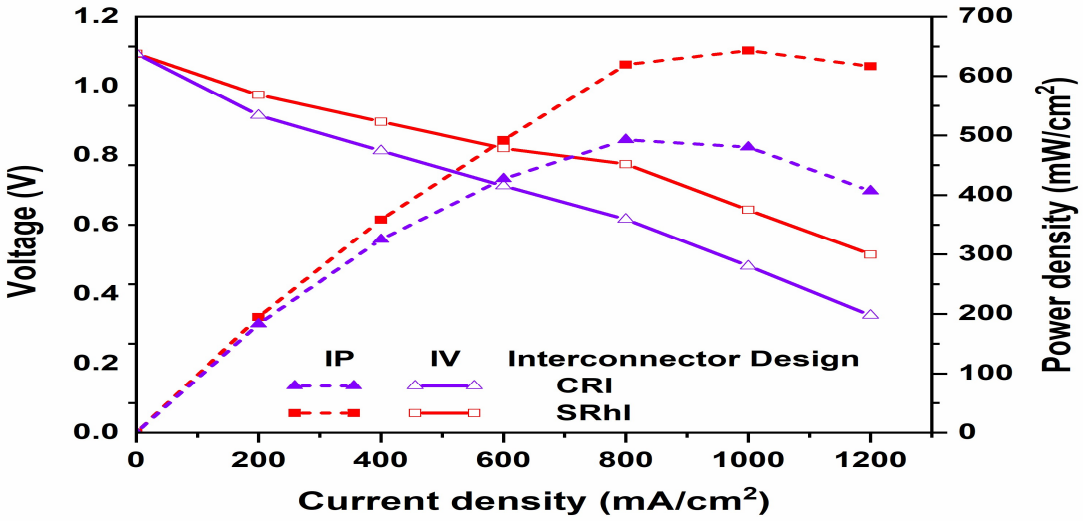

FIGURE 5. 4: Polarization curve for CRI and SRhI designs

At a current density of 1000 $mAcm^{-2}$, the SRhI has a peak power density of 643.2 mW/cm^2 against 480.4 mW/cm^2 for the CRI configuration. Therefore, an increase of 33.9% power density is obtained with the novel flow channel configuration. The reasons for the improvement in performance obtained by adopting the SRhI configuration are discussed by comparing the differences between both the designs with respect to various parameters in the subsection that follows.

5.3.2.1 Oxygen Mole Fraction Distribution

The oxygen content under the rib is reported to be extremely important for anode-supported planar type SOFCs in the literature [194], [195]. As a result, improving the oxygen content beneath the ribs is advantageous for improving cell performance. The oxygen mole fraction distribution for both CRI and SRhI are shown in Figures 5.5(a) and 5.5(b) respectively. It is observed that although the decrement of mole fraction at the outlet of the cell for both the interconnector design is nearly the same about 0.158, the area under the rib for the SRhI design has shown a significant improvement as evident from figure 5.5(b). The decrease of the average oxygen mole fraction from 0.14 under the rib vicinity of the inlet region to 0.04 under the outlet

section of the rib vicinity along the channel for SRhI indicates better dispersion of the oxidant and leads to a reduction in pressure drop in the cathode section of the cell.

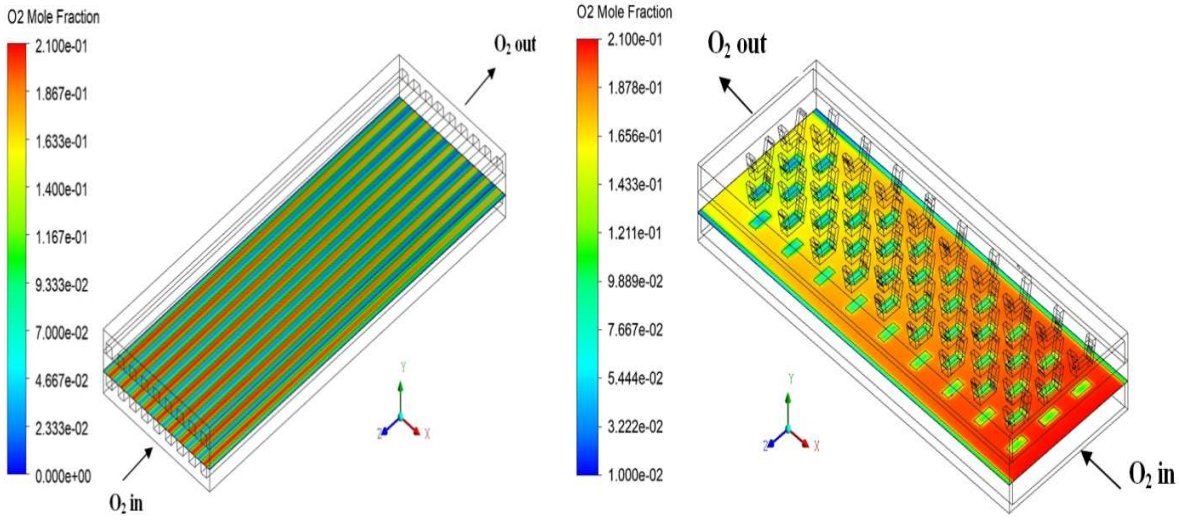

5.5(a) 5.5(b)

FIGURE 5. 5: Oxygen mole fraction distribution (a) CRI (b) SRhI

5.3.2.2 Pressure distribution

For both CRI and SRhI configurations, Figure 5.6 and Figure 5.7 depict fuel pressure distribution at the anode side of the cell and air pressure distribution at the cathode side of the cell respectively. From the pressure distribution plots of fuel shown in Figures 6(a) and 6(b) for CRI and SRhI designs respectively, it is noticed that the average pressure drop in SRhI is nearly the same to CRI design with a marginal decrement in average pressure drop from 4655.5 Pa in CRI against 4625.54 Pa in SRhI design. As the thickness of the anode is more in anode supported cells, the area under the rib is not much affected like in the cathode side. Therefore, the pressure drops for both the interconnectors design is more or less the same. On the other hand, the pressure distribution plots of air shown in Figure 5.7(a) and 5.7(b) for CRI and SRhI design respectively, shows that SRhI offers lesser pressure drop than the CRI configuration. The reason for such a drastic improvement in pressure drop in the cathode side of the cell can be attributed to the uniform gas distribution offered by the rhombohedral design placed in a staggered position causing minimum hindrance to the gas flow and acting as a direction control agent to disperse

the gas uniformly throughout the active area of the cell. Compared to CRI design, the pressure drop in the air has been reduced by 94.9% for SRhI design which indicates that SRhI configuration is superior to CRI configuration.

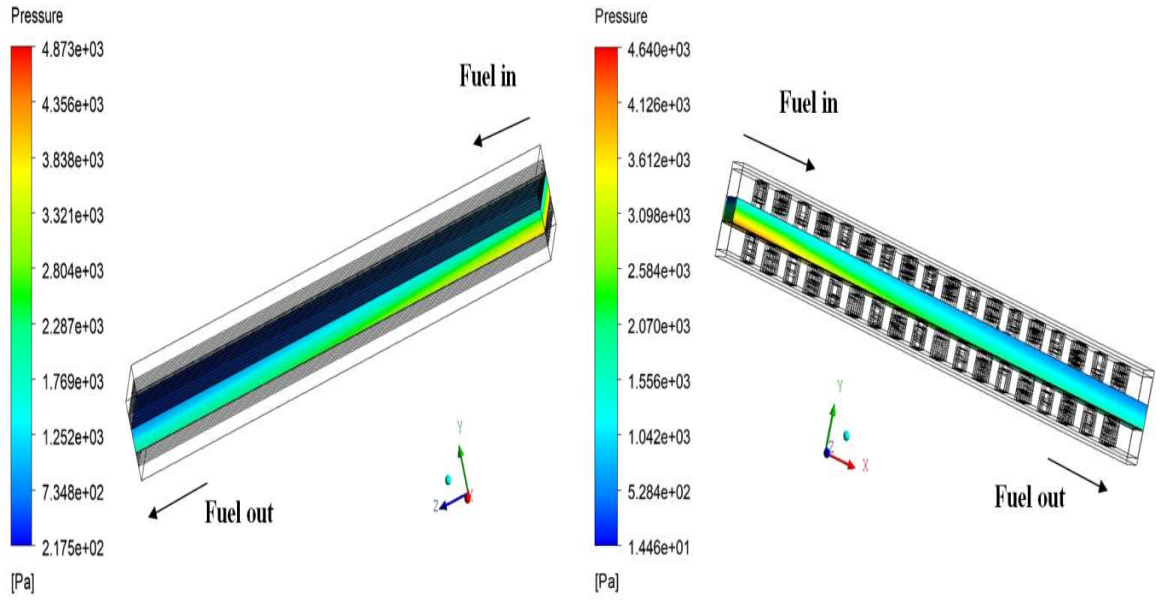

5.6(a) 5.6(b)

FIGURE 5. 6: Pressure distribution of fuel (a) CRI (b) SRhI

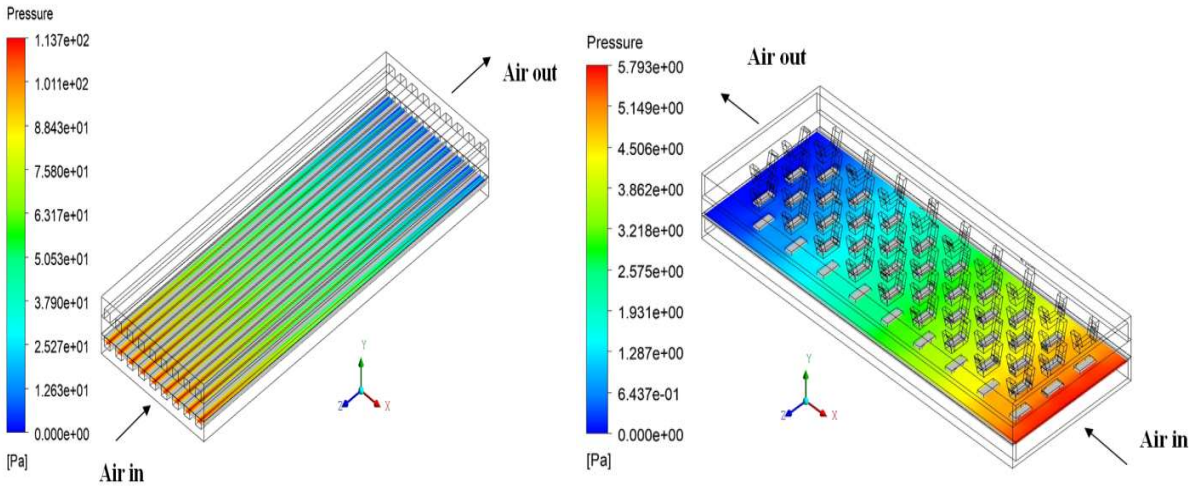

5.7(a) 5.7(b)

FIGURE 5. 7: Pressure distribution of air (a) CRI (b) SRhI

5.3.2.3 Electrical potential distribution

The electrical potential for both CRI and SRhI configurations is depicted in Figures 5.8(a) and 5.8(b) respectively. Because the rib collects the current emanating from the anode, it is apparent that the electrical potential just beneath the cathode where the collector is in contact is superior to that where the current is tapped[176]. It is obvious that for a specified current density of 1000 mA/cm^2, the SRhI interconnector design is better than the CRI design as the voltage acquired at the cathode tapping of CRI is recorded as 0.7465 V compared to 0.7746 V for SRhI. It is observed that the potential generated at the electrolyte reaction site gets reduced till it reaches the cathode tapping due to ohmic polarization losses and in the case of CRI design the potential reduces from 0.7609V to 0.7465V. Similarly, for SRhI design, the potential reduces from 0.7841 V to 0.7746 V. The potential difference in CRI accounts for 0.0144V against 0.0095V for the SRhI design which shows that the SRhI configuration is 34.03% more efficient as the current collector than the CRI configuration. Therefore, it can be agreed that the SRhI design provides a shorter current path and aids in the improvement of SOFC performance.

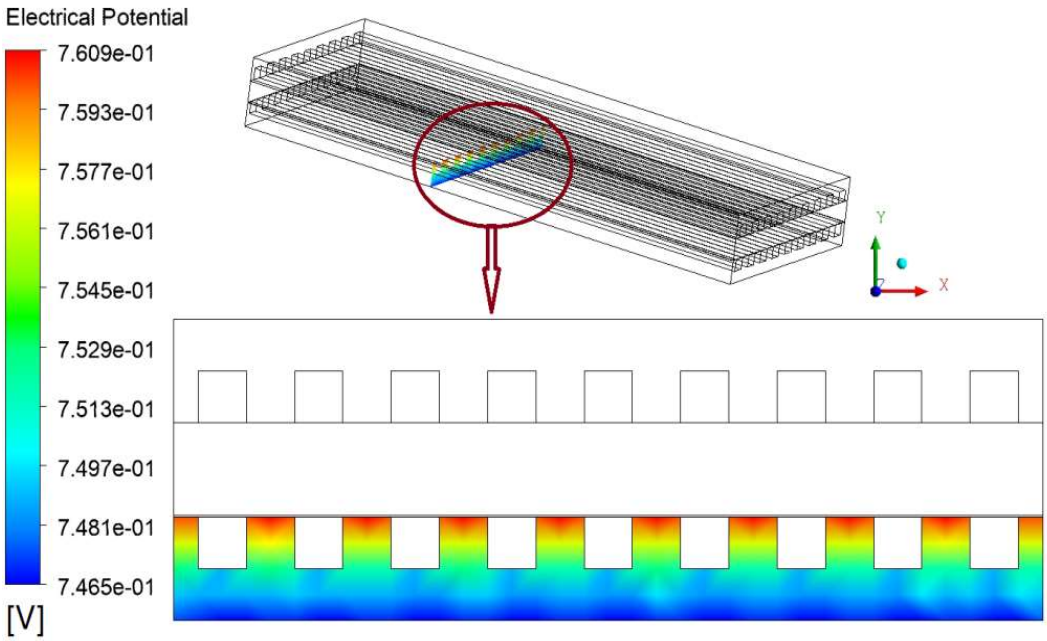

5.8(a)

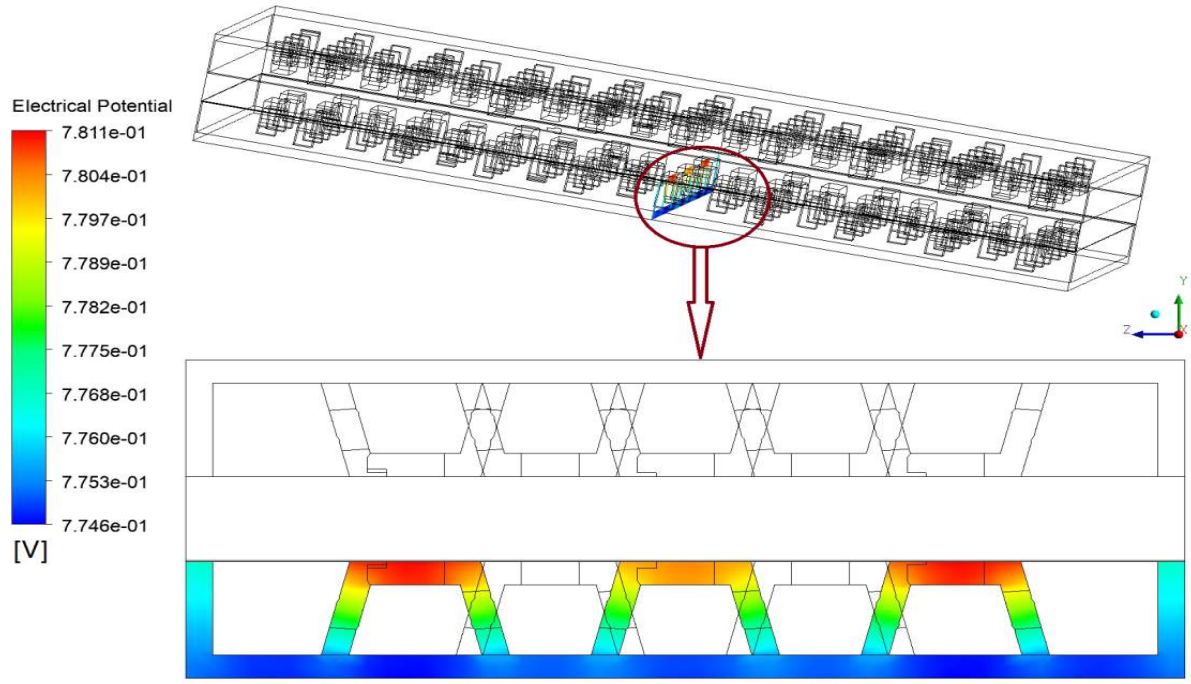

5.8(b)

FIGURE 5. 8: Electrical potential distribution (a) CRI (b) SRhI

5.3.2.4 Temperature distribution

Temperature distribution is one of the most significant parameters affecting the electrochemical processes and transfer phenomena inside a cell. As the electrolyte is the core reaction site where the electrochemical reaction takes place and generates a huge amount of heat, the temperature distribution at electrolyte for both CRI and SRhI design is depicted in Figures 5.9(a) and 5.9(b) respectively.

As it can be visualized from the plots, the maximum temperature for both the interconnector designs is observed to be almost at the midway of the cell length indicating temperature change was impacted by the interaction of the heat of reaction and the transferred heat. For the CRI design, the minimum temperature observed is 1207 K at the fuel inlet section with a maximum temperature of 1245 K being near the middle of the cell and 1239 K at the air inlet section. From this temperature trend, it can be inferred that the temperature distribution in the CRI design is non-uniform and the temperature difference along the length of the cell for CRI is 38 K.

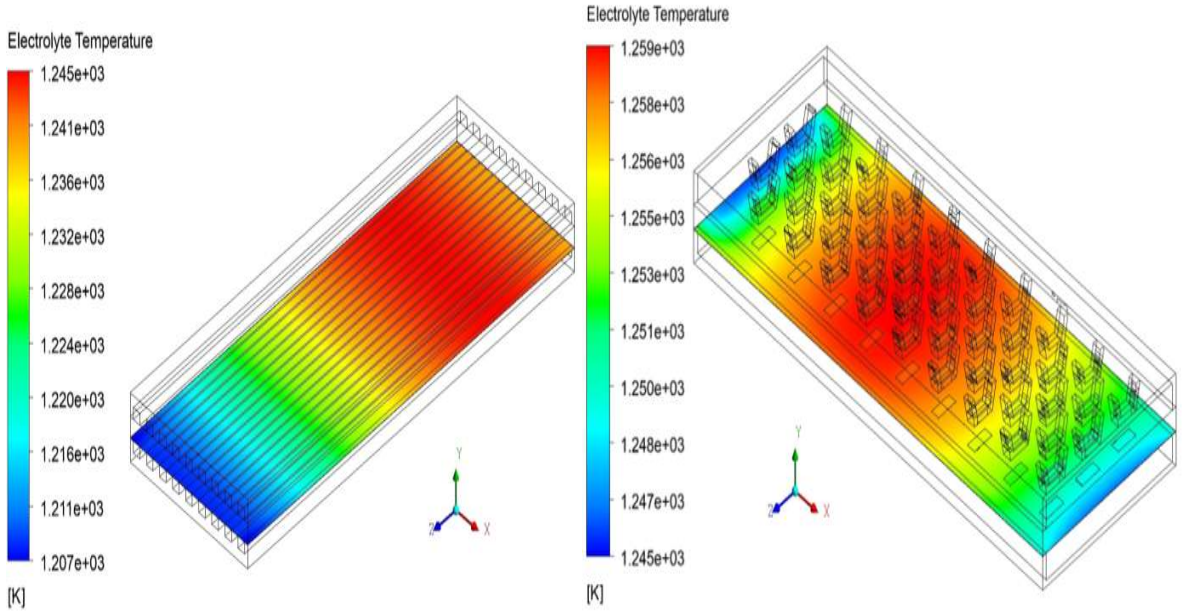

5.9(a) 5. 9(b)

FIGURE 5. 9: Temperature distribution at electrolyte (a) CRI (b) SRhI

On the other hand, the SRhI design offers uniform temperature distribution with a maximum temperature of 1259 K being at the middle of the cell length and 1247 K and 1245 K at the fuel inlet and air inlet respectively. The temperature difference along the length of the cell for SRhI is only 14 K signifying better heat management than the CRI design. The reason for better heat management can be attributed to the reduction in pressure drop and better diffusion of oxygen under the rib area of the cathode section obtained in the SRhI design of the interconnector. Moreover, the higher maximum temperature of 1259 K obtained in SRhI against the maximum temperature of 1245K in CRI is also an indication of improved electro-chemical reaction and thereby the overall improvement of the cell performance.

The whole cell temperature distribution plots for CRI and SRhI configurations are depicted in Figures 5.10(a) and 5.10(b), respectively, to understand and visualize the temperature distribution in the entire cell domain. From the plots, it is clear that the SRhI arrangement helps achieve uniform temperature distribution.

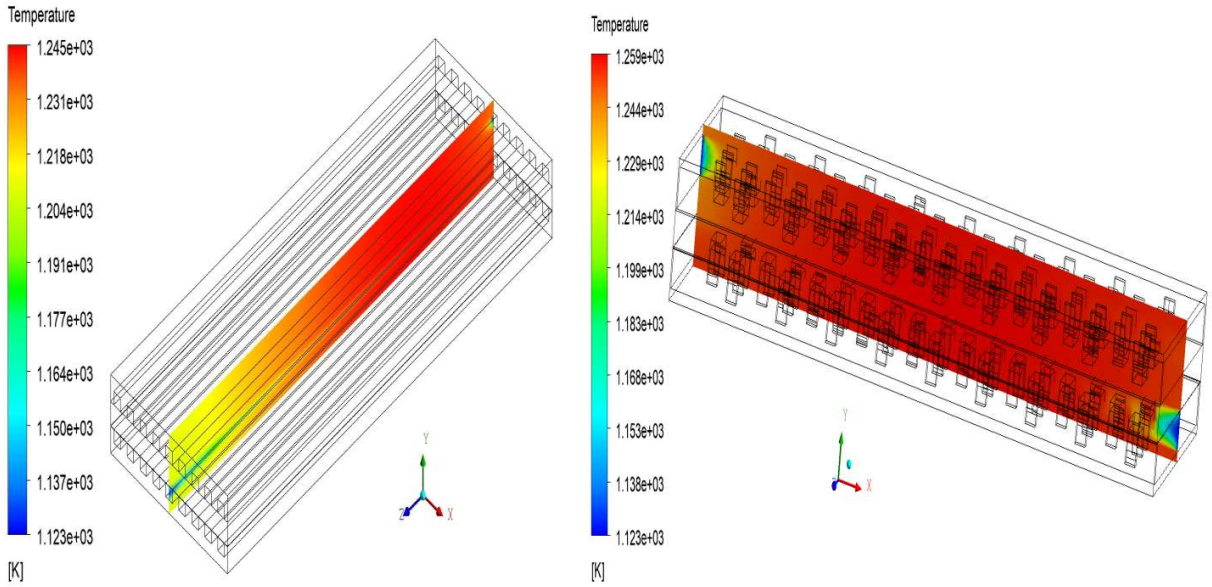

5.10(a) 5.10(b)

FIGURE 5. 10: Whole cell temperature distribution (a) CRI (b) SRhI

5.3.3 Effect of different mass flow rates

An analysis is undertaken to understand how different mass flow rates affect the SOFC performance with SRhI interconnectors. Considering the standard mass flow rate used in the comparison study as the base case (i.e ξ =1.2 for fuel and ξ=1.7 for air), the mass flow rate is varied at the lower end as the exact stoichiometric mass flow rate for fuel and air (i.e. ξ =1 for fuel and ξ=1for air) and rich stoichiometric mass flow rate as ξ =1.7 for fuel and ξ=2 for air on the higher end. Figure 5.11 shows the variation in performance curves with different mass flow rates for SRhI design.

It can be inferred that for the supplied exact stoichiometric mass flow rate for fuel and air, the performance curve follows the base case performance curve trend closely at lower current density values. But as the current density increases, the V-I curve starts deviating gradually from 400 mA/ cm^2 to the maximum current density of 800 mA/ cm^2 which is achieved with the considered mass flow rate before starvation. The drop in cell performance is due to insufficient

availability of reactants, in particular, the oxidant mole fraction value getting reduced to 0.0942 near the air exit section, and the area under the ribs getting reduced to 0.02476 in the early portion of the air inlet section being the main cause of cell performance limitation as evident from Figure 5.12.

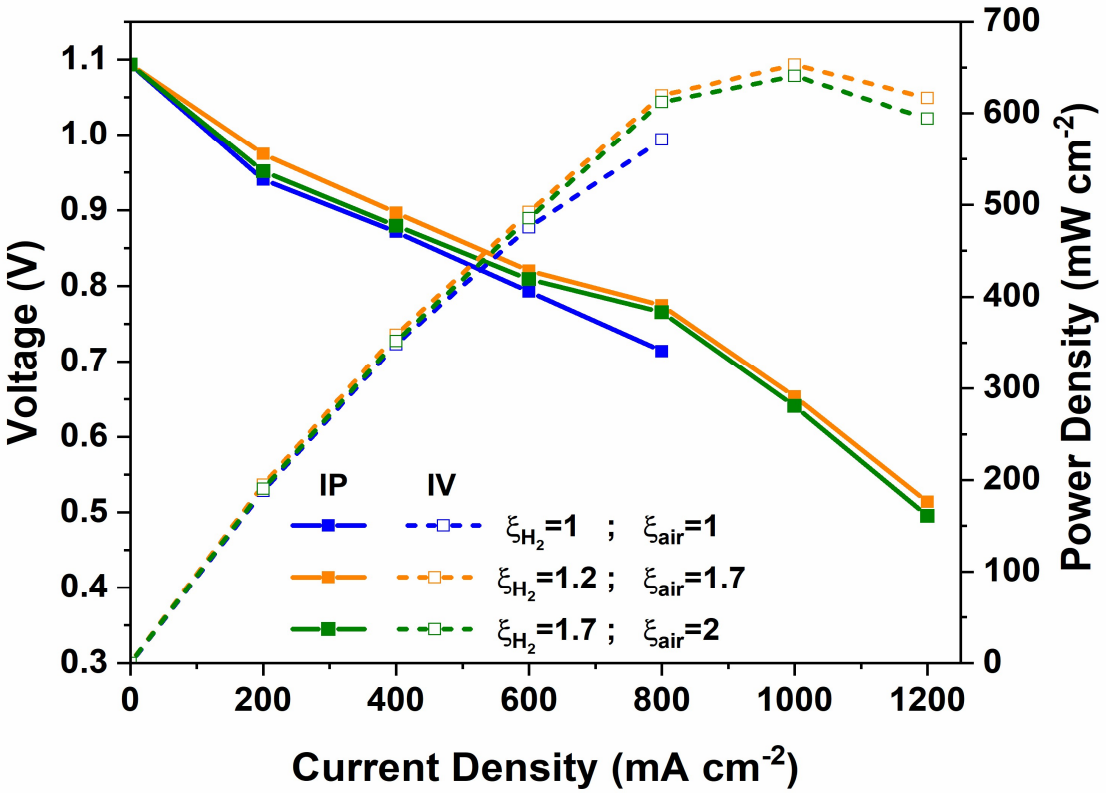

FIGURE 5. 11: Variation in polarization curve with different mass flow rates for SRhI design

On the other hand, when rich stoichiometric mass flow rate are supplied it was observed that the performance of rich stoichiometric mass flow rate is significantly lower than the base case performance curve for lower current density up to 600 mA/ cm^2 and thereafter the differences gradually reduce with an increase in current density up to 1200 mA/ cm^2. The curve shown in Figure 5.13 provides an explanation for the decreased performance in the case of rich stoichiometric mass flow rate. This figure shows that the average cell temperature is lower than the base case average cell temperature over the entire current density range, indicating an excess reactant supply. Since the electrochemical reaction in the cell has accumulated enough reactants

and the oxidant piles up on the cathode side, an apparent performance enhancement is unlikely[199].

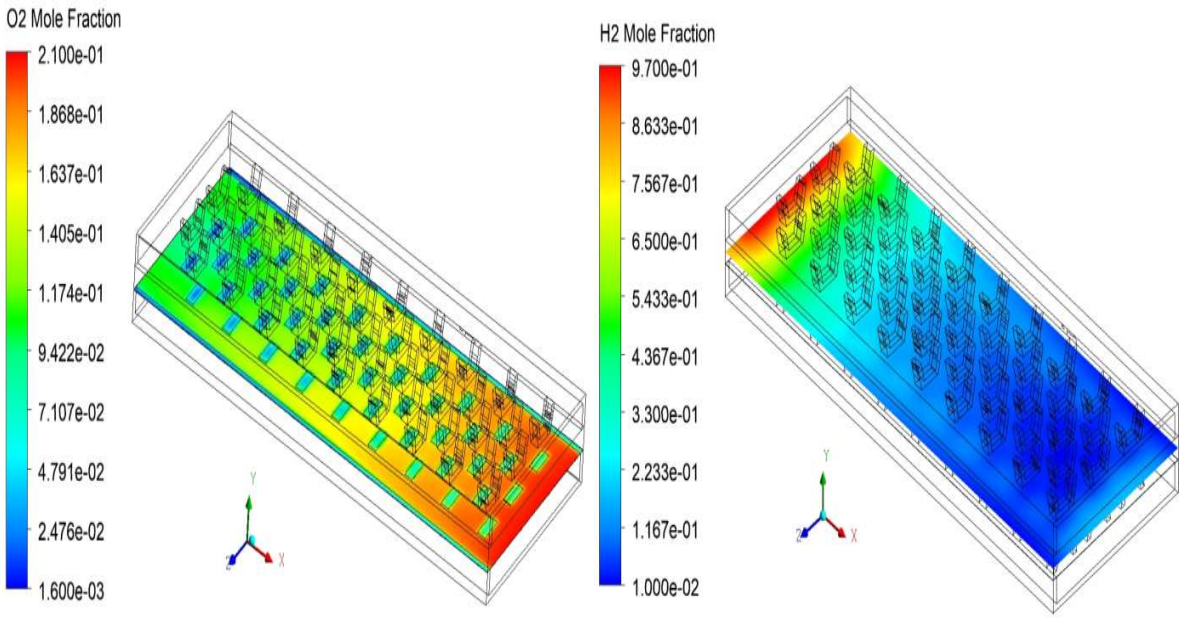

5.12(a) 5.12(b)

FIGURE 5. 12: Distribution of air (a) and Fuel (b) at stoichiometric mass flow rate ratio

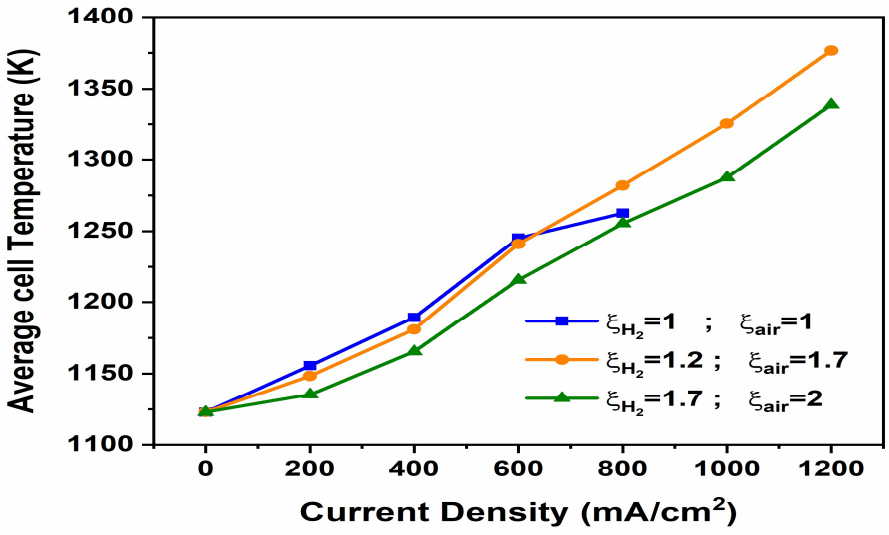

FIGURE 5. 13: Variation in average cell temperature with different mass flow rates for SRhI design

5.3.4 Comparison of SRhI configuration with other previously studied configurations

Table 5.2 provides a brief insight about the performance improvement achieved by using various designs for the interconnectors. The primary objective in varying the interconnector configuration is to address the diffusion of oxygen in the rib section of the thin porous cathode which was reported to be a limiting criterion in planar SOFC. The parameters shown in table 5 are pertaining to a current density where maximum power density is achieved for all the three configurations. It is evident from the power density values that the SRhI configuration is better than the Trapezoidal interconnector. The TI configuration is better than the CRI. The primary reason for this trend can be justified with the pressure drop values at the cathode side of the cell. When compared to TI and CRI, SRhI achieved a smaller pressure drop, indicating better oxygen diffusion at the rib area.

TABLE 5.2 : Comparison of SRhI configuration with other previously studied configurations

Configurations→/ parameters↓	Conventional Rectangular Interconnector (CRI)	Trapezoidal Interconnector (TI)	Staggered Rhombohedral Interconnector (SRhI)
Power Density (mW/ cm^2)	480.4	567.8	643.2
Pressure drop at cathode side of cell(Pa)	113.70	50.24	5.793

5.4 Summary

The SOFC with a rhombohedral interconnector positioned in a staggered position is proposed in the current work and is referred to as SRhI. When comparing the performance study of the SRhI configuration to that of the conventional rectangular interconnector (CRI), all the relevant multi-

physics are taken into account. The impact of different mass flow rates on cell performance was also investigated. The results of the present studies indicate that the performance of SRhI is superior to CRI as it offers the following advantages:

- Better oxygen distribution beneath the ribs
- Shorter current path
- Reduced pressure drop, and
- Uniform temperature distribution along the length of the cell.

The above advantages pertaining to SRhI lead to an increase in cell performance by 33.9% compared to the CRI design. The fuel and oxidant in the anode and cathode respectively will be depleted before it reaches the cell exit when the inlet flow rates are less than a particular threshold, the oxidant flow rate being dominant in impacting the cell performance. When the cathode inlet flow rate exceeds the critical value, an increase in cell performance is challenging as the inlet air has already met the electrochemical reaction's needs. Therefore it can be concluded that an increase in fuel/air flows is associated with an increase in cell performance up to a certain range only and the rate of increase in cell performance decreases gradually with increased fuel/air mass flow rates.

CHAPTER 6

Conclusion and Future Scope

The main objective of this thesis is to provide a numerical model for analysing the performance of SOFCs by linking the dynamics of electrochemical reacting fluxes, heat transfer, and thermal effects of solid electrolyte and porous electrodes. Thermal strains and stresses are produced in SOFCs as a result of the high working temperature, which might lead to cell collapse. To enhance the performance of the cell, the areas with greater thermal stresses are identified and addressed by novel geometrical configurations. The main findings of this study are presented below, followed by recommendations for further investigation.

6.1 Conclusion

In the present study, a SOFC with a Trapezoidal interconnector and a rhombohedral interconnector placed in a staggered position abbreviated as SRhI is proposed. The performance analysis of Trapezoidal interconnector (TI) and SRhI configuration is compared against the conventional rectangular interconnector (CRI), considering all the multi-physics involved. A study was also conducted to determine the varying mass flow rate and different operating temperature impact on cell performance. A study was also undertaken to determine the impact of rib area on anode fuel transportation. The highlights of the studies are summarized as follows:

- The study on anode-supported SOFC indicates that the trapezoidal interconnector design is beneficial for fuel and, in particular, air transportation.
- The trapezoidal interconnector design improves the cell performance. When the cell is operated at 1123K, an increment of 18.2% power density was observed compared to SOFC with a conventional rectangular interconnector configuration.
- The trapezoidal interconnector offers the advantage of operating the cell at a lower operating temperature of 1073K with an increment of 10.68% power density compared to the 1123K operating temperature in a conventional rectangular interconnector configuration.

- Considering the large anode conductivity, the area under the rib on the anode side shows moderate changes whether we employ a trapezoidal interconnector or RATC configuration.
- But from the interchangeability of components and fabrication viewpoint, the trapezoidal interconnector design for both anode and cathode interconnector is preferable.
- When comparing the performance study of the SRhI configuration to that of the conventional rectangular interconnector (CRI), the SRhI lead to an increase in cell performance by 33.9% .
- The fuel and oxidant in the anode and cathode respectively will be depleted before it reaches the cell exit when the inlet flow rates are less than a particular threshold, the oxidant flow rate being dominant in impacting the cell performance.
- When the cathode inlet flow rate exceeds the critical value, an increase in cell performance is challenging as the inlet air has already met the electrochemical reaction's needs.
- Therefore it can be concluded that an increase in fuel/air flows is associated with an increase in cell performance up to a certain range only and the rate of increase in cell performance decreases gradually with increased fuel/air mass flow rates.

Out of the three interconnector configurations studied, the SRhI configuration is better than the Trapezoidal interconnector. The TI configuration is better than the CRI.

6.2 Future Scope

The most advanced and fuel-flexible 3D numerical model of SOFC is currently available. The model aids in identifying potential points of failure during cell operation. Additionally, it aids in the selection of appropriate materials for the various cell components that are necessary for improved structural stability and performance. The following directions for the investigations conducted during this research should be the focus of future work.

- Carry out a detailed analysis of the polarization losses and temperature distribution for tapered interconnector configuration for fuel and air.
- Parametric optimization of TI configuration by varying the channel height along with channel and rib width.
- Performance enhancement by using non-hollowed trapezoidal, rectangular, elliptical, and semi-spherical interconnectors placed in a staggered position.

References

[1] A. M. Omer, "Energy, environment and sustainable development," *Renew. Sustain. Energy Rev.*, vol. 12, no. 9, pp. 2265–2300, Dec. 2008, doi: 10.1016/J.RSER.2007.05.001.

[2] U.S. Energy Information Administration (EIA), "International Energy Outlook 2021: Case Descriptions," 2021.

[3] K. Venkata Sundar Rao, S. N. Kurbet, and V. V. Kuppast, "A Review on Performance of the IC Engine Using Alternative Fuels," *Mater. Today Proc.*, vol. 5, no. 1, pp. 1989–1996, Jan. 2018, doi: 10.1016/J.MATPR.2017.11.303.

[4] L. Chen, K. Gao, C. Zhang, and W. Lang, "Alternative fuels for IC engines and jet engines and comparison of their gaseous and particulate matter emissions," *Adv. Biofuels Appl. Technol. Environ. Sustain.*, pp. 17–64, Jan. 2019, doi: 10.1016/B978-0-08-102791-2.00002-7.

[5] A. S. Ramadhas, S. Jayaraj, and C. Muraleedharan, "Use of vegetable oils as I.C. engine fuels - A review," *Renew. Energy*, vol. 29, no. 5, pp. 727–742, 2004, doi: 10.1016/j.renene.2003.09.008.

[6] B. V. Subhanandh, N. Abilash, and P. S. Raveendran, "Investigation of emission and performance analysis of honne oil in VCR diesel engine," *J. Phys. Conf. Ser.*, vol. 2054, no. 1, Oct. 2021, doi: 10.1088/1742-6596/2054/1/012065.

[7] M. Tomar, A. Sonthalia, N. Kumar, and H. Dewal, "Waste glycerol derived bio-propanol as a potential extender fuel for compressed ignition engine," *Environ. Prog. Sustain. Energy*, vol. 40, no. 2, Mar. 2021, doi: 10.1002/EP.13526.

[8] D. Liu and C. Yuan, "A coupling study of ignition position on fuel-air mixing and diffusion of a linear hydrogen engine," *Int. J. Hydrogen Energy*, Nov. 2022, doi: 10.1016/j.ijhydene.2022.08.274.

[9] M. M. Wagh and V. V. Kulkarni, "Modeling and Optimization of Integration of Renewable Energy Resources (RER) for Minimum Energy Cost, Minimum CO2 Emissions and Sustainable Development, in Recent Years: A Review," *Mater. Today Proc.*, vol. 5, no. 1, pp. 11–21, 2018, doi: 10.1016/j.matpr.2017.11.047.

[10] P. C. Mishra, R. B. Ishaq, and F. Khoshnaw, "Mitigation strategy of carbon dioxide emissions through multiple muffler design exchange and gasoline-methanol blend replacement," *J. Clean. Prod.*, vol. 286, Mar. 2021, doi: 10.1016/j.jclepro.2020.125460.

[11] E. Michalena and J. M. Hills, "Renewable energy governance: Complexities and challenges," *Lect. Notes Energy*, vol. 23, 2013, doi: 10.1007/978-1-4471-5595-9.

[12] C. O. Colpan, Y. Nalbant, and M. Ercelik, "Fundamentals of Fuel Cell Technologies," in *Comprehensive Energy Systems*, vol. 4–5, 2018.

[13] A. Hamnett, *Handbook of Fuel Cells Fundamentals, Technology, Application*. 2010.

[14] J. J. Chen, X. H. Gao, L. F. Yan, and D. G. Xu, "Progress and Challenges in the Direct Carbon Fuel Cell Technology," *Int. Lett. Chem. Phys. Astron.*, vol. 49, 2015, doi: 10.18052/www.scipress.com/ilcpa.49.109.

[15] J. Ma, N. A. Choudhury, and Y. Sahai, "A comprehensive review of direct borohydride fuel cells," *Renewable and Sustainable Energy Reviews*, vol. 14, no. 1. 2010, doi: 10.1016/j.rser.2009.08.002.

[16] J. Milewski, K. Świrski, M. Santarelli, and P. Leone, "Advanced methods of solid oxide fuel cell modeling," *Green Energy Technol.*, vol. 40, 2014, doi: 10.1007/978-0-85729-262-9.

[17] Á. Varga, "Introduction to fuel cell technology," in *Fuel Cell Electronics Packaging*, 2007, doi: 10.1007/978-0-387-47324-6_1.

[18] A. L. Dicks and D. A. J. Rand, *Fuel Cell Systems Explained*. 2018.

[19] B. Cook, "Introduction to fuel cells and hydrogen technology," *Eng. Sci. Educ. J.*, vol. 11, no. 6, 2002, doi: 10.1049/esej:20020601.

[20] D. H. Program, "Hydrogen Fuel Cells Fact Sheet," *U.S. Dep. Energy*, 2006.

[21] S. C. Singhal, "Solid Oxide Fuels Cells: Facts and Figures," *Green Energy Technol.*, vol. 55, 2013.

[22] J. T. S. Irvine and P. Connor, "Solid oxide fuels cells: Facts and figures: Past, present and future perspectives for SOFC Technologies," *Green Energy Technol.*, vol. 55, 2013, doi: 10.1007/978-1-4471-4456-4.

[23] V. S. Bagotsky, *Fuel Cells: Problems and Solutions*. 2008.

[24] J. M. Andújar and F. Segura, "Fuel cells: History and updating. A walk along two centuries," *Renewable and Sustainable Energy Reviews*, vol. 13, no. 9. 2009, doi: 10.1016/j.rser.2009.03.015.

[25] A. G. Olabi, T. Wilberforce, and M. A. Abdelkareem, "Fuel cell application in the automotive industry and future perspective," *Energy*, vol. 214, 2021, doi: 10.1016/j.energy.2020.118955.

[26] O. Z. Sharaf and M. F. Orhan, "An overview of fuel cell technology: Fundamentals and applications," *Renewable and Sustainable Energy Reviews*, vol. 32. 2014, doi: 10.1016/j.rser.2014.01.012.

[27] M. Winter and R. J. Brodd, "What are batteries, fuel cells, and supercapacitors?," *Chem. Rev.*, vol. 104, no. 10, 2004, doi: 10.1021/cr020730k.

[28] M. Winter and R. J. Brodd, " What Are Batteries, Fuel Cells, and Supercapacitors? (Chem. Rev. 2003 , 104 , 4245−4269. Published on the Web 09/28/2004.) ," *Chem. Rev.*, vol. 105, no. 3, 2005, doi: 10.1021/cr040110e.

[29] U. A. Icardi, S. Specchia, G. J. R. Fontana, G. Saracco, and V. Specchia, "Compact direct methanol fuel cells for portable application," *J. Power Sources*, vol. 176, no. 2, 2008, doi: 10.1016/j.jpowsour.2007.08.048.

[30] T. Wilberforce, A. Alaswad, A. Palumbo, M. Dassisti, and A. G. Olabi, "Advances in stationary and portable fuel cell applications," *Int. J. Hydrogen Energy*, vol. 41, no. 37, 2016, doi: 10.1016/j.ijhydene.2016.02.057.

[31] J. H. Wee, "Applications of proton exchange membrane fuel cell systems," *Renewable and Sustainable Energy Reviews*, vol. 11, no. 8. 2007, doi: 10.1016/j.rser.2006.01.005.

[32] A. Q. Al-Amin and B. Doberstein, "Introduction of hydrogen fuel cell vehicles: prospects and challenges for Malaysia's transition to a low-carbon economy," *Environ. Sci. Pollut. Res.*, vol. 26, no. 30, 2019, doi: 10.1007/s11356-019-06128-4.

[33] A. F. Ambrose, A. Q. Al-Amin, R. Rasiah, R. Saidur, and N. Amin, "Prospects for introducing hydrogen fuel cell vehicles in Malaysia," *Int. J. Hydrogen Energy*, vol. 42, no. 14, 2017, doi: 10.1016/j.ijhydene.2016.05.122.

[34] N. P. Brandon and Z. Kurban, "Clean energy and the hydrogen economy," *Philos. Trans. R. Soc. A Math. Phys. Eng. Sci.*, vol. 375, no. 2098, 2017, doi: 10.1098/rsta.2016.0400.

[35] M. Contestabile, G. J. Offer, R. Slade, F. Jaeger, and M. Thoennes, "Battery electric vehicles, hydrogen fuel cells and biofuels. Which will be the winner?," *Energy Environ. Sci.*, vol. 4, no. 10, 2011, doi: 10.1039/c1ee01804c.

[36] A. Kirubakaran, S. Jain, and R. K. Nema, "A review on fuel cell technologies and power electronic interface," *Renewable and Sustainable Energy Reviews*, vol. 13, no. 9. 2009, doi: 10.1016/j.rser.2009.04.004.

[37] L. Carrette, K. A. Friedrich, and U. Stimming, "Fuel Cells: Principles, Types, Fuels, and Applications," *ChemPhysChem*, vol. 1, no. 4, 2000, doi: 10.1002/1439-7641(20001215)1:4<162::aid-cphc162>3.0.co;2-z.

[38] L. Carrette, K. A. Friedrich, and U. Stimming, "Fuel cells: Principles, types, fuels, and applications," *ChemPhysChem*, vol. 1, no. 4. 2000, doi: 10.1002/1439-7641(20001215)1:4<162::aid-cphc162>3.3.co;2-q.

[39] P. Parkhey and R. Sahu, "Microfluidic microbial fuel cells: Recent advancements and future prospects," *Int. J. Hydrogen Energy*, vol. 46, no. 4, 2021, doi: 10.1016/j.ijhydene.2020.07.019.

[40] M. Andersson, J. Yuan, and B. Sundén, "Review on modeling development for multiscale chemical reactions coupled transport phenomena in solid oxide fuel cells," *Applied*

Energy, vol. 87, no. 5. 2010, doi: 10.1016/j.apenergy.2009.11.013.

[41] S. Jain, J. Jiang, X. Huang, and S. Stevandic, "Modeling of fuel-cell-based power supply system for grid interface," *IEEE Trans. Ind. Appl.*, vol. 48, no. 4, 2012, doi: 10.1109/TIA.2012.2199454.

[42] M. H. Nehrir and C. Wang, *Modeling and control of fuel cells: Distributed generation applications*. 2009.

[43] J. W. Patrick, "Handbook of fuel cells. Fundamentals technology and applications," *Fuel*, vol. 83, no. 4–5, 2004, doi: 10.1016/j.fuel.2003.09.012.

[44] R. S. Tiara Dewi, Muhammad Amir Masruhim, *Fuel Cell Fundamentals - Third Edition*, no. April. 2016.

[45] M. K. Singla, P. Nijhawan, and A. S. Oberoi, "Hydrogen fuel and fuel cell technology for cleaner future: a review," *Environ. Sci. Pollut. Res.*, vol. 28, no. 13, pp. 15607–15626, 2021, doi: 10.1007/s11356-020-12231-8.

[46] K. Scott, "Introduction to Hydrogen, Electrolyzers and Fuel Cells Science and Technology," in *Comprehensive Renewable Energy*, 2022.

[47] "Introduction to Fuel Cells: Electrochemistry and Materials," *Focus Catal.*, vol. 2020, no. 9, 2020, doi: 10.1016/j.focat.2020.08.052.

[48] M. S. Whittingham, R. F. Savinell, and T. Zawodzinski, "Introduction: Batteries and fuel cells," *Chemical Reviews*, vol. 104, no. 10. 2004, doi: 10.1021/cr020705e.

[49] M. M. Mench, C. Wang, and S. T. Thynell, "An Introduction to Fuel Cells and Related Transport Phenomena," *Int. J. Transp. Phenom.*, vol. 3, no. 3, 2001.

[50] Z. Zhan and S. A. Barnett, "An octane-fueled solid oxide fuel cell," *Science (80-.).*, vol. 308, no. 5723, 2005, doi: 10.1126/science.1109213.

[51] A. Nafees and R. Abdul Rasid, "Study of natural gas powered solid oxide fuel cell simulation and modeling," in *IOP Conference Series: Materials Science and Engineering*, 2019, vol. 702, no. 1, doi: 10.1088/1757-899X/702/1/012017.

[52] S. Kakaç, A. Pramuanjaroenkij, and X. Y. Zhou, "A review of numerical modeling of solid oxide fuel cells," *International Journal of Hydrogen Energy*, vol. 32, no. 7. 2007, doi: 10.1016/j.ijhydene.2006.11.028.

[53] A. K. Podder, O. Chakraborty, S. Islam, N. Manoj Kumar, and H. H. Alhelou, "Control Strategies of Different Hybrid Energy Storage Systems for Electric Vehicles Applications," *IEEE Access*, vol. 9, 2021, doi: 10.1109/ACCESS.2021.3069593.

[54] A. Afif, N. Radenahmad, Q. Cheok, S. Shams, J. H. Kim, and A. K. Azad, "Ammonia-fed fuel cells: A comprehensive review," *Renewable and Sustainable Energy Reviews*, vol.

60. 2016, doi: 10.1016/j.rser.2016.01.120.

[55] S. Mekhilef, R. Saidur, and A. Safari, "Comparative study of different fuel cell technologies," *Renewable and Sustainable Energy Reviews*, vol. 16, no. 1. 2012, doi: 10.1016/j.rser.2011.09.020.

[56] S. B. Beale *et al.*, "Continuum scale modelling and complementary experimentation of solid oxide cells," *Progress in Energy and Combustion Science*, vol. 85. 2021, doi: 10.1016/j.pecs.2020.100902.

[57] M. Bavarian, M. Soroush, I. G. Kevrekidis, and J. B. Benziger, "Mathematical modeling, steady-state and dynamic behavior, and control of fuel cells: A review," *Ind. Eng. Chem. Res.*, vol. 49, no. 17, 2010, doi: 10.1021/ie100032c.

[58] H. H. Faheem, S. Z. Abbas, A. N. Tabish, L. Fan, and F. Maqbool, "A review on mathematical modelling of Direct Internal Reforming- Solid Oxide Fuel Cells," *Journal of Power Sources*, vol. 520. 2022, doi: 10.1016/j.jpowsour.2021.230857.

[59] S. A. Hajimolana, M. A. Hussain, W. M. A. W. Daud, M. Soroush, and A. Shamiri, "Mathematical modeling of solid oxide fuel cells: A review," *Renewable and Sustainable Energy Reviews*, vol. 15, no. 4. 2011, doi: 10.1016/j.rser.2010.12.011.

[60] M. Peksen, "Numerical thermomechanical modelling of solid oxide fuel cells," *Progress in Energy and Combustion Science*, vol. 48. 2015, doi: 10.1016/j.pecs.2014.12.001.

[61] H. Xu, B. Chen, and M. Ni, "Modeling of Direct Carbon-Assisted Solid Oxide Electrolysis Cell (SOEC) for Syngas Production at Two Different Electrodes," *J. Electrochem. Soc.*, vol. 163, no. 11, 2016, doi: 10.1149/2.0041611jes.

[62] T. S. Zhao, C. Xu, R. Chen, and W. W. Yang, "Mass transport phenomena in direct methanol fuel cells," *Progress in Energy and Combustion Science*, vol. 35, no. 3. 2009, doi: 10.1016/j.pecs.2009.01.001.

[63] U. Ibrahim and A. Ayub, "Direct Carbon Fuel Cell-Cleaner and Efficient Future Power Generation Technology," *Adv. J. Grad. Res.*, vol. 6, no. 1, 2019, doi: 10.21467/ajgr.6.1.14-30.

[64] L. An and T. S. Zhao, "Transport phenomena in alkaline direct ethanol fuel cells for sustainable energy production," *Journal of Power Sources*, vol. 341. 2017, doi: 10.1016/j.jpowsour.2016.11.117.

[65] M. Mayur, M. Gerard, P. Schott, and W. G. Bessler, "Lifetime prediction of a polymer electrolyte membrane fuel cell under automotive load cycling using a physically-based catalyst degradation model," *Energies*, vol. 11, no. 8, 2018, doi: 10.3390/en11082054.

[66] K. Zheng, Y. Zhang, L. Li, and M. Ni, "On the tortuosity factor of solid phase in solid oxide fuel cell electrodes," *Int. J. Hydrogen Energy*, vol. 40, no. 1, pp. 665–669, Jan. 2015, doi: 10.1016/j.ijhydene.2014.10.111.

[67] S. Presto, P. Kumar, S. Varma, M. Viviani, and P. Singh, “Electrical conductivity of NiMo–based double perovskites under SOFC anodic conditions,” *Int. J. Hydrogen Energy*, vol. 43, no. 9, pp. 4528–4533, Mar. 2018, doi: 10.1016/j.ijhydene.2018.01.066.

[68] S. Futamura *et al.*, “SOFC anodes impregnated with noble metal catalyst nanoparticles for high fuel utilization,” *Int. J. Hydrogen Energy*, vol. 44, no. 16, pp. 8502–8518, Mar. 2019, doi: 10.1016/j.ijhydene.2019.01.223.

[69] A. Hagen, H. Langnickel, and X. Sun, “Operation of solid oxide fuel cells with alternative hydrogen carriers,” *Int. J. Hydrogen Energy*, vol. 44, no. 33, pp. 18382–18392, Jul. 2019, doi: 10.1016/j.ijhydene.2019.05.065.

[70] W. J. Sembler and S. Kumar, “Optimization of a single-cell solid-oxide fuel cell using computational fluid dynamics,” *ASME 2010 8th Int. Conf. Fuel Cell Sci. Eng. Technol. FUELCELL 2010*, vol. 2, pp. 1–14, 2010, doi: 10.1115/FuelCell2010-33013.

[71] Z. Qu *et al.*, “Three-dimensional computational fluid dynamics modeling of anode-supported planar SOFC,” in *International Journal of Hydrogen Energy*, 2011, vol. 36, no. 16, pp. 10209–10220, doi: 10.1016/j.ijhydene.2010.11.018.

[72] C. Zhao *et al.*, “Numerical simulation of flow distribution for external manifold design in solid oxide fuel cell stack,” *Int. J. Hydrogen Energy*, vol. 42, no. 10, pp. 7003–7013, Mar. 2017, doi: 10.1016/j.ijhydene.2016.12.009.

[73] W. J. Sembler, “Proceedings of the ASME 2010 Eighth International Fuel Cell Science, Engineering and Technology Conference FuelCell2010 June 14-16, 2010, Brooklyn, New York, USA,” pp. 1–14, 2016.

[74] S. C. Singhal, “Solid oxide fuel cells: Past, present and future,” *Green Energy Technol.*, vol. 55, 2013, doi: 10.1007/978-1-4471-4456-4_1.

[75] N. Shaigan, W. Qu, D. G. Ivey, and W. Chen, “A review of recent progress in coatings, surface modifications and alloy developments for solid oxide fuel cell ferritic stainless steel interconnects,” *Journal of Power Sources*, vol. 195, no. 6. 2010, doi: 10.1016/j.jpowsour.2009.09.069.

[76] P. S. Devi, A. Das Sharma, and H. S. Maiti, “Solid oxide fuel cell materials: A review,” *Trans. Indian Ceram. Soc.*, vol. 63, no. 2, 2004, doi: 10.1080/0371750X.2004.11012140.

[77] B. Huang, Y. Qi, and M. Murshed, “Solid oxide fuel cell: Perspective of dynamic modeling and control,” in *Journal of Process Control*, 2011, vol. 21, no. 10, doi: 10.1016/j.jprocont.2011.06.017.

[78] B. Huang, Y. Qi, and M. Murshed, “Solid Oxide Fuel Cell: Perspective of Dynamic Modeling and Control,” *IFAC Proc. Vol.*, vol. 43, no. 5, 2010, doi: 10.3182/20100705-3-be-2011.00023.

[79] L. Zhang, X. Li, J. Jiang, S. Li, J. Yang, and J. Li, “Dynamic modeling and analysis of a

5-kW solid oxide fuel cell system from the perspectives of cooperative control of thermal safety and high efficiency," *International Journal of Hydrogen Energy*, vol. 40, no. 1. 2015, doi: 10.1016/j.ijhydene.2014.10.149.

[80] B. Huang, Y. Qi, and M. Murshed, "Solid oxide fuel cell: Perspective of dynamic modeling and control," in *IFAC Proceedings Volumes (IFAC-PapersOnline)*, 2010, vol. 9, no. PART 1, doi: 10.3182/20100705-3-BE-2011.0208.

[81] H. Cao *et al.*, "Dynamic modeling and experimental validation for the electrical coupling in a 5-cell solid oxide fuel cell stack in the perspective of thermal coupling," *Int. J. Hydrogen Energy*, vol. 36, no. 7, 2011, doi: 10.1016/j.ijhydene.2011.01.032.

[82] S. C. Singhal, "Solid oxide fuel cells for power generation," *Wiley Interdiscip. Rev. Energy Environ.*, vol. 3, no. 2, pp. 179–194, 2014, doi: 10.1002/wene.96.

[83] A. S. Nesaraj, "Recent developments in solid oxide fuel cell technology - A review," *Journal of Scientific and Industrial Research*, vol. 69, no. 3. 2010.

[84] F. S. da Silva and T. M. de Souza, "Novel materials for solid oxide fuel cell technologies: A literature review," *International Journal of Hydrogen Energy*, vol. 42, no. 41. 2017, doi: 10.1016/j.ijhydene.2017.08.105.

[85] A. Choudhury, H. Chandra, and A. Arora, "Application of solid oxide fuel cell technology for power generation - A review," *Renewable and Sustainable Energy Reviews*, vol. 20. 2013, doi: 10.1016/j.rser.2012.11.031.

[86] N. Mahato, A. Banerjee, A. Gupta, S. Omar, and K. Balani, "Progress in material selection for solid oxide fuel cell technology: A review," *Progress in Materials Science*, vol. 72. 2015, doi: 10.1016/j.pmatsci.2015.01.001.

[87] A. Jun, J. Kim, J. Shin, and G. Kim, "Perovskite as a Cathode Material: A Review of its Role in Solid-Oxide Fuel Cell Technology," *ChemElectroChem*, vol. 3, no. 4, 2016, doi: 10.1002/celc.201500382.

[88] N. Laosiripojana, W. Wiyaratn, W. Kiatkittipong, A. Arpornwichanop, A. Soottitantawat, and S. Assabumrungrat, "Reviews on solid oxide fuel cell technology," *Eng. J.*, vol. 13, no. 1, 2009, doi: 10.4186/ej.2009.13.1.65.

[89] J. O. Bockris, "Handbook of fuel cell technology," *Electrochim. Acta*, vol. 14, no. 9, 1969, doi: 10.1016/0013-4686(69)87014-3.

[90] R. . Hirschenhofer , J.H; Stauffer , D.B ; Engleman, "Fuel Cell handbook," *Tecnol. Overview/ Appl. Demonstr. Status/ Veh. Motiv. Power*, 1998.

[91] G. Hoogers, *Fuel cell technology handbook*. 2002.

[92] *Fuel Cell Technologies: State and Perspectives*. 2005.

[93] I. Kosacki, “Nanoscaled Oxide Thin Films for Energy Conversion,” in *Fuel Cell Technologies: State and Perspectives*, 2006.

[94] J. G. Carton, A. Baroutaji, and M. Ramadan, “Developments of Foam Materials for Fuel Cell Technology,” in *Encyclopedia of Smart Materials*, 2021.

[95] M. Mori, R. Stropnik, M. Sekavčnik, and A. Lotrič, “Criticality and life-cycle assessment of materials used in fuel-cell and hydrogen technologies,” *Sustain.*, vol. 13, no. 6, 2021, doi: 10.3390/su13063565.

[96] A. Dhand, “Advances in Materials for Fuel Cell Technologies- A Review,” *Int. J. Res. Appl. Sci. Eng. Technol.*, vol. V, no. IX, 2017, doi: 10.22214/ijraset.2017.9243.

[97] H. Sumi, H. Shimada, Y. Yamaguchi, Y. Mizutani, Y. Okuyama, and K. Amezawa, “Comparison of electrochemical impedance spectra for electrolyte-supported solid oxide fuel cells (SOFCs) and protonic ceramic fuel cells (PCFCs),” *Sci. Rep.*, vol. 11, no. 1, 2021, doi: 10.1038/s41598-021-90211-9.

[98] J. T. S. Irvine *et al.*, “Scandia-Zirconia Electrolytes and Electrodes for SOFCS,” in *Fuel Cell Technologies: State and Perspectives*, 2006.

[99] T. A. Adams, J. Nease, D. Tucker, and P. I. Barton, “Energy conversion with solid oxide fuel cell systems: A review of concepts and outlooks for the short- and long-term,” *Industrial and Engineering Chemistry Research*, vol. 52, no. 9. 2013, doi: 10.1021/ie300996r.

[100] K. Chen and S. P. Jiang, “Review—Materials Degradation of Solid Oxide Electrolysis Cells,” *J. Electrochem. Soc.*, vol. 163, no. 11, 2016, doi: 10.1149/2.0101611jes.

[101] J. T. S. Irvine and P. Connor, “Alternative materials for SOFCs, opportunities and limitations,” *Green Energy Technol.*, vol. 55, 2013, doi: 10.1007/978-1-4471-4456-4_7.

[102] E. Perry Murray, T. Tsai, and S. A. Barnett, “A direct-methane fuel cell with a ceria-based anode,” *Nature*, vol. 400, no. 6745, 1999, doi: 10.1038/23220.

[103] Y. M. Choi, C. Compson, M. C. Lin, and M. Liu, “Ab initio analysis of sulfur tolerance of Ni, Cu, and Ni-Cu alloys for solid oxide fuel cells,” *J. Alloys Compd.*, vol. 427, no. 1–2, 2007, doi: 10.1016/j.jallcom.2006.03.009.

[104] E. Fabbri, D. Pergolesi, and E. Traversa, “Electrode materials: A challenge for the exploitation of protonic solid oxide fuel cells,” *Science and Technology of Advanced Materials*, vol. 11, no. 4. 2010, doi: 10.1088/1468-6996/11/4/044301.

[105] J. W. Fergus, “Materials challenges for solid-oxide fuel cells,” *JOM*, vol. 59, no. 12. 2007, doi: 10.1007/s11837-007-0153-x.

[106] S. Hui and A. Petric, “Evaluation of yttrium-doped SrTiO3 as an anode for solid oxide fuel cells,” *J. Eur. Ceram. Soc.*, vol. 22, no. 9–10, 2002, doi: 10.1016/S0955-

2219(01)00485-X.

[107] S. Hui and A. Petric, “Electrical Properties of Yttrium-Doped Strontium Titanate under Reducing Conditions,” *J. Electrochem. Soc.*, vol. 149, no. 1, 2002, doi: 10.1149/1.1420706.

[108] P. Blennow, K. K. Hansen, L. R. Wallenberg, and M. Mogensen, “Electrochemical characterization and redox behavior of Nb-doped SrTiO3,” *Solid State Ionics*, vol. 180, no. 1, 2009, doi: 10.1016/j.ssi.2008.10.011.

[109] J. Savioli and G. W. Watson, “Computational modelling of solid oxide fuel cells,” *Current Opinion in Electrochemistry*, vol. 21. 2020, doi: 10.1016/j.coelec.2019.12.007.

[110] S. P. Ping, J. P. Zhang, and K. Föger, “Chemical interactions between 3 mol% yttria-zirconia and Sr-doped lanthanum manganite,” *J. Eur. Ceram. Soc.*, vol. 23, no. 11, 2003, doi: 10.1016/S0955-2219(02)00447-8.

[111] M. Rękas, “Electrolytes for intermediate temperature solid oxide fuel cells,” *Arch. Metall. Mater.*, vol. 60, no. 2A, 2015, doi: 10.1515/amm-2015-0225.

[112] J. A. Kilner and M. Burriel, “Materials for intermediate-temperature solid-oxide fuel cells,” *Annu. Rev. Mater. Res.*, vol. 44, 2014, doi: 10.1146/annurev-matsci-070813-113426.

[113] B. Conti, B. Bosio, S. J. McPhail, F. Santoni, D. Pumiglia, and E. Arato, “A 2-D model for intermediate temperature solid oxide fuel cells preliminarily validated on local values,” *Catalysts*, vol. 9, no. 1, 2019, doi: 10.3390/catal9010036.

[114] J. L. Hall, “Cell components,” *Phytochemistry*, vol. 26, no. 4, 1987, doi: 10.1016/s0031-9422(00)82398-5.

[115] D. B. Stauffer, J. H. Hirschenhofer, M. G. Klett, and R. R. Engleman, “Fuel Cell Handbook, Fourth Edition,” 1998.

[116] S. S. Penner *et al.*, “Commercialization of fuel cells,” *Energy*, vol. 20, no. 5, pp. 331–470, May 1995, doi: 10.1016/0360-5442(95)00003-Y.

[117] V. Liso, A. C. Olesen, M. P. Nielsen, and S. K. Kær, “Performance comparison between partial oxidation and methane steam reforming processes for solid oxide fuel cell (SOFC) micro combined heat and power (CHP) system,” *Energy*, vol. 36, no. 7, pp. 4216–4226, Jul. 2011, doi: 10.1016/j.energy.2011.04.022.

[118] J. Larminie and A. Dicks, *Fuel cell systems explained: Second edition*. 2013.

[119] P. Costamagna, A. Selimovic, M. Del Borghi, and G. Agnew, “Electrochemical model of the integrated planar solid oxide fuel cell (IP-SOFC),” *Chem. Eng. J.*, vol. 102, no. 1, 2004, doi: 10.1016/j.cej.2004.02.005.

[120] P. Costamagna, S. Grosso, R. Travis, and L. Magistri, “Integrated planar solid oxide fuel cell: Steady-state model of a bundle and validation through single tube experimental data,” *Energies*, vol. 8, no. 11, 2015, doi: 10.3390/en81112364.

[121] B. Wang, J. Zhu, and Z. Lin, “A theoretical framework for multiphysics modeling of methane fueled solid oxide fuel cell and analysis of low steam methane reforming kinetics,” *Appl. Energy*, vol. 176, 2016, doi: 10.1016/j.apenergy.2016.05.049.

[122] M. Irshad *et al.*, “A brief description of high temperature solid oxide fuel cell’s operation, materials, design, fabrication technologies and performance,” *Applied Sciences (Switzerland)*, vol. 6, no. 3. 2016, doi: 10.3390/app6030075.

[123] K. Huang and S. C. Singhal, “Cathode-supported tubular solid oxide fuel cell technology: A critical review,” *Journal of Power Sources*, vol. 237. 2013, doi: 10.1016/j.jpowsour.2013.03.001.

[124] C. O. Colpan, I. Dincer, and F. Hamdullahpur, “Thermodynamic modeling of direct internal reforming solid oxide fuel cells operating with syngas,” *Int. J. Hydrogen Energy*, vol. 32, no. 7, 2007, doi: 10.1016/j.ijhydene.2006.10.059.

[125] F. J. Gardner, M. J. Day, N. P. Brandon, M. N. Pashley, and M. Cassidy, “SOFC technology development at Rolls-Royce,” *J. Power Sources*, vol. 86, no. 1, 2000, doi: 10.1016/S0378-7753(99)00428-0.

[126] E. Audasso, F. R. Bianchi, and B. Bosio, “2D simulation for CH4internal reforming-SOFCs: An approach to study performance degradation and optimization,” *Energies*, vol. 13, no. 15, 2020, doi: 10.3390/en13164116.

[127] N. L. Garland, D. C. Papageorgopoulos, and J. M. Stanford, “Hydrogen and fuel cell technology: Progress, challenges, and future directions,” in *Energy Procedia*, 2012, vol. 28, doi: 10.1016/j.egypro.2012.08.034.

[128] M. Cimenti and J. M. Hill, “Direct utilization of liquid fuels in SOFC for portable applications: Challenges for the selection of alternative anodes,” *Energies*, vol. 2, no. 2. 2009, doi: 10.3390/en20200377.

[129] D. Sánchez, R. Chacartegui, A. Muñoz, and T. Sánchez, “Thermal and electrochemical model of internal reforming solid oxide fuel cells with tubular geometry,” *J. Power Sources*, vol. 160, no. 2 SPEC. ISS., 2006, doi: 10.1016/j.jpowsour.2006.02.098.

[130] J. B. Goodenough and Y. H. Huang, “Alternative anode materials for solid oxide fuel cells,” *Journal of Power Sources*, vol. 173, no. 1. 2007, doi: 10.1016/j.jpowsour.2007.08.011.

[131] Y. KOMATSU, G. BRUS, J. S. SZMYD, and S. KIMIJIMA, “C113 Experimental Study on Dynamic Behavior of 300W Class Planar Type Solid Oxide Fuel Cell Stacks,” *Proc. Natl. Symp. Power Energy Syst.*, vol. 2012.17, no. 0, 2012, doi: 10.1299/jsmepes.2012.17.95.

[132] J. Wang, D. Yan, J. Pu, B. Chi, and L. Jian, “Fabrication and performance evaluation of planar solid oxide fuel cell with large active reaction area,” *Int. J. Hydrogen Energy*, vol. 36, no. 12, 2011, doi: 10.1016/j.ijhydene.2011.03.011.

[133] A. Lanzini, P. Leone, M. Santarelli, P. Asinari, and M. Cali, “Performance and degradation effects of anode-supported cells with LSM and LSCF cathodes,” in *ASME International Mechanical Engineering Congress and Exposition, Proceedings*, 2008, vol. 6, doi: 10.1115/IMECE2007-43421.

[134] A. Lanzini, P. Leone, M. Santarelli, P. Asinari, M. Calì, and R. Borchiellini, “Performances and degradation phenomena of solid oxide anode supported cells with LSM and LSCF cathodes: An experimental assessment,” *J. Fuel Cell Sci. Technol.*, vol. 6, no. 1, 2009, doi: 10.1115/1.2971128.

[135] S. Seidler, M. Henke, J. Kallo, W. G. Bessler, U. Maier, and K. A. Friedrich, “Pressurized solid oxide fuel cells: Experimental studies and modeling,” in *Journal of Power Sources*, 2011, vol. 196, no. 17, doi: 10.1016/j.jpowsour.2010.09.100.

[136] H. Y. Jung *et al.*, “Fabrication and performance evaluation of 3-cell SOFC stack based on planar 10 cm × 10 cm anode-supported cells,” *J. Power Sources*, vol. 159, no. 1 SPEC. ISS., 2006, doi: 10.1016/j.jpowsour.2005.10.103.

[137] J. Luo *et al.*, “Electrochemical performance and thermal cyclicability of industrial-sized anode supported planar solid oxide fuel cells,” *J. Power Sources*, vol. 224, 2013, doi: 10.1016/j.jpowsour.2012.09.087.

[138] S. Bedogni, S. Campanari, P. Iora, L. Montelatici, and P. Silva, “Experimental analysis and modeling for a circular-planar type IT-SOFC,” *J. Power Sources*, vol. 171, no. 2, 2007, doi: 10.1016/j.jpowsour.2007.07.014.

[139] V. Lawlor *et al.*, “Experimental and numerical study of various MT-SOFC flow manifold techniques: Single MT-SOFC analysis,” *J. Fuel Cell Sci. Technol.*, vol. 10, no. 1, 2013, doi: 10.1115/1.4023216.

[140] H. Yakabe, Y. Baba, T. Sakurai, and Y. Yoshitaka, “Evaluation of the residual stress for anode-supported SOFCs,” *J. Power Sources*, vol. 135, no. 1–2, 2004, doi: 10.1016/j.jpowsour.2003.11.049.

[141] W. Fischer, J. Malzbender, G. Blass, and R. W. Steinbrech, “Residual stresses in planar solid oxide fuel cells,” *J. Power Sources*, vol. 150, no. 1–2, 2005, doi: 10.1016/j.jpowsour.2005.02.014.

[142] M. Yano, A. Tomita, M. Sano, and T. Hibino, “Recent advances in single-chamber solid oxide fuel cells: A review,” *Solid State Ionics*, vol. 177, no. 39–40. 2007, doi: 10.1016/j.ssi.2006.10.014.

[143] Y. Luo, W. Jiang, Q. Zhang, W. Y. Zhang, and M. Hao, “Effects of anode porosity on thermal stress and failure probability of planar solid oxide fuel cell with bonded compliant

seal," *Int. J. Hydrogen Energy*, vol. 41, no. 18, 2016, doi: 10.1016/j.ijhydene.2016.03.117.

[144] O. Razbani, I. Wærnhus, and M. Assadi, "Experimental investigation of temperature distribution over a planar solid oxide fuel cell," *Appl. Energy*, vol. 105, 2013, doi: 10.1016/j.apenergy.2012.12.062.

[145] B. Morel, Ŕ. Roberge, S. Savoie, T. W. Napporn, and M. Meunier, "An experimental evaluation of the temperature gradient in solid oxide fuel cells," *Electrochem. Solid-State Lett.*, vol. 10, no. 2, 2007, doi: 10.1149/1.2398729.

[146] Y. Kim, S. Y. Jo, and J.-Y. Park, "Developing Redox Stability of Ceramic Anode Supported Intermediate Temperature Solid Oxide Fuel Cells," *ECS Meet. Abstr.*, vol. MA2017-03, no. 1, 2017, doi: 10.1149/ma2017-03/1/156.

[147] S. Sayadian, M. Ghassemi, and A. J. Robinson, "Multi-physics simulation of transport phenomena in planar proton-conducting solid oxide fuel cell," *J. Power Sources*, vol. 481, p. 228997, Jan. 2021, doi: 10.1016/j.jpowsour.2020.228997.

[148] S. C. Singhal and K. Kendall, "High Temperature Solid Oxide Fuel Cells : Fundamentals , Design and Applications Edited by : Subhash C Singhal and Kevin Kendall," pp. 197–225, 2003.

[149] M. Liu *et al.*, "Enhanced sulfur and coking tolerance of a mixed ion conductor for SOFCs: BaZr0.1Ce0.7y0.2-XYb xO3-δ," *Science (80-.).*, vol. 326, no. 5949, pp. 126–129, 2009, doi: 10.1126/science.1174811.

[150] B. C. H. Steele, "Appraisal of Ce1-yGdyO2-y/2 electrolytes for IT-SOFC operation at 500 °C," *Solid State Ionics*, vol. 129, no. 1, 2000, doi: 10.1016/S0167-2738(99)00319-7.

[151] J. Rossmeisl and W. G. Bessler, "Trends in catalytic activity for SOFC anode materials," *Solid State Ionics*, vol. 178, no. 31–32, pp. 1694–1700, 2008, doi: 10.1016/j.ssi.2007.10.016.

[152] T. Takeguchi, R. Kikuchi, T. Yano, K. Eguchi, and K. Murata, "Effect of precious metal addition to Ni-YSZ cermet on reforming of CH 4 and electrochemical activity as SOFC anode," in *Catalysis Today*, 2003, vol. 84, no. 3–4, pp. 217–222, doi: 10.1016/S0920-5861(03)00278-5.

[153] Y. L. Lee, J. Kleis, J. Rossmeisl, S. H. Yang, and D. Morgan, "Prediction of solid oxide fuel cell cathode activity with first-principles descriptors," *Energy Environ. Sci.*, vol. 4, no. 10, pp. 3966–3970, 2011, doi: 10.1039/c1ee02032c.

[154] M. Andersson, J. Yuan, and B. Sundén, "SOFC modeling considering hydrogen and carbon monoxide as electrochemical reactants," *J. Power Sources*, vol. 232, pp. 42–54, 2013, doi: 10.1016/j.jpowsour.2012.12.122.

[155] Y. Jiang and A. V. Virkar, "Fuel Composition and Diluent Effect on Gas Transport and Performance of Anode-Supported SOFCs," *J. Electrochem. Soc.*, vol. 150, no. 7, 2003,

doi: 10.1149/1.1579480.

[156] S. N. Hosseini, F. Karimzadeh, M. H. Enayati, and N. M. Sammes, “Oxidation and electrical behavior of CuFe2O4 spinel coated Crofer 22 APU stainless steel for SOFC interconnect application,” *Solid State Ionics*, vol. 289, pp. 95–105, 2016, doi: 10.1016/j.ssi.2016.02.015.

[157] Z. Yang, G. G. Xia, X. H. Li, and J. W. Stevenson, “(Mn,Co)3O4 spinel coatings on ferritic stainless steels for SOFC interconnect applications,” *Int. J. Hydrogen Energy*, vol. 32, no. 16, 2007, doi: 10.1016/j.ijhydene.2006.08.048.

[158] S. Zeng, X. Zhang, J. Song Chen, T. Li, and M. Andersson, “Modeling of solid oxide fuel cells with optimized interconnect designs,” *Int. J. Heat Mass Transf.*, vol. 125, pp. 506–514, 2018, doi: 10.1016/j.ijheatmasstransfer.2018.04.096.

[159] C. Zhao *et al.*, “Numerical simulation of flow distribution for external manifold design in solid oxide fuel cell stack,” *Int. J. Hydrogen Energy*, vol. 42, no. 10, pp. 7003–7013, 2017, doi: 10.1016/j.ijhydene.2016.12.009.

[160] C. Zhao *et al.*, “Numerical modeling of manifold design and flow uniformity analysis of an external manifold solid oxide fuel cell stack,” *Int. J. Hydrogen Energy*, vol. 45, no. 28, pp. 14440–14451, 2020, doi: 10.1016/j.ijhydene.2020.02.143.

[161] H. Hesami, M. Borji, and J. Rezapour, “A comprehensive three-dimensional modeling of an internal reforming planar solid oxide fuel cell with different interconnect designs,” *J. Solid State Electrochem.*, vol. 1, p. 3, 2021, doi: 10.1007/s10008-021-05030-9.

[162] T. Dey, D. Singdeo, R. N. Basu, M. Bose, and P. C. Ghosh, “Improvement in solid oxide fuel cell performance through design modifications: An approach based on root cause analysis,” *Int. J. Hydrogen Energy*, vol. 39, no. 30, pp. 17258–17266, Oct. 2014, doi: 10.1016/j.ijhydene.2014.08.025.

[163] M. Xu *et al.*, “Modeling of an anode supported solid oxide fuel cell focusing on thermal stresses,” *Int. J. Hydrogen Energy*, vol. 41, no. 33, pp. 14927–14940, 2016, doi: 10.1016/j.ijhydene.2016.06.171.

[164] M. Saied, K. Ahmed, M. Ahmed, M. Nemat-Alla, and M. El-Sebaie, “Investigations of solid oxide fuel cells with functionally graded electrodes for high performance and safe thermal stress,” *Int. J. Hydrogen Energy*, vol. 42, no. 24, pp. 15887–15902, Jun. 2017, doi: 10.1016/j.ijhydene.2017.05.071.

[165] W. Kong, J. Li, S. Liu, and Z. Lin, “The influence of interconnect ribs on the performance of planar solid oxide fuel cell and formulae for optimal rib sizes,” *J. Power Sources*, vol. 204, pp. 106–115, 2012, doi: 10.1016/j.jpowsour.2012.01.041.

[166] M. Andersson, J. Yuan, and B. Sundén, “SOFC cell design optimization using the finite element method based CFD approach,” *Fuel Cells*, vol. 14, no. 2, pp. 177–188, 2014, doi: 10.1002/fuce.201300160.

[167] Q. Chen, Q. Wang, J. Zhang, and J. Yuan, “Effect of bi-layer interconnector design on mass transfer performance in porous anode of solid oxide fuel cells,” *Int. J. Heat Mass Transf.*, vol. 54, no. 9–10, pp. 1994–2003, Apr. 2011, doi: 10.1016/j.ijheatmasstransfer.2011.01.003.

[168] T. M. M. Heenan *et al.*, “The role of bi-polar plate design and the start-up protocol in the spatiotemporal dynamics during solid oxide fuel cell anode reduction,” *Energies*, vol. 13, no. 14, pp. 1–12, 2020, doi: 10.3390/en13143552.

[169] A. N. Celik, “Three-dimensional multiphysics model of a planar solid oxide fuel cell using computational fluid dynamics approach,” *Int. J. Hydrogen Energy*, vol. 43, no. 42, pp. 19730–19748, 2018, doi: 10.1016/j.ijhydene.2018.08.212.

[170] I. Khazaee and A. Rava, “Numerical simulation of the performance of solid oxide fuel cell with different flow channel geometries,” *Energy*, vol. 119, pp. 235–244, Jan. 2017, doi: 10.1016/j.energy.2016.12.074.

[171] R. M. Manglik and Y. N. Magar, “Heat and mass transfer in planar anode-supported solid oxide fuel cells: Effects of interconnect fuel/oxidant channel flow cross section,” *J. Therm. Sci. Eng. Appl.*, vol. 7, no. 4, pp. 1–10, 2015, doi: 10.1115/1.4030636.

[172] Z. Lin, J. W. Stevenson, and M. A. Khaleel, “The effect of interconnect rib size on the fuel cell concentration polarization in planar SOFCs,” *J. Power Sources*, vol. 117, no. 1–2, 2003, doi: 10.1016/S0378-7753(02)00726-7.

[173] Z. Lin, J. W. Stevenson, and M. A. Khaleel, “The effect of interconnect rib size on the fuel cell concentration polarization in planar SOFCs,” *J. Power Sources*, vol. 117, no. 1–2, pp. 92–97, May 2003, doi: 10.1016/S0378-7753(02)00726-7.

[174] S. Zeng, X. Zhang, J. Song Chen, T. Li, and M. Andersson, “Modeling of solid oxide fuel cells with optimized interconnect designs,” *Int. J. Heat Mass Transf.*, vol. 125, pp. 506–514, Oct. 2018, doi: 10.1016/j.ijheatmasstransfer.2018.04.096.

[175] D. Bhattacharya, J. Mukhopadhyay, N. Biswas, R. N. Basu, and P. K. Das, “Performance evaluation of different bipolar plate designs of 3D planar anode-supported SOFCs,” *Int. J. Heat Mass Transf.*, vol. 123, pp. 382–396, Aug. 2018, doi: 10.1016/j.ijheatmasstransfer.2018.02.096.

[176] W. Kong, Z. Han, S. Lu, X. Gao, and X. Wang, “A novel interconnector design of SOFC,” *Int. J. Hydrogen Energy*, vol. 45, no. 39, pp. 20329–20338, Aug. 2020, doi: 10.1016/j.ijhydene.2019.10.252.

[177] X. Gao, Q. Zhang, W. Zhang, and D. Chen, “Optimization of distributed cylindrical interconnect ribs for anode- and cathode-supported solid oxide fuel cell,” *Int. J. Electrochem. Sci.*, vol. 10, no. 9, pp. 7521–7534, 2015.

[178] Q. Fu, Z. Li, W. Wei, F. Liu, X. Xu, and Z. Liu, “Performance enhancement of planar solid oxide fuel cell using a novel interconnector design,” *Int. J. Hydrogen Energy*, vol.

46, no. 41, pp. 21634–21656, Jun. 2021, doi: 10.1016/j.ijhydene.2021.04.001.

[179] Y. J. Kim and M. C. Lee, "The influence of flow direction variation on the performance of a single cell for an anode-substrate flat-panel solid oxide fuel cell," *Int. J. Hydrogen Energy*, vol. 45, no. 39, pp. 20369–20381, Aug. 2020, doi: 10.1016/j.ijhydene.2019.10.129.

[180] K. P. Recknagle, R. E. Williford, L. A. Chick, D. R. Rector, and M. A. Khaleel, "Three-dimensional thermo-fluid electrochemical modeling of planar SOFC stacks," *J. Power Sources*, vol. 113, no. 1, pp. 109–114, 2003, doi: 10.1016/S0378-7753(02)00487-1.

[181] C. Schluckner, V. Subotić, S. Preißl, and C. Hochenauer, "Numerical analysis of flow configurations and electrical contact positions in SOFC single cells and their impact on local effects," *Int. J. Hydrogen Energy*, vol. 44, no. 3, pp. 1877–1895, 2019, doi: 10.1016/j.ijhydene.2018.11.132.

[182] Z. Zhang *et al.*, "Three-dimensional CFD modeling of transport phenomena in multi-channel anode-supported planar SOFCs," *Int. J. Heat Mass Transf.*, vol. 84, pp. 942–954, May 2015, doi: 10.1016/j.ijheatmasstransfer.2015.01.097.

[183] X. Li, W. Shi, and M. Han, "Optimization of interconnect flow channels width in a planar solid oxide fuel cell," *Int. J. Hydrogen Energy*, vol. 43, no. 46, pp. 21524–21534, Nov. 2018, doi: 10.1016/j.ijhydene.2018.09.061.

[184] B. Timurkutluk and E. Ucar, "Development of high performance and low-cost solid oxide fuel cell stacks: Numerical optimization of flow channel geometry," *Int. J. Energy Res.*, vol. 45, no. 15, pp. 20634–20650, 2021, doi: 10.1002/er.7129.

[185] Y. Mehdizadeh Chellehbari, K. Adavi, J. Sayyad Amin, and S. Zendehboudi, "A numerical simulation to effectively assess impacts of flow channels characteristics on solid oxide fuel cell performance," *Energy Convers. Manag.*, vol. 244, p. 114280, Sep. 2021, doi: 10.1016/J.ENCONMAN.2021.114280.

[186] A. A. Ebrahimzadeh, I. Khazaee, and A. Fasihfar, "Numerical investigation of obstacle's effect on the performance of proton-exchange membrane fuel cell: studying the shape of obstacles," *Heliyon*, vol. 5, no. 5, p. e01764, May 2019, doi: 10.1016/J.HELIYON.2019.E01764.

[187] Y. Mollayi Barzi, A. Raoufi, N. Manafi Rasi, and S. Davari, "Three Dimensional Simulation of a Counter-Flow Planar Solid Oxide Fuel Cell," *ECS Trans.*, vol. 35, no. 1, pp. 1021–1033, 2011, doi: 10.1149/1.3570083.

[188] Ansys Inc, "Fuel Cells Module Manual," *Fuel Cells*, no. April, 2009.

[189] W. J. Sembler and S. Kumar, "Modification of results from computational-fluid-dynamics simulations of single-cell solid-oxide fuel cells to estimate multicell stack performance," *J. Fuel Cell Sci. Technol.*, vol. 8, no. 2, pp. 1–10, 2011, doi: 10.1115/1.4002617.

[190] S. S. Wei, T. H. Wang, and J. S. Wu, "Numerical modeling of interconnect flow channel design and thermal stress analysis of a planar anode-supported solid oxide fuel cell stack," *Energy*, vol. 69, pp. 553–561, May 2014, doi: 10.1016/j.energy.2014.03.052.

[191] A. Pramuanjaroenkij, S. Kakaç, and X. Yang Zhou, "Mathematical analysis of planar solid oxide fuel cells," *Int. J. Hydrogen Energy*, vol. 33, no. 10, pp. 2547–2565, 2008, doi: 10.1016/j.ijhydene.2008.02.043.

[192] B. Ghorbani and K. Vijayaraghavan, "3D and simplified pseudo-2D modeling of single cell of a high temperature solid oxide fuel cell to be used for online control strategies," *Int. J. Hydrogen Energy*, vol. 43, no. 20, pp. 9733–9748, May 2018, doi: 10.1016/j.ijhydene.2018.03.211.

[193] J. M. Park, D. Y. Kim, J. D. Baek, Y. J. Yoon, P. C. Su, and S. H. Lee, "Effect of electrolyte thickness on electrochemical reactions and thermo-fluidic characteristics inside a SOFC unit cell," *Energies*, vol. 11, no. 3, 2018, doi: 10.3390/en11030473.

[194] D. H. Jeon, J. H. Nam, and C.-J. Kim, "Microstructural Optimization of Anode-Supported Solid Oxide Fuel Cells by a Comprehensive Microscale Model," *J. Electrochem. Soc.*, vol. 153, no. 2, p. A406, 2006, doi: 10.1149/1.2139954.

[195] S. Liu, C. Song, and Z. Lin, "The effects of the interconnect rib contact resistance on the performance of planar solid oxide fuel cell stack and the rib design optimization," *J. Power Sources*, vol. 183, no. 1, pp. 214–225, Aug. 2008, doi: 10.1016/j.jpowsour.2008.04.054.

[196] X. Zhang, L. Wang, M. Espinoza, T. Li, and M. Andersson, "Numerical simulation of solid oxide fuel cells comparing different electrochemical kinetics," *Int. J. Energy Res.*, vol. 45, no. 9, pp. 12980–12995, 2021, doi: 10.1002/er.6628.

[197] J. Ramasamy, K. Palaniswamy, T. Kumaresan, M. Chandran, and R. Chen, "Study of novel flow channels influence on the performance of direct methanol fuel cell," *Int. J. Hydrogen Energy*, vol. 47, no. 1, pp. 595–609, Jan. 2022, doi: 10.1016/j.ijhydene.2021.10.033.

[198] Y. Ji, K. Yuan, J. N. Chung, and Y. C. Chen, "Effects of transport scale on heat/mass transfer and performance optimization for solid oxide fuel cells," *J. Power Sources*, vol. 161, no. 1, pp. 380–391, 2006, doi: 10.1016/j.jpowsour.2006.04.097.

[199] Z. Dang, X. Shen, J. Ma, Z. Jiang, and G. Xi, "Multiphysics Coupling Simulation and Parameter Study of Planar Solid Oxide Fuel Cell," *Front. Chem.*, vol. 8, no. January, pp. 1–11, 2021, doi: 10.3389/fchem.2020.609338.

[200] G. Kaur, "Solid oxide fuel cell components: Interfacial compatibility of SOFC glass seals," *Solid Oxide Fuel Cell Components Interfacial Compat. SOFC Glas. Seals*, pp. 1–408, 2015, doi: 10.1007/978-3-319-25598-9.

[201] S. Mahabunphachai and M. Koç, "Fabrication of micro-channel arrays on thin metallic

sheet using internal fluid pressure: Investigations on size effects and development of design guidelines," *J. Power Sources*, vol. 175, no. 1, pp. 363–371, Jan. 2008, doi: 10.1016/J.JPOWSOUR.2007.09.036.

[202] Y. Song *et al.*, "Review on current research of materials, fabrication and application for bipolar plate in proton exchange membrane fuel cell," *Int. J. Hydrogen Energy*, vol. 45, no. 54, pp. 29832–29847, Nov. 2020, doi: 10.1016/J.IJHYDENE.2019.07.231.

[203] Z. Xu, L. Peng, P. Yi, and X. Lai, "Modeling of microchannel hydroforming process with thin metallic sheets," *J. Eng. Mater. Technol.*, vol. 134, no. 2, 2012, doi: 10.1115/1.4006180.

[204] J. C. Hung and C. C. Lin, "Fabrication of micro-flow channels for metallic bipolar plates by a high-pressure hydroforming apparatus," *J. Power Sources*, vol. 206, pp. 179–184, May 2012, doi: 10.1016/J.JPOWSOUR.2012.01.112.

[205] R. Kumar, A. Veeresh Babu, and S. H. Sonawane, "Performance evaluation of a trapezoidal interconnector configuration of solid oxide fuel cell: A numerical study," *Int. J. Energy Res.*, 2022, doi: 10.1002/er.8656.

Research Publications

List of Publications

1. Performance evaluation of a trapezoidal interconnector configuration of solid oxide fuel cell: A numerical study, **Raj Kumar, A. Veeresh Babu, Shirish H. Sonawane**, International Journal of Energy Research, 6(14):19710-19722 & 2022, doi:10.1002/er.8656, **SCI (Impact Factor : 4.67)**

2. Numerical investigation of a novel rhombohedral interconnector configuration for planar solid oxide fuel cells, **Raj Kumar, A. Veeresh Babu, Shirish H. Sonawane**, International Journal of Green Energy , doi:10.1080/15435075.2022.2154609, **SCI (Impact Factor : 3.2)**